2000

Multistage adaptive noise cancellation and multi-dimensional signal processing for ultrasonic nondestructive evaluation

Jae-Joon Kim
Iowa State University

Recommended Citation

Kim, Jae-Joon, "Multistage adaptive noise cancellation and multi-dimensional signal processing for ultrasonic nondestructive evaluation " (2000). *Retrospective Theses and Dissertations*. 12337.
https://lib.dr.iastate.edu/rtd/12337

INFORMATION TO USERS

This manuscript has been reproduced from the microfilm master. UMI films the text directly from the original or copy submitted. Thus, some thesis and dissertation copies are in typewriter face, while others may be from any type of computer printer.

The quality of this reproduction is dependent upon the quality of the copy submitted. Broken or indistinct print, colored or poor quality illustrations and photographs, print bleedthrough, substandard margins, and improper alignment can adversely affect reproduction.

In the unlikely event that the author did not send UMI a complete manuscript and there are missing pages, these will be noted. Also, if unauthorized copyright material had to be removed, a note will indicate the deletion.

Oversize materials (e.g., maps, drawings, charts) are reproduced by sectioning the original, beginning at the upper left-hand corner and continuing from left to right in equal sections with small overlaps.

Photographs included in the original manuscript have been reproduced xerographically in this copy. Higher quality 6" x 9" black and white photographic prints are available for any photographs or illustrations appearing in this copy for an additional charge. Contact UMI directly to order.

Bell & Howell Information and Learning
300 North Zeeb Road, Ann Arbor, MI 48106-1346 USA
800-521-0600

UMI®

Multistage adaptive noise cancellation and multi-dimensional signal processing for ultrasonic nondestructive evaluation

by

Jae-Joon Kim

A dissertation submitted to the graduate faculty
in partial fulfillment of the requirements for the degree of
DOCTOR OF PHILOSOPHY

Major: Electrical Engineering (Communications and Signal Processing)
Major Professor: Lalita Udpa

Iowa State University
Ames, Iowa
2000

UMI Number: 9990462

UMI®

Bell & Howell Information and Learning Company
300 North Zeeb Road
P.O. Box 1346
Ann Arbor, MI 48106-1346

Graduate College

Iowa State University

This is to certify that the Doctoral dissertation of

Jae-Joon Kim

has met the dissertation requirements of Iowa State University

Major Professor

For the Major Program

For the Graduate College

TABLE OF CONTENTS

LIST OF FIGURES

LIST OF TABLES

ABSTRACT

Ultrasonic signal processing presents several challenges with respect to both noise removal and interpretation. The interference of unwanted reflections from material grain structure can render the data extremely noisy and mask the detection of small flaws. It is therefore imperative to separate the flaw reflections from grain noise. The interpretation or classification of ultrasonic signals in general is relatively difficult due to the complexity of the physical process and similarity of signals from various classes of reflectors.

Adaptive noise cancellation techniques are ideally suited for reducing spatially varying noise due to the grain structure of material in ultrasonic nondestructive evaluation. In this research, a multi-stage adaptive noise cancellation (MANC) scheme is proposed for reducing spatially varying grain noise and enhancing flaw detection in ultrasonic signals. The overall scheme is based on the use of an adaptive least mean square error (LMSE) filter with primary and reference signals derived from two adjacent positions of the transducers. Since grain noise is generally uncorrelated, in contrast to the correlated flaw echoes, adaptive filtering algorithms exploit the correlation properties of signals in a C-scan image to enhance the signal-to-noise ratio (SNR) of the output signal.

A neural network-based signal classification system is proposed for the interpretation of ultrasonic signals obtained from inspection of welds, where signals have to be classified as resulting from porosity, slag, lack of fusion, or cracks in the weld region. Standard techniques rely on differences in individual A-scans to classify the signals. This thesis investigates the need for investigating signal features that incorporate the effects of beam spread and echo dynamics. Such effects call for data interpretation schemes that include a neighborhood of A-scans carrying information about a reflector. Several ultrasonic signal features based on the information in a two-dimensional array of ultrasonic waveforms, ranging from the estimation of statistical characteristics of signals to two and three-dimensional transform-based methods, are evaluated. A two-dimensional scan of ultrasonic testing is also represented in the form of images (B- and B'-scans). Multidimensional signal and image-processing algorithms are used to analyze the images. Two and three-dimensional Fourier transforms are applied to ultrasonic data that are inherently three-dimensional in nature (2 spatial and 1 time). A variety of transform-based features are then utilized for obtaining the final classification.

CHAPTER 1. INTRODUCTION

1.1 Weld Inspection and Ultrasonic Nondestructive Evaluation (NDE)

Welding is the most efficient way to join metals. It is also the only way to join two or more pieces of metal to make them act as one piece. Welding is widely used to manufacture or repair all products made of metal. Welds are encountered in many structures such as gas transmission pipelines, nuclear power reactors, aircrafts, automobiles, and ships.

In order to understand the concept of welding, we must first define joint and weld. A joint is the junction of members or the edges of members that are to be joined or have been joined. Welds in metals are produced either by heating materials to the welding temperature, with or without the application of pressure, or by applying pressure alone, again with or without the use of filler metal. Several types of weld joints exist, such as butt, corner, edge, lap, and tee joints.

Some of the commonly used methods in the arc welding process are shielded metal arc welding (SMAW) and gas metal arc welding (GMAW) [1][2]. SMAW is a process that contains an arc between a covered electrode and the weld pool. GMAW is an arc welding process that uses an arc between a continuous filler metal electrode and the weld pool. The process is used with shielding from an externally supplied gas and without the application of pressure (Figure 1.1). GMAW is used in all industrial manufacturing operations, military equipment, and field constructions including gas pipelines.

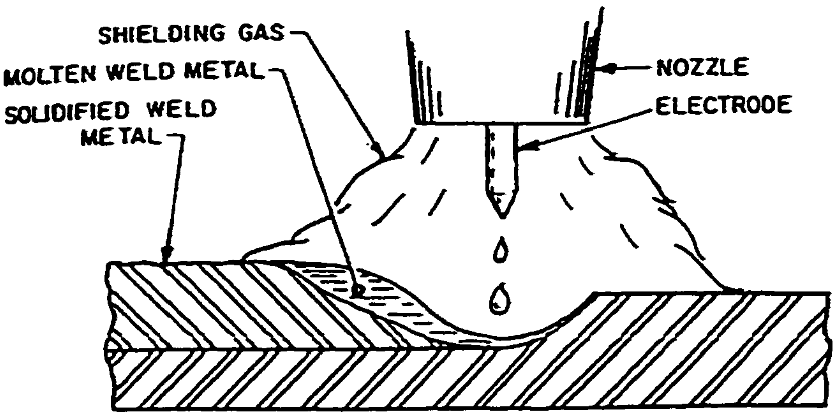

Figure 1.1 The gas metal arc welding process [1].

Weld defects are produced by material stress, fatigue, and environmental changes as well as the manufacturing process. During weld inspection, the commonly occurring defects in welded joints are porosity, slag, lack of fusion, and cracks. These defects can be categorized into two major types of discontinuities, namely volumetric and planar. Volumetric discontinuities include porosity and slag. Lack of fusion and cracks in the joints are referred to as planar flaws. Porosity is one of the most common weld defects. The main cause of weld metal porosity is the contamination of hydrogen in the weld metal. Porosity can be classified by size and location. It may be scattered in small clusters or occur along the entire length of the weld [3]. Fine scattered porosities are less severe than larger porosities, which are clustered or aligned. Aligned porosity is normally related to lack of fusion [4]. This defect is easily detected by radiographic inspection of the welds. Slags produced in arc welding serve as scavengers of impurities in the molten metal pool. This process forms a slag blanket over the weld that controls the cooling rates and excludes atmospheric oxygen from the hot metal surface.

Slag inclusions are often characterized by their location at the edges of the underlying metal deposits, where they often tend to extend longitudinally along the weld. They are generally detected by radiographic testing and have irregular shapes and sizes. Since slag inclusions cause a weakening of the weld and often serve as crack initiation points, this type of defect could probe difficulty for the operator to decipher the characteristics that exist between crack and slag inclusions. Porosity and slag inclusions are volumetric anomalies that mainly occur in the manufacturing welding process. They are considered to be less severe in terms of strength, but they can essentially deform material characteristics and initiate critical cracks.

Lack of fusion is a very common planar type of weld defect. It represents an area that suffers from insufficient mechanical binding between weld metal and base metal. Since the two surfaces of weld and base metal are pressed closely together, this type of defect is normally not detectable by radiographic examination. Although lack of fusion is in general not an acceptable weld defect, it is characterized as a planar defect and treated in the same way as cracks. Cracks are the most severe of the defects in a weld. Cracks may be embedded on the surface of the weld metal or in the heat affected zones. Most cracks occur during solidification and cooling, while some cracks may also develop at a later stage caused by stress or environmental conditions such as stress corrosion and fatigue. Cracks are difficult to detect by radiographic inspection alone unless their planes are aligned with the radiation direction.

To ensure cost saving and safety, weld defects are inspected by nondestructive methods that use one of inspection processes – visual, radiographic, or ultrasonic inspection. Radiography is most sensitive to volumetric type discontinuities because of the principle on which it works, i.e., absorption of radiation. The use of radiographic inspection technique is most prevalent in the shipping industry. The predominant types of discontinuities detectable in radiographic inspection are volumetric (slag and porosity).

Ultrasonic flaw detection has long been the preferred method for welding inspection in the nuclear industry. The safety, accuracy, and simplicity of the technique have continued to push the use of ultrasonics in piping welds inspection. In addition, ultrasonic testing has been reported to be more reliable in detecting planar weld discontinuities such as cracks and lack of fusion [5][6]. Ultrasonic inspection [7] can be carried out using straight beam and angle beam incident waves. Straight beam testing is often insensitive to cracks. For example, if the defect is vertical and thin, it will not reflect enough sound back to the transducer to ensure its detection. The other method of ultrasound testing is via angle beam incidence. Angle beam transducers use the principles of refraction and mode conversion to produce refracted shear or longitudinal waves in the test material. The process involves scanning the surface of the material around the weldment with the transducer. This refracted sound wave bounces off a reflector (discontinuity) in the path of the sound beam. With proper angle beam techniques, echoes returned from the weld zone allow the operator to determine the location and type of discontinuity.

Practical applications of radiographic inspection have several problems such as:

1. Radiation hazards that cause unnecessary delays until radiographic inspections are complete.
2. Inspection results are not immediately available, as the radiographic film must be processed and interpreted before the inspection is complete.

Ultrasonic inspection, on the other hand, presents no safety hazards. Concurrent work in adjacent areas can continue during the inspection procedure. Moreover, the inspection results are available immediately because the ultrasonic operator inspects, interprets, and disposes the weld at the time of the inspection. An additional advantage is the potential for more accurate sizing of discontinuities through the use of sophisticated software such as synthetic aperture focusing techniques (SAFT) [8][9]. In recent years, automated signal analysis systems have found increasing applications in ultrasonic weld inspection largely because these systems can potentially improve the ability to acquire and analyze data in a consistent manner.

This thesis attempts to develop an automated signal classification (ASC) system for consistent and accurate interpretation of weld ultrasonic data obtained from weld inspection. ASC system is also referred to as knowledge-based system since the system can embed expert knowledge in the analysis algorithms. Instead of relying only on ultrasonic amplitude, discontinuity length, and proximity measurements to interpret the signal, ASC system can determine discontinuity types, namely, crack, slag, porosity, and lack of fusion with higher accuracy and consistency.

To achieve optimum accuracy of the ASC system, a significant amount of effort was first focused on reducing the noise in the ultrasonic measurements caused by material grain structure. A multi-stage adaptive noise cancellation (MANC) scheme is proposed for reducing spatially varying grain noise and enhancing flaw detection in ultrasonic signals. This scheme is based on the use of an adaptive least mean square error (LMSE) filter with primary and reference signals derived from two adjacent positions of the transducers. The concept of LMSE filter is also extended to the development of a multistage adaptive wavelet de-noising filtering algorithm.

This thesis also investigates the need for incorporating the effects of beam spread in ultrasonic signal classification. Such effects call for data interpretation schemes based on the information in a neighborhood of A-scans about a reflector. A two-dimensional scan of ultrasonic testing is usually performed resulting in a three-dimensional volume of data (2 spatial and 1 time). Multidimensional signal processing and data fusion algorithms have been developed to analyze the data in Fourier and wavelet transform domains.

1.2 Adaptive Noise Cancellation

In ultrasonic inspection, detection of small flaws is often rendered difficult by the clutter introduced due to the grain structure of the material. The scattering of ultrasonic waves from grain boundaries can interfere and introduce artifacts in the received signal that can sometimes mask indications of a small flaw. For instance, the grain noise can hinder the detection of small but potentially dangerous flaws, such as hard-α inclusions in titanium alloy components [10]. Furthermore, since grain structure typically varies spatially within the material, grain noise can be considered to be a stochastic process [11].

Several signal processing techniques have been developed over the years to reduce grain noise, including spatial averaging [12], bandpass filtering [13], split-spectrum processing [14], and adaptive signal processing [15]. Among these procedures, adaptive signal processing algorithms have gained popularity in recent years primarily due to its ability to handle spatially varying noise in signals. An adaptive grain noise cancellation algorithm for ultrasonic signals using an infinite impulse response (IIR) filter is reported in

[16]. The adaptive filter automatically adjusts its parameters by making use of the correlation between reference and auxiliary inputs from two sensors. However, when the underlying assumptions regarding the correlation properties of signal and noise are not strictly satisfied, the adaptive signal processing (ASP) algorithm can result in sub-optimal performance.

This research proposes a multi-stage adaptive filtering (MAF) scheme for enhancing the signal-to-noise ratio (SNR) by performing grain noise cancellation in stages. At each stage, the filter exploits the statistical correlation properties of grain noise and flaw indications in A-scans obtained from adjacent positions of the transducer. It is shown that each stage of the adaptive noise cancellation (ANC) algorithm not only increases the SNR of the input signal but also reduces the correlation between flaw and noise signals. Consequently, a second stage of ANC further increases the SNR of the signal.

1.3 Multi-dimensional Signal Classification

A second focus of this thesis is ultrasonic testing (UT) signal classification. ASC systems are being used increasingly in nondestructive testing (NDT) largely due to their ability to provide accurate and consistent interpretation of large volumes of data. ASC systems have been used successfully to classify signals obtained from a wide variety of sources, including ultrasonic, eddy current, and magnetic flux leakage signals [17]. In ultrasonic nondestructive testing, a transducer sends an ultrasonic wave into the test sample and receives the reflected wave from discontinuities in the sample. The received energy is converted into an electrical signal by the transducer, resulting in a one-dimensional time domain signal called an A-scan at each transducer position. A raster scan of a two-dimensional area is used to collect A-scan signals. Each position in the raster scan generates a three-dimensional volume of data. Alternate techniques for representing ultrasonic signals are by displaying the collection of A-scans in a line scan to form a two-dimensional image. The B-(axial scan) and B'-scan (circumferential scan) represent a cross-sectional view of the object on a plane that is normal to the surface of the probe. A C-scan image shows the plane view of the test specimen. In order to produce a C-scan, the probe is mechanically scanned over the surface. Typically, the pixel values in C-scan are generated by peak value in each A-scan signal. The amplitude of the reflected signal is used to modulate the intensity of pixels in an image.

In conventional ASC systems, a discontinuity type is determined by using the amplitude and the shape of the A-scan data. A schematic of the generic ASC system is shown in Figure 1.2. The raw NDT signal is applied to a preprocessing block that is used to de-noise the signal and extract features. Noise clutter, caused by the grain structure of the material, often hinders detection of a signal class. Hence, de-noising the signal will enhance the ability of the ASC system to detect small flaws. In order to interpret the signal accurately, we must take into consideration features or invariant attributes of the signal that contain necessary discriminatory information. The feature vectors then becomes inputs to a classification system that provides the result. The classifier, usually a clustering algorithm or a neural network, is first trained to distinguish between the different classes using a training data set. In general, ultrasonic signal classification systems are based on processing individual A-scans [18][19]. In many signal classification applications, the investigation of individual A-scans is the most logical and intuitive way to view signals. Even though these

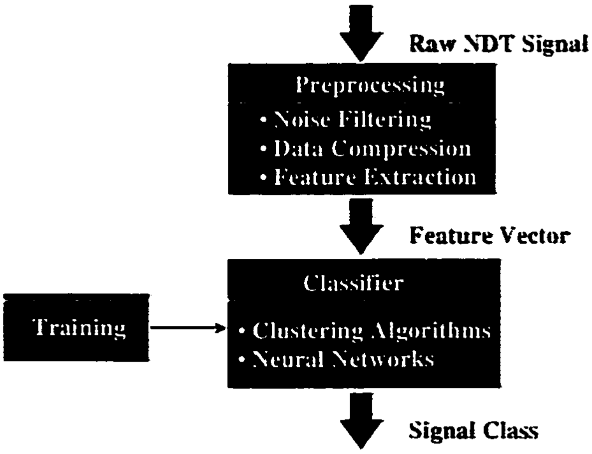

Figure 1.2 A generic automated signal classification scheme.

approaches show reasonable success in ultrasonic testing data analysis, a single A-scan signal itself cannot represent a type of flaw in time, space, or transform domain.

Ultrasound intensity along the beam is not uniform due to the finite aperture of the source that gives rise to diffraction effects [20][21][22][23]. There are extensive fluctuations near the source, known as the near field or Fresnel zone. Because of the variations within the near field, it can be extremely difficult to characterize flaws accurately in materials. The ultrasonic beam is more uniform in the far field or Fraunhofer zone. In this zone, the beam spreads out as if originating from the center of the transducer. Figure 1.3 shows the near/far field zone transition at a distance N that is significant because amplitude variations that characterize the near field change to smoothly declining amplitude as the distance from the transducer increases. The near and far distance measure can be written as

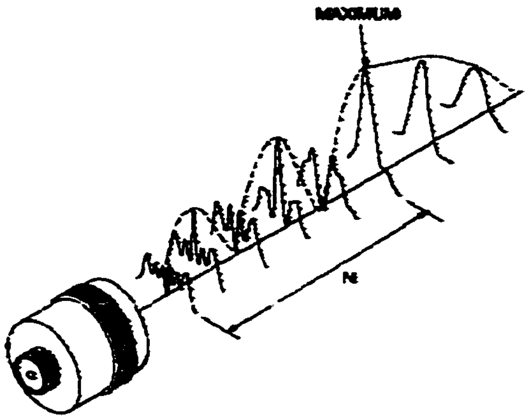

Figure 1.3 The near and far zones of the ultrasonic beam [21].

$$N = \frac{r^2 f}{v} \tag{1.1}$$

where r is the radius of the transducer aperture, f is the frequency of the transducer, and v is the velocity of sound in the liquid or solid medium.

Beam spread is an important consideration in transducer selection [24][25]. It defines how much the beam will spread with distance. Beam spread is largely determined by the frequency of the sound waves. A high frequency transducer produces a narrow beam, and a low frequency transducer produces a wider beam. Due to the beam spread, information about a scatterer is present in a neighborhood of A-scans. Hence, it is important to analyze the B- and B'-scan images collectively and thereby capture the echo dynamics in ultrasonic signals.

The effectiveness of B-scan analysis in showing flaw details depends upon the relationship between the flaw size and beam area. The larger the sound-beam area, the greater the number of small discontinuities illuminated by the sound. Several of these echoes returning at the same time can add and cause an ultrasonic flaw-type indication of rejectible amplitude. It is, therefore, necessary to analyze a neighborhood of signals prior to making a classification decision. Such an approach provides a better estimate of the dynamics in the signal.

Previous work on the classification of a group of A-scans using principal component analysis has been reported in [26], where the statistical variance of a group of A-scans in a neighborhood is computed. Classification is based on the fact that geometric indications in the material do not vary much spatially and consequently have a lower variance than those obtained from irregular flaws. Although this technique is computationally simple, the scheme does not capture all the characteristics of the signal. This thesis investigates the application of wavelet transform to analyze the set of A-scans. Furthermore, it experiments with multi-dimensional Fourier transform for the B- and B'-scan data and three-dimensional moments on the spatial and frequency domain to obtain a final classification for a flaw.

1.4 Organization of the Thesis

Chapter 2 addresses the problem of enhancing signal-to-noise ratio of ultrasonic testing signals. A commonly used technique known as split spectrum processing is first described with a discussion of its limitations. In Chapter 3, the principles of adaptive noise cancellation using finite impulse response (FIR) filters, its extension to the multi-stage adaptive filtering process, and the feasibility of using two adaptive filters in cascade for obtaining improved performance are discussed. Experimental results with regard to various parameters such as effects of filter length, convergence rates, and transducer spacing are also described in this chapter. Additionally an adaptive wavelet de-noising method also is applied to compare the performance of the multi-stage adaptive filtering method. Chapter 4 addresses the problem of ultrasonic signal classification. Previous work based on A-scan classifications with respect to feature extraction and classification schemes are presented. Chapter 5 presents a proposed approach to multi-dimensional signal classification that uses two-dimensional feature vector of B- and B'-scan images as they are applied to the ultrasonic weld inspection. In addition, the principal components use to reduce the dimensionality of a feature vector. Three-dimensional moments also exploit in the spatial and frequency domain. Finally, conclusion and future plans are discussed in Chapter 6.

CHAPTER 2. SPLIT SPECTRUM PROCESSING

Using ultrasonic nondestructive evaluation to detect small flaw signals of a specimen with large microstructures can be a difficult task due to the interference caused by scattering from grain boundaries. Although recent improvements in hardware technology allow transducers to operate at higher frequencies with a smaller focal spot size, the microstructure grain noise in test material cannot be reduced by conventional linear filtering or by time averaging. Several signal processing algorithms have been developed for minimizing the effect of the noise while maximizing the signal. Approaches such as Wiener filtering [27][28], spatial averaging [12], and maximum likelihood estimation [29] have all been utilized for noise suppression in ultrasonic testing. These methods use fixed filters based on a single noise model. However, in many practical applications, noise is usually time varying. Fixed filters, therefore, are in general ineffective in reducing grain noise. Split spectrum processing is a technique proposed in [14] that was shown to be very effective in reducing grain noise. This technique is described in detail below.

2.1 Review of Split Spectrum Processing

In the last decade, split spectrum processing (SSP) was shown to be a very promising tool to enhance the signal-to-noise ratio (SNR) of ultrasonic test signals [30][31][32][33][34][35]. The basic problem with ultrasonic grain noise reduction is that the signal energy of both the flaw and microstructure lies within the same frequency range. Hence, typical filtering techniques, such as a lowpass, highpass, or a single bandpass filter are not effective. Any filter designed to eliminate the microstructure signal would also result in the loss of the flaw signal.

In split spectrum processing, the frequency band containing most of the flaw signal energy is evenly divided into a number of smaller frequency bands. A bank of bandpass filters represents these frequency bands. The bank of filters is applied to an ultrasonic signal, and the minimum output at each point in time is taken as the final output with reduced a microstructure signal and enhanced flaw reflections. Figure 2.1 is a block diagram of split spectrum processing. As illustrated in this diagram, the input x(n) is presented to the bank of bandpass filters. $y_i(n)$, $i=1,2,\ldots,L$, represents individual filter outputs. Once the filter outputs are calculated, the final output value, y(n), is selected to be $\min\limits_{1\le n\le N}\{y_i(n)\}$ for the corresponding point in time n. The algorithm was implemented in frequency domain.

The spectrum of the ultrasonic signal $x(n)$ was obtained using Discrete Fast Fourier transform as

$$X(k) = \sum_{0}^{N-1} x(n) W_N^{kn} \tag{2.1}$$

where $W_N = \exp(-j2\pi / N)$ and N is a length of an ultrasonic signal. Split spectrum processing splits the spectrum into different frequency bands using Gaussian filters defined by

$$G_i(k) = (2\pi\sigma^2)^{-1/2} \exp\left[-\frac{(k-f_i)^2}{2\sigma^2} \right] \tag{2.2}$$

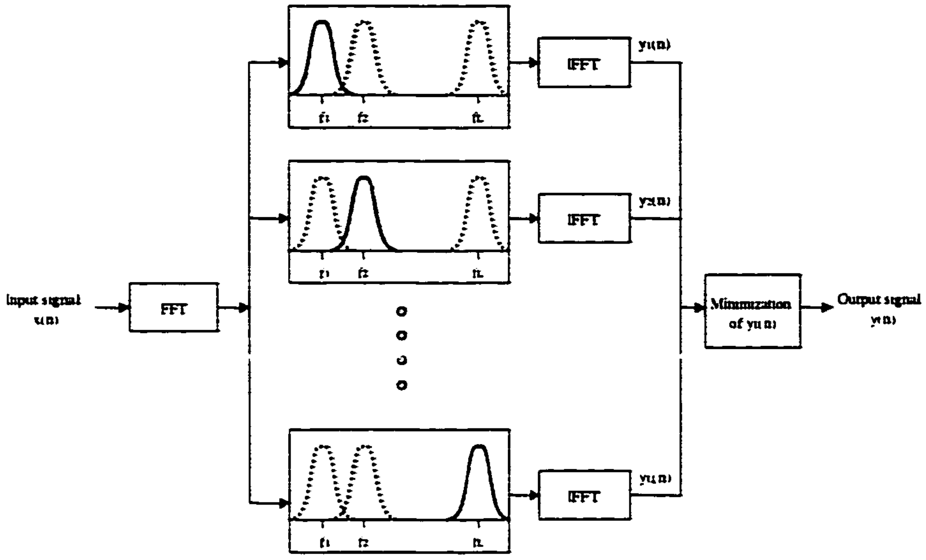

Figure 2.1 A block diagram for split spectrum processing.

where f_i is the mean frequency and σ^2 is the variance of the Gaussian filter. Theoretically, a time limited signal produces an infinite bandwidth. However, because of the frequency response of the ultrasonic signal, the optimal frequency region selection is limited to a frequency band of B Hz defined by $[f_{lower}, f_{upper}]$ as shown in Figure 2.2. Thus, the number of frequency bands $N_{Gaussian}$ is

$$N_{Gaussian} = BT \tag{2.3}$$

where T is the total time duration of the ultrasonic signal. The optimum frequency separation of two successive filters is

$$\Delta f = \frac{f_{upper} - f_{lower}}{N_{Gaussian} - 1} \text{Hz} \tag{2.4}$$

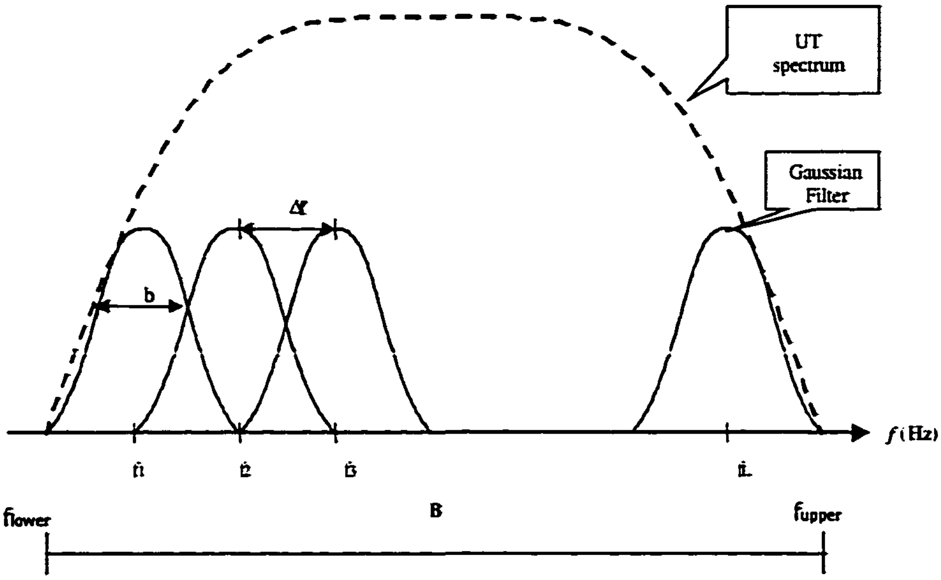

Figure 2.2 Split spectrum filtering scheme.

Figure 2.2 shows the filtering scheme of the original wide-band signal. The center frequencies of the Gaussian filters are selected so that they fall within the usable limited bandwidth B. Therefore, the filter center frequencies are defined as

$$f_i = f_{lower} + (i-1)\Delta f, \quad i = 1,2,\ldots,L \tag{2.5}$$

where L is the number of Gaussian filters. The Gaussian filters were used to split the spectrum into several overlapping bands so that none of the frequency components of the original signals are lost in the processing.

The output of the overlapping Gaussian filters with different center frequencies consist of the different split spectra, $Y_i(k)$, $i = 1,2,\ldots,N_{Gaussian}$. The time domain signal of each individual frequency bands can be found by computing inverse Fourier transform, which can be written as

$$y_i(n) = \frac{1}{N}\sum_{0}^{N-1} Y_i(k)W_N^{-kn}, \quad i = 1,2,\ldots, N_{Gaussian}. \tag{2.6}$$

Finally, the time domain signals from each individual frequency band are then passed through a minimization stage, and the final output signal is computed as

$$y(n) = \min_{1\le i\le L}\left[y_i(n)\right] \quad n = 1,2,\ldots, N. \tag{2.7}$$

The basic objective of this technique is to suppress the reflection from grain boundaries while retaining the flaw echo. The signals from rain boundaries, in general, are random and uncorrelated signals [14]. Hence the reflection from grain boundaries interferes to produce a resultant signal whose net phase and amplitudes depends more strongly on frequency than a flaw signal. Due to this sensitivity of grain echoes on the frequency band, a minimization method rather than averaging is more effective in suppressing the grain noise in the final output. Therefore, split-spectrum processing technique can enhance the signal-to-noise ratio while suppressing the grain noise signals.

2.2 Limitations of Split Spectrum Processing

Split-spectrum processing (SSP) methods are sensitive to filter parameters such as center frequency f_i of the filters, the center frequency spacing Δf, Gaussian filter variance σ, and the minimization scheme. In this section, we analyze limitations of the SSP technique using a synthetic signal.

2.2.1 Effect of α and Minimization Scheme

Consider a synthetic windowed sine wave $x(n)$ of frequency 50 Hz expressed as

$$x(n)=\begin{cases}0, & 0\le n<250\\ \sin(2\pi fn), & 250\le n\le 350\\ 0, & 351\le n\le 600.\end{cases} \tag{2.8}$$

Adding Gaussian noise to the signal, we get the signal model equation

$$y(n)=x(n)+\eta(n) \tag{2.9}$$

where $\eta(n)$ is an additive Gaussian noise of zero mean and variance 2. The signal $y(n)$ is plotted in Figure 2.3. The input signal $y(n)$ is of a length of 601 samples obtained at 1000 Hz sampling frequency. Consequently, the total time duration (T) of the ultrasonic signal is 0.601 seconds. As can be seen in Figure 2.4, most of the signal energy lies in the frequency range 40 ~ 60 Hz, giving a valuable bandwidth B of 20 Hz. In general, the variance of Gaussian filters (σ) is constant and can be expressed as

$$b=\sigma^2=\alpha*\Delta f \tag{2.10}$$

where α is a scaling factor used for determining the width of Gaussian filters. Based on the separation of the filters, Δf must be chosen as 1.8182 Hz using Equation (2.3).

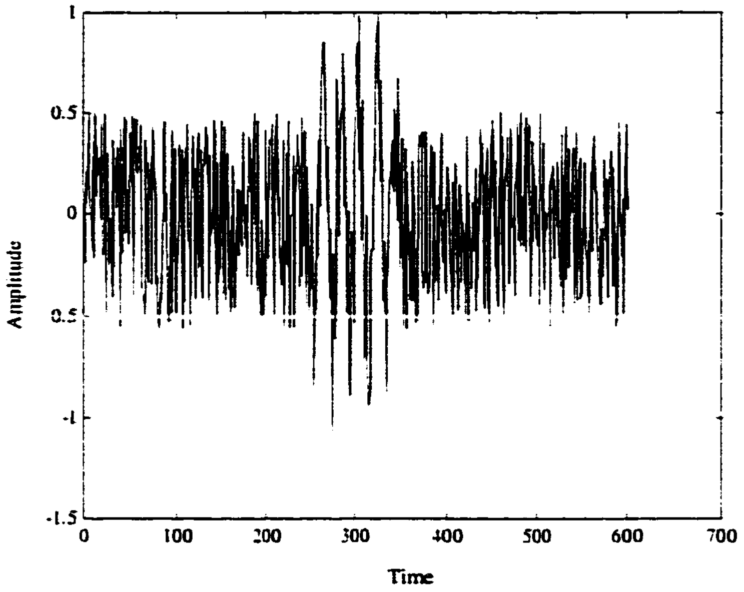

Figure 2.3 The input signal for split spectrum processing.

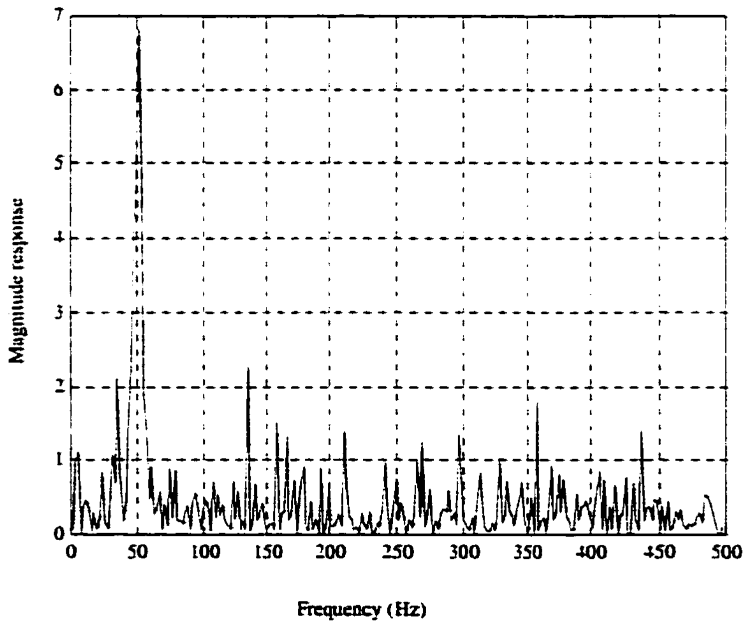

Figure 2.4 The frequency response of the input signal in Figure 2.3.

Figure 2.5 shows the effect of α on the filter output. As shown in Figure 2.5-(a) and (b), for small values of α, the SSP outputs are not enhanced. If α is less than the frequency spacing Δf, the Gaussian filters are non-overlapping. This means that the frequencies in between two neighboring Gaussian filters are passed without filtering. Therefore, the α value should be selected to be greater than Δf. In this example, the value of α must be greater than 2. Also, too large a value of α can make the shape of Gaussian filters asymmetrical when the value of α is greater than 8. Therefore, the optimal value of α is chosen to be 4 and the variance b is 7.2727 in this experiment. Figure 2.6 shows the output using the SSP technique. In Figure 2.6-(a), the final output of the SSP filters is obtained by selecting the minimum output according to Equation (2.7). The use of an alternate minimization algorithm called the polarity minimization scheme produces the output shown in Figure 2.6-(b). The polarity minimization scheme can be described in the following equation.

$$y_{out}(n) = \begin{cases} \max\{|y_i(n)|, i = 1,2,\ldots,N\} & \textit{if } \text{for } i,\ y_i(n) < 0 \ \textit{or} \ y_i(n) > 0 \\ 0 & \textit{else} \end{cases} \tag{2.11}$$

In polarity thresholding, the output is set to the maximum magnitude value of the ensemble if there is no polarity change. Otherwise, the output is assigned to zero. Correlated peaks, a likely indication of the presence of a target, will be maximized in amplitude, otherwise the amplitude value is set to zero. Figure 2.7 shows the result obtained using a single bandpass filter with passband frequency range [40 ~ 60 Hz]. As seen in this result, the multiple bandpass filters within the usable spectral range provide better SNR than those obtained using a single bandpass filter.

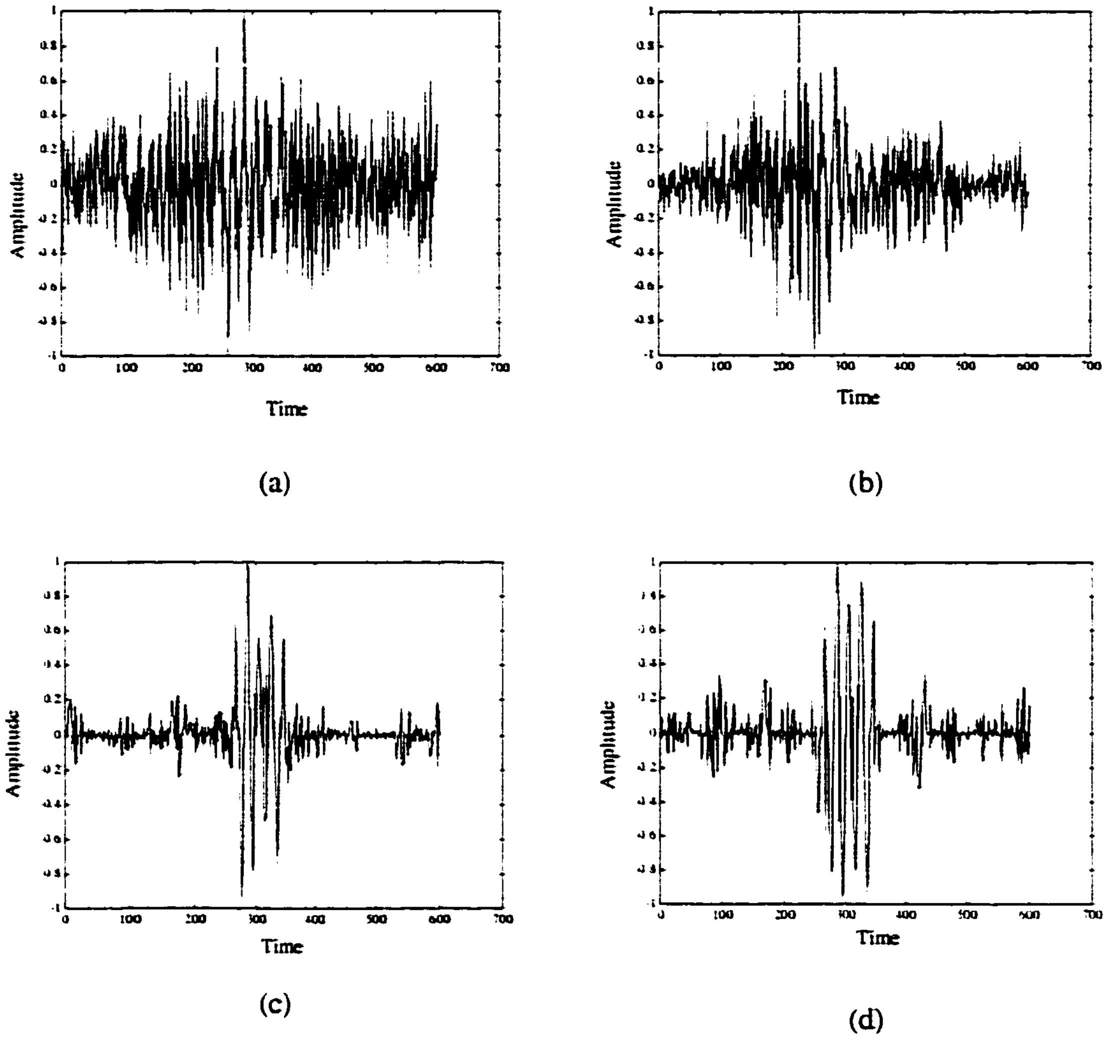

(a) (b)

(c) (d)

Figure 2.5 Output of SSP with different values of α (a) α=0.5, (b) α=1, (c) α=4, and (d) α=8.

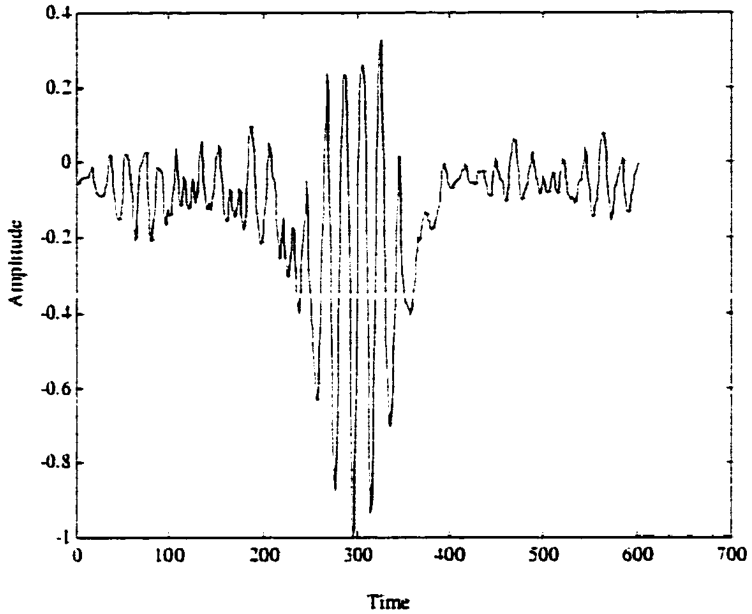

(a)

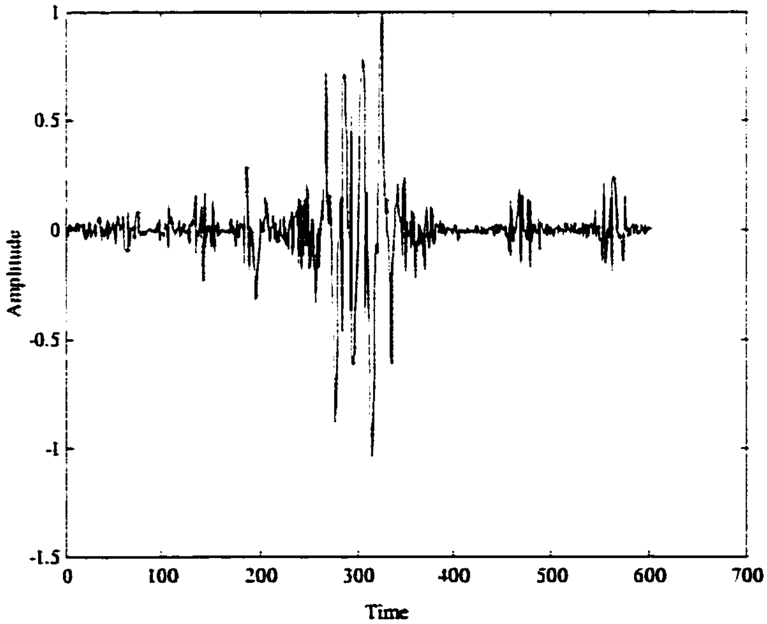

(b)

Figure 2.6 Output of SSP using (a) conventional minimization scheme and (b) polarity minimization scheme.

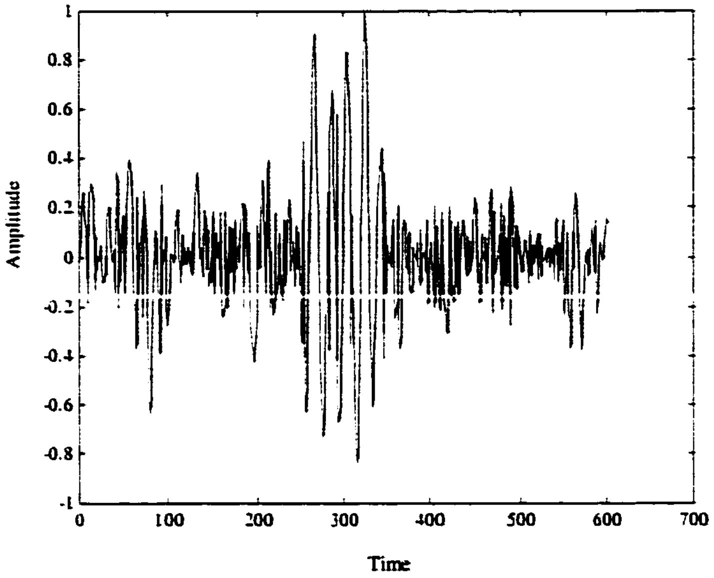

Figure 2.7 SSP results using single bandpass filter N=1.

2.2.2 Signals with Two Distinct Frequencies

Suppose a signal $x(n)$ is composed of two sinusoids of frequencies 50 Hz and 120 Hz, as described below:

$$x(n) = \begin{cases} 0, & 0 \le n < 250 \\ \sin(2\pi f_1 n) + \sin(2\pi f_2 n), & 250 \le n \le 350 \\ 0, & 351 \le n \le 600 \end{cases} \tag{2.12}$$

Adding a Gaussian noise of zero mean and variance 2 to the signal $x(n)$, the resultant signal with noise can be expressed as in Equation (2.9). The input signals, $x(n)$ and $y(n)$ are plotted in Figure 2.8-(a) and (b), respectively. Again, the input signal $y(n)$ is of a length of 601 samples obtained at 1000 Hz sampling frequency, and the total time duration (T) of the ultrasonic signal is 0.601 seconds. In Figure 2.8-(c), most of the signal energy lies in the frequency range 40 ~ 130 Hz, and the bandwidth of the usable spectrum becomes 90 Hz. Therefore, the number of Gaussian filters ($N_{Gaussian}$) is 54 using Equation (2.3). According to Equation (2.4), the optimum frequency separation of the filters Δf must be chosen as 1.6981 Hz. The variance b of 6.7925 with the scaling factor α of 4 is used for determining the width of Gaussian filters.

The result of SSP is shown in Figure 2.8-(d). The output of SSP fails when the input signal contains two significant frequencies as seen in Figure 2.8-(d). Since the most dominant energy bands are two separate frequency ranges, 40 ~60 Hz and 110 ~ 130 Hz, the final result is not as desirable as when the range is chosen as 40 ~ 130 Hz. This result clearly shows that the SSP technique works only when the target frequency is contained in a single wideband. Also, when the target and noise frequencies are very close, the technique is not very effective in selectively reducing the noise as will be shown in the next chapter.

2.2.3 Effect of $f_2 - f_1$

In order to analyze the effect of an interval between two distinct frequencies, the split-spectrum processing technique was implemented on signals containing two frequencies f_1 and f_2. Using Equation (2.12), test signals were generated with f_1 = 50 Hz and various f_2 values for 60, 70, and 80 Hz.

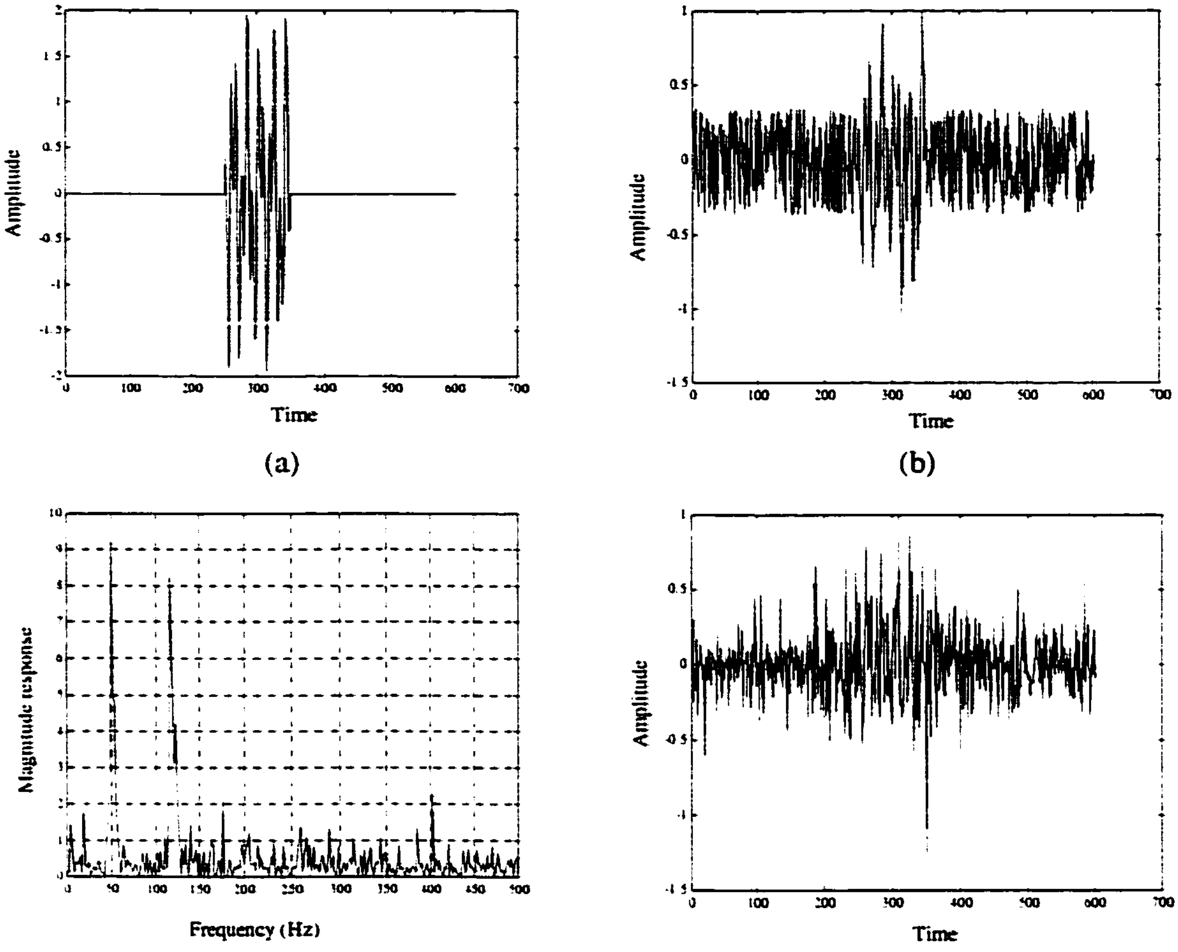

(a) (b)

(c) (d)

Figure 2.8 SSP result with two frequencies. (a) an original input signal x(n), (b) a signal added zero mean and variance 2, (c) spectrum of *y(n)*, and (d) output signal.

The results of implementing SSP on the test signals are shown in Figures 2.9. The original input signals are presented in the top row. Adding a Gaussian noise of zero mean and variance 2 to the original signal, the resultant signal with noise and its spectrum are shown in the second and third rows, respectively. The usable frequency range for the SSP process is obtained from the spectra of noisy signals.

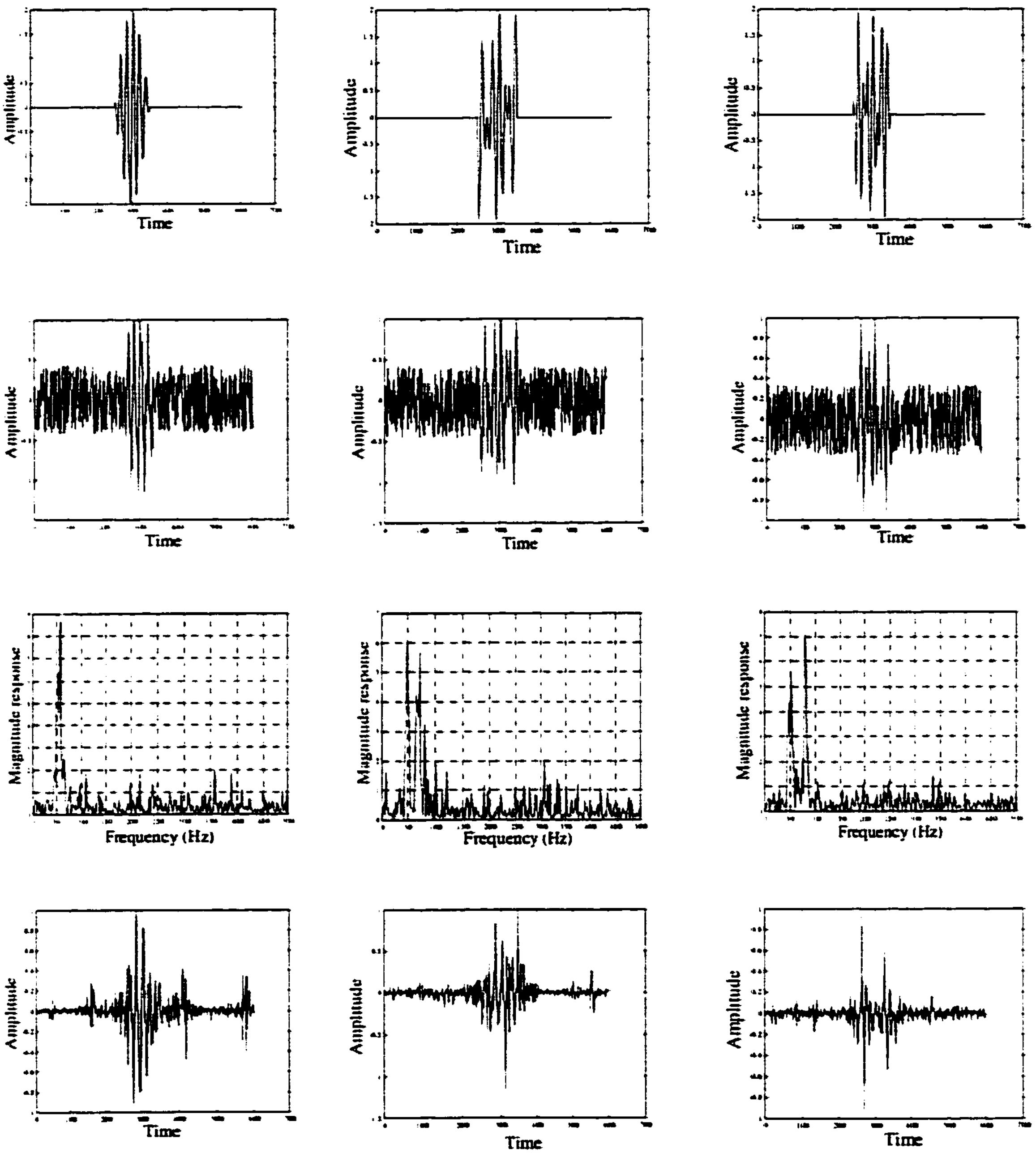

(a) (b) (c)

Figure 2.9 SSP results using various values of Δf with f_1=50 Hz. Values of f_2 in Hz are (a) 60, (b) 70, and (c) 80.

The SSP parameters used in this experiment are summarized in Table 2.1. The last row in Figure 2.9 shows the results of split-spectrum processing. In the case (f_2=60 Hz and f_2=70 Hz), the outputs of split-spectrum processing showed a reduction of noise components while retaining the original signal. However, at other frequencies of f_2 the results show not only a suppression of noise components but also loss of the original signal.

We have reviewed some limitations of the split-spectrum processing technique. For SNR enhancement, the SSP technique has proved to be effective in noise suppression but only under certain conditions. For example, the method fails if the signal is composed of multiple frequencies.

Table 2.1 The parameter values used to compare the effect of f_2-f_1 (The scaling factor is shown to be 4 and f_1=50 Hz). B stands for the limited bandwidth on split-spectrum processing.

f_2	B (Hz)	Δf	$b = \sigma^2$	$N_{Gaussian}$
60	[40.70]	1.7647	7.0588	18
70	[40.80]	1.7391	6.9565	24
80	[40,90]	1.7241	6.8965	30

CHAPTER 3. MULTI-STAGE ADAPTIVE NOISE CANCELLATION

3.1 Adaptive Least Mean Square Error (LMSE) Filter

Noise cancellation algorithms with optimal filter weights can be fixed or adaptive, depending on the prior knowledge of signal characteristics. In many cases, the complete range of input conditions may not be known exactly or the conditions may vary with time. In such circumstances, an adaptive system that continually seeks the optimum within an allowed range of possibilities offers a much higher level of performance than fixed filters.

Adaptive noise cancellation (ANC) algorithms estimate the impulse response of the filter using an iterative procedure to minimize the error between the filter output and primary input. The simplest adaptive filtering technique uses an LMSE finite impulse response (FIR) filter to perform the noise cancellation. Although FIR adaptive systems converge rather slowly to an optimal state, it is nevertheless used in adaptive systems due to its simplicity and ease of implementation.

Figure 3.1 shows a block diagram representation of a single stage adaptive filter with reference input $u_1(n)$ and primary input $d_1(n)$. The reference input, in general, represents a pure noise signal if available and fixed. In conventional ANC algorithms, the reference input is filtered and subtracted from the primary input containing both signal and noise. The filter in Figure 3.1 is adaptive in that it automatically adjusts its impulse response to minimize the error signal. When this algorithm is applied to ultrasonic nondestructive evaluation (NDE), where the noise is spatially varying, the primary input and reference signals are obtained

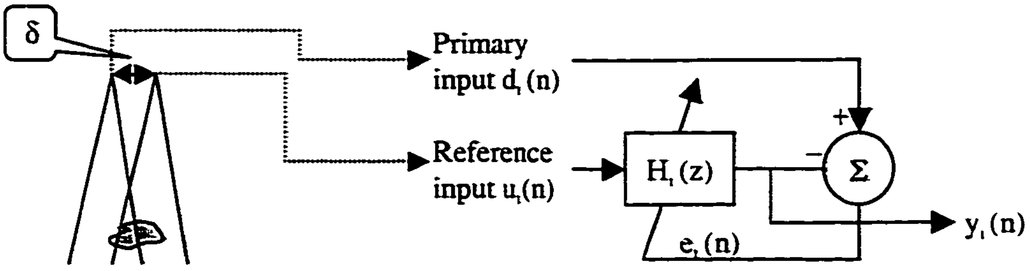

Figure 3.1 Schematic of the adaptive noise cancellation system for ultrasonic NDE [15].

from two adjacent positions of the transducer. $u_1(n)$ and $d_1(n)$ can be obtained from two transducers distance δ apart or alternately by choosing $u_1(n)$ to be a time-delayed version of primary input $d_1(n+\delta)$. In general, a measured signal can have both flaw and noise components. Suppose the primary input signal $d_1(n)$, consists of a flaw component $f_{d_1}(n)$ and noise component $n_{d_1}(n)$.

$$d_1(n) = f_{d_1}(n) + n_{d_1}(n) \tag{3.1}$$

and correspondingly the reference signal is expressed as a sum of flaw and noise components $f_{u_1}(n)$ and $n_{u_1}(n)$ respectively.

$$u_1(n) = f_{u_1}(n) + n_{u_1}(n). \tag{3.2}$$

The underlying assumptions in this algorithm (summarized in Table 3.1) is that the noise components, $n_{d_1}(n)$ and $n_{u_1}(n)$ from the grain structure are uncorrelated with both

Table 3.1 Assumptions of correlation between primary and reference input signals made by an adaptive noise cancellation algorithm.

		Reference signal $u_1(n) = f_{u_1}(n) + n_{u_1}(n)$	
		f_{u_1}	n_{u_1}
Primary signal $d_1(n) = f_{d_1}(n) + n_{d_1}(n)$	f_{d_1}	correlated	uncorrelated
	n_{d_1}	uncorrelated	uncorrelated

$f_{d_1}(n)$ and $f_{u_1}(n)$ whereas the flaw indications $f_{d_1}(n)$ and $f_{u_1}(n)$ are correlated. The mean square error (MSE$_1$) between filter output, $y_1(n)$, and primary input, $d_1(n)$, is given by

$$\begin{aligned} MSE_1 &= E\left[e_1^2(n)\right] = E\left[(d_1(n) - y_1(n))^2\right] \\ &= E\left[(f_{d_1}(n) - y_1(n) + n_{d_1}(n))^2\right] \end{aligned} \tag{3.3}$$

If the impulse response of the filter is represented by $h_1(n)$, we have $y_1(n) = h_1(n) * u_1(n) = h_1(n) * f_{u_1}(n) + h_1(n) * n_{u_1}(n) = f_{y_1}(n) + n_{y_1}(n)$. Substituting back in Equation (3.3), the MSE$_1$ can be written in the form.

$$\begin{aligned} MSE_1 &= E\left[(f_{d_1}(n) - f_{y_1}(n))^2\right] + E\left[(n_{d_1}(n) - n_{y_1}(n))^2\right] \\ &+ 2E\left[(f_{d_1}(n) - f_{y_1}(n))(n_{d_1}(n) - n_{y_1}(n))\right] \end{aligned} \tag{3.4}$$

The optimum filter coefficients are determined when MSE$_1$ is minimized. If the noise and flaw signals are uncorrelated, the expected value of the last term is zero. Suppose $f_{u_1}(n)$ is simply a time-delayed version of $f_{d_1}(n)$, (say $f_{d_1}(n - n_0)$).

During adaptation, the filter coefficients are adjusted to $h_1(n+n_0)$, and the first term in Equation (3.4) goes to zero. The minimum error MSE$_1$ in this case is $E\left[(n_{d_1}(n)-n_{y_1}(n))^2\right]$, and the filter output is close to zero. If the primary and reference inputs have both target and noise, the filter minimizes the error $E\left[(f_{d_1}(n)-h_1(n)*f_{u_1}(n))^2\right]+ E\left[(n_{d_1}(n)-h_1(n)*n_{u_1}(n))^2\right]$, and the filter output has a lower noise component. In other words, the signal-to-noise ratio (SNR) is increased.

Adaptive algorithms in general are based on optimizing a certain cost function. In the case of the LMS algorithm, the cost function is the Mean Square Error (i.e. the mean square value of the error signal). The LMSE algorithm is the simplest and the most commonly used technique [36][37][38] for estimating the filter weights. This is achieved by adjusting the values of the weights of the FIR filter in such a way that the cost function is minimized. Typical methods for reaching the minimum value include the gradient and steepest descent techniques.

The input-output relationship of the FIR filter is given by

$$y_1(k)=\sum_{n=0}^{L}h_{1,n}(k)u_{1,k-n} \tag{3.5}$$

where $h_{1,n}(k)$ are the time-varying characteristic filter coefficients, $u_{1,k}$ is the reference input, $y_1(k)$ is the output, and L is a filter length. In the steepest descent method for updating filter coefficients, we have

$$h_{1,k+1}=h_{1,k}+2\mu e_k u_{1,k},\ k=1,2,3,\ \ldots N \tag{3.6}$$

where μ is the convergence parameter, e_k is the error signal, $u_{1,k}$ is the reference input signal, and N is the signal length. The convergence parameter plays an important role in determining the performance of an adaptive system. Its value is important since it affects the speed of convergence and the stability of the LMS algorithm. Since there are no general rules for selecting the convergence factor μ, we use a value that is stable for a given input signal power. In general, the normalized convergence factor [39][40][41] is selected according to

$$\mu_n = \frac{\mu}{(1+L)\sigma^2}, \qquad 0<\mu<1 \tag{3.7}$$

where $(1+L)$ is the number of filter coefficients and σ^2 is the input signal power. In many applications, we need to estimate the signal power, which can be obtained as

$$\hat{\sigma}_k^2 = \alpha u_{1,k}^2 + (1-\alpha)\hat{\sigma}_{k-1}^2, \qquad 0 \le \alpha << 1 \tag{3.8}$$

where α is a "forgetting factor" used to reduce the influence of the past inputs. Substituting the normalized convergence parameter and estimated signal power in Equation (3.6), we get

$$h_{1,k+1} = h_{1,k} + \frac{2\mu e_k u_{1,k}}{(1+L)\hat{\sigma}_k^2}, \qquad 0<\mu<1. \tag{3.9}$$

In the LMSE algorithm, parameters, α, μ, and L, should be chosen optimally so that the performance of the adaptive filter is satisfactory. However, the convergence parameter μ

will depend on the design specifications and computing time. The goal of the adaptive process is to adjust the filter coefficients in such a way that they move from any initial condition to the minimum mean-square-error solution. Within the convergence rate margin, the larger the value of μ, the faster the convergence, but less the stability around the minimum value. On the other hand, the smaller the value of μ, the slower the convergence, but more the stability around the optimum value. In practical applications, however, we are dealing with non-stationary signals, and as signal conditions change, the adaptive process must continually update the coefficients in order to track the LMSE solution. It is, therefore, assumed that the signals are slowly varying satisfying stationary requirements.

3.2 Multi-stage Adaptive Filter

The performance of conventional adaptive noise cancellation techniques depends strongly on the statistical correlation properties of flaw and grain noise signals. If these assumptions are not fully satisfied, the algorithms result in a sub-optimal performance of the system in improving the SNR of the ultrasonic data. In this thesis, we propose a multi-stage adaptive filtering method to suppress the noise level in stages. Figure 3.2 shows two stages of the proposed multi-stage adaptive noise cancellation method. The purpose of the first stage is to obtain a signal with improved SNR and also better correlation properties, i.e., high correlation between flaw signal components and less correlation between the noise components, thereby enabling significantly superior performance in the second stage. The output of the first stage adaptive filter serves as the input to the second stage adaptive filter.

The input-output relationship of the second adaptive filter $H_2(z)$ is the same as that described in the previous section. The filter output $y_2(n)$ of the second stage can be represented as

$$\begin{aligned} y_2(n) &= h_2(n) * y_1(n) \\ &= h_2(n) * f'_{y_1}(n) + h_2(n) * n_{y_1}(n) \\ &= f_{y_2}(n) + n_{y_2}(n) \end{aligned} \tag{3.10}$$

where $h_2(n)$ is the impulse response of the second stage adaptive filter. The MSE associated with the second stage is given by:

$$\begin{aligned} MSE_2 &= E\left[e_2^2(n)\right] = E\left[(d_2(n) - y_2(n))^2\right] \\ &= E\left[(f_{d_1}(n) - f_{v_2}(n))^2\right] + E\left[(n_{d_1}(n) - n_{y_2}(n))^2\right] \\ &\quad + 2E\left[(f_{d_1}(n) - f_{v_2}(n))(n_{d_1}(n) - n_{v_2}(n))\right] \end{aligned} \tag{3.11}$$

where $d_2(n) = d_1(n) = f_{d_1}(n) + n_{d_1}(n)$. The optimal filter minimizes the MSE$_2$. As explained in the earlier section, if $f_{u_1}(n)$ is simply a time-delayed version of $f_{d_1}(n)$, the MSE$_2$ is given by $E\left[(n_{d_1}(n) - n_{v_2}(n))^2\right]$. In the second stage of MANC, in general, the minimum $MSE_2 > MSE_1$ because of using $d_2(n) = d_1(n)$ and the filter output $n_{y_2}(n) < n_{y_1}(n)$. This ensures that the MSE and SNR increase monotonically in successive stages. This treatment can be extended similarly to m-stages, where the output can be written as

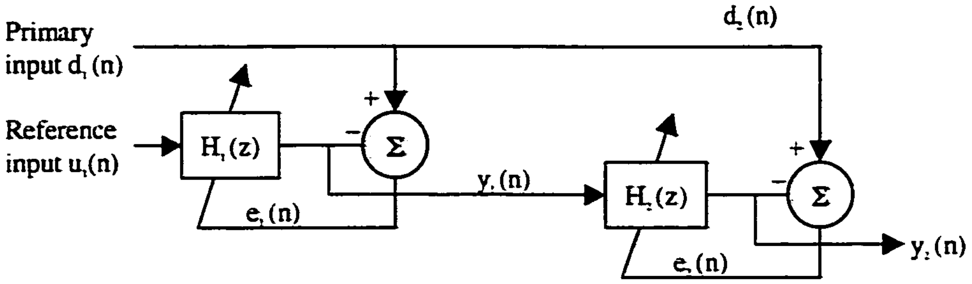

Figure 3.2 Configuration of multi-stage adaptive noise cancellation filter (Method I).

$$
\begin{aligned}
y_m(n) &= h_m(n) * y_{m-1}(n) = h_m(n) * f_{y_{m-1}}(n) + h_m(n) * n_{y_{m-1}}(n) \\
&= f_{y_m}(n) + n_{y_m}(n)
\end{aligned}
\tag{3.12}
$$

and the minimum error is

$$
\begin{aligned}
MSE_m &= E\left[e_m^2(n)\right] = E\left[(d_m(n) - y_m(n))^2\right] \\
&= E\left[(f_{d_1}(n) - f_{y_m}(n))^2\right] + E\left[(n_{d_1}(n) - n_{y_m}(n))^2\right] \\
&\quad - 2E\left[(f_{d_1}(n) - f_{y_m}(n))(n_{d_1}(n) - n_{y_m}(n))\right]
\end{aligned}
\tag{3.13}
$$

where $d_m(n) = d_1(n) = f_{d_1}(n) + n_{d_1}(n)$ and $MSE_m > MSE_{m-1} > \cdots > MSE_2 > MSE_1$.

Figure 3.3 shows an alternate configuration for multi-stage adaptive filtering in which the primary and reference inputs are selected from the processed image at the output of the first stage. The relationship between the primary and reference inputs at the first and second adaptive filters is summarized in Table 3.2. In this method, the output of each stage is similar to Equation (3.4) and the mean square error is expressed for an M-stage system as

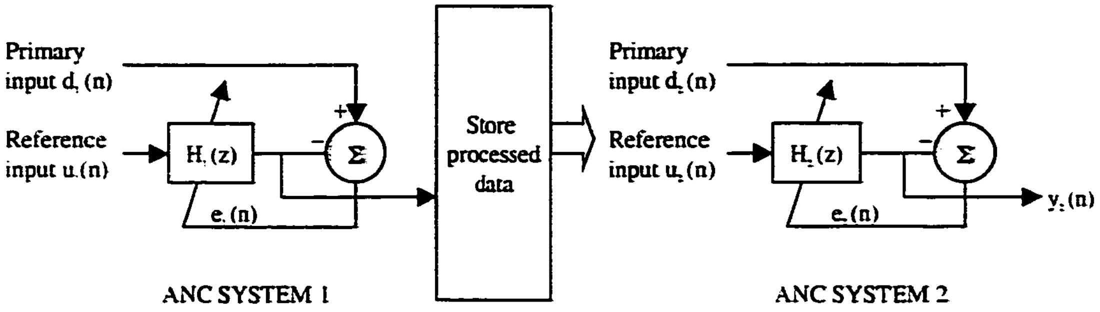

Figure 3.3 Alternate configuration of multi-stage adaptive noise cancellation filter (Method II).

$$\begin{aligned} MSE_i &= E\left[e_i^2(n)\right] = E\left[(d_i(n) - y_i(n))^2\right] \\ &= E\left[(f_{d_i}(n) - f_{y_i}(n))^2\right] + E\left[(n_{d_i}(n) - n_{y_i}(n))^2\right] \quad i=1,2,\ldots,M. \qquad (3.14) \\ &\quad - 2E\left[(f_{d_i}(n) - f_{y_i}(n))(n_{d_i}(n) - n_{y_i}(n))\right] \end{aligned}$$

such that, in this case, $MSE_2 < MSE_1$.

3.3 Experimental Data and Results

The signal processing algorithms described here were applied to real ultrasonic testing data with grain noise. The test specimen is a Ti block of ½" width, 4" length and 4" depth shown in Figure 3.4. It contains two synthetic Ti64 2.7% Nitrogen hard-α inclusions.

Table 3.2 Relation between primary and reference inputs in the two stages in Method II (Figure 3.3).

	Primary signal	Reference signal
ANC system 1	$d_1(n) = d_1(n-\delta)$	$u_1(n) = d_1(n)$
ANC system 2	$d_1(n) = d_1(n)$	$u_1(n) = d_1(n+\delta)$

which are located one inch below the surface. The signals are obtained using a 10 MHz, 0.75" diameter, and 8" focal length wideband transducer. The length of the A-scan is 1024 samples obtained at 100MHz sampling rate collected using a transducer step size of 0.008". The front surface reflection is eliminated, and a typical C-scan image from the sample is shown in Figure 3.4. The bright circles near (30,30) and (30,90) represent indications of the hard-α inclusions. The highly granular microstructure of the material generates strong interference noise in the ultrasonic signal as seen in Figure 3.4-(a). Typical A-scans from 2 pixels located at (33, 28) and (33, 90) are shown in Figure 3.4-(b).

The two-stage ANC algorithm was applied to the data in Figure 3.4. Factors that affect the performance of the algorithm are (i) distance between transducer positions δ, (ii) convergence rate μ, and (iii) filter length L. The performance in each case was evaluated in terms of two parameters, namely the SNR and the correlation properties. The correlation properties of the input data and the processed signals at the output were studied by computing the cross-correlation coefficient

$$\rho_{\mathbf{du}} = \frac{\mathrm{cov}(\mathbf{d},\mathbf{u})}{\sqrt{\mathrm{cov}(\mathbf{d}) * \mathrm{cov}(\mathbf{u})}}. \tag{3.15}$$

where **d** and **u** are the two input vectors and cov(•) represents the covariance.

In evaluating the performance of the multi-stage adaptive filter, it is helpful to define signal-to-noise ratio in a manner that takes into account the burst nature of the desired flaw signal and the cross-correlation of the two inputs. In order for the adaptive LMSE algorithm to perform optimally, we require high correlation in the flaw area and low correlation in the

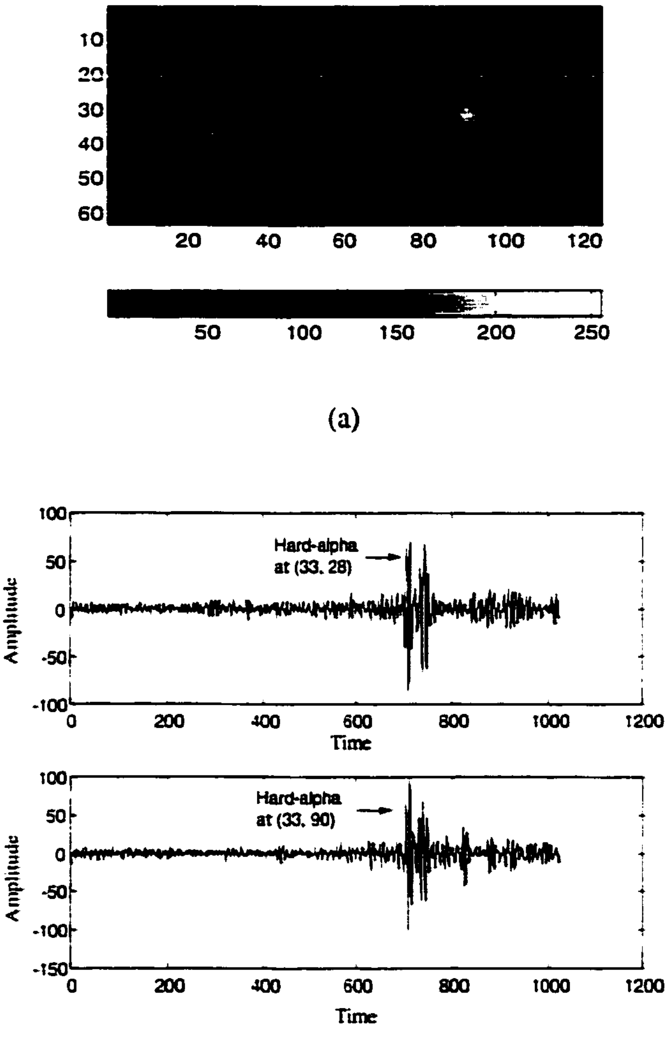

Figure 3.4 Experimental data. (a) ultrasonic C-scan data from Ti samples with synthetic hard-α inclusions and (b) typical A-scans from 2 pixels located at (33, 28) and (33, 90).

background pixels. Although there are several definitions for signal-to-noise ratio (SNR), a modified SNR_{flaw} function that is focused on the flaw signal [15] (see Figure 3.5) is defined as

$$SNR_{flaw} = 10\log\left(\frac{\frac{1}{N_s}\sum_{k=M-N_s/2}^{M-1+N_s/2} y^2(k)}{\frac{1}{M_{d_1}}\sum_{k=1}^{M_{d_1}} y^2(k) + \frac{1}{L-M_{d_2}}\sum_{k=M_{d_1}+N_s}^{L-(M_{d_1}+N_s)} y^2(k)}\right). \tag{3.16}$$

where M is the target location. N_s is the target signal duration. M_{d_1} and M_{d_2} define the target signal duration comprising N_s data points. These parameters are obtained manually through a visual examination.

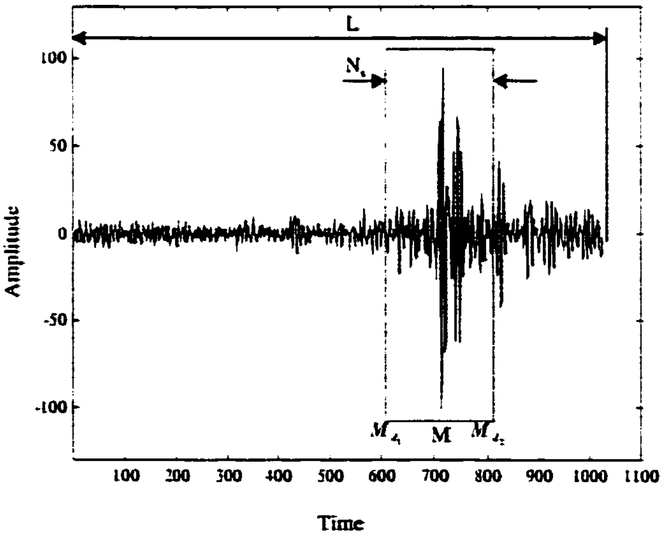

Figure 3.5 Parameters L, N_s, M_{d_1}, M_{d_2}, and M used in definition of SNR at a flaw.

3.3.1 Split Spectrum Processing Implementation

For the SSP implementation, the parameter values described in Chapter 2 are summarized in Table 3.3. The result of implementing the SSP algorithm on the hard-α inclusion signal is shown in Figure 3.6. The results of SSP on both grain as well as flaw signal show that the method is not applicable to this problem. Although the noise seems to be somewhat reduced, the processed noise signal contains only two significant peaks that can be misinterpreted. Therefore, it is necessary to use the correlation properties of hard-α and grain reflections to suppress the noise component. The following sections describe the performance of a multi-stage adaptive noise cancellation scheme on the data shown in Figure 3.4. A detailed study of the effect of the parameters – filter length, learning rate, and transducer distance on the performance – is also described.

3.3.2 Effect of Filter Length

The MAF system was implemented using FIR adaptive filters of varying filter lengths in the first and second stage represented by L_1 and L_2, respectively. Three combinations of

Table 3.3 The parameter values for SSP method.

	f_{lower}	f_{upper}	B	T	$N_{Gaussian}$	Δf	B
Hard-α	10MHz	15MHz	5MHz	10.24μs	51	100KHz	400KHz
Grain	10MHz	13MHz	3MHz	10.24μs	31	100KHz	400KHz

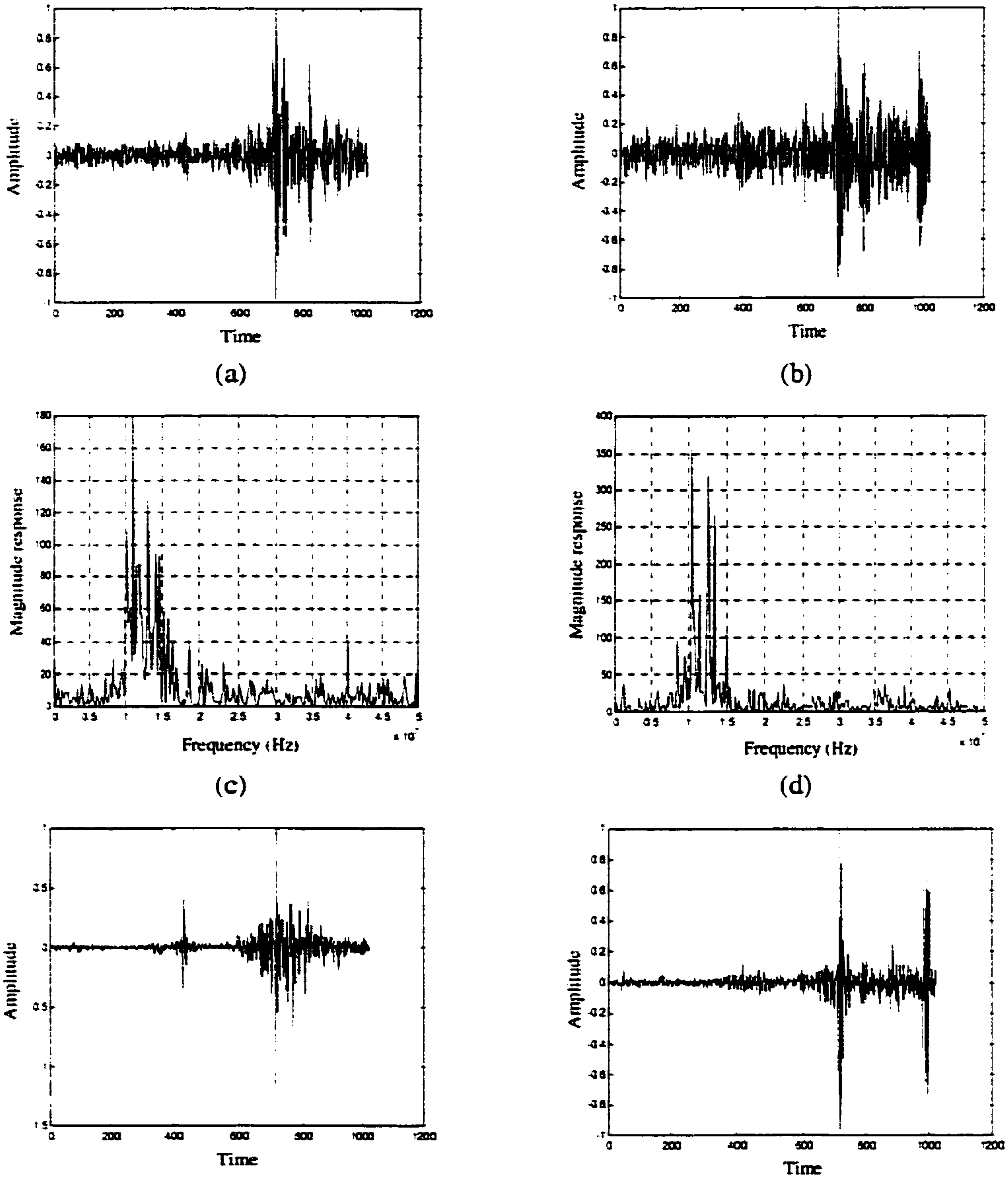

(a) (b)

(c) (d)

(e) (f)

Figure 3.6 The left side figures show (a) input signal (target+noise), (c) spectrum, and (e) output signal for Hard-α signal. The right side figures show (b) input signal (noise only), (d) spectrum, and (f) output signal for grain noise signal. The input signals are located at (30, 90) and (50,87) in Figure 3.4.

$[L_1, L_2]$ were selected namely, (i) $[L_1, L_2] = [3, 5]$, (ii) $[L_1, L_2] = [7, 7]$, and (iii) $[L_1, L_2] = [7, 9]$ using a learning rate $\mu_1=\mu_2=0.1$. The reduced noise signals at the output of the first and second stage are plotted in Figures 3.7 to 3.9. The primary and reference input signals were captured with transducers placed 0.016" apart. Both signals contain flaw and grain noise components. The results were evaluated using improvements in the SNR and correlation in each stage, which are summarized in Table 3.4. The results clearly show the advantage of using a two stage adaptive filter. The choice of filter length L_1 does not greatly affect the result of the output of the first stage in terms of both SNR and correlation coefficient ρ. However, the results indicate that the choice of L_2 has a significant effect on the SNR of

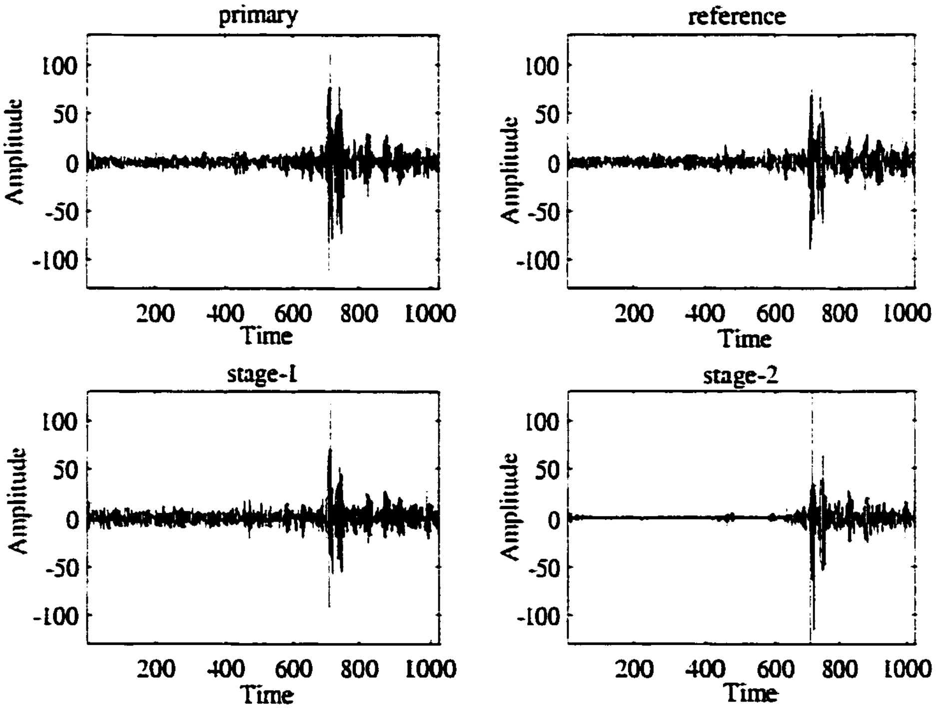

Figure 3.7 Results using adaptive filtering on signals containing both flaw and noise components (filter parameter $L_1=3$, $L_2=5$, $\mu_1=\mu_2=0.1$).

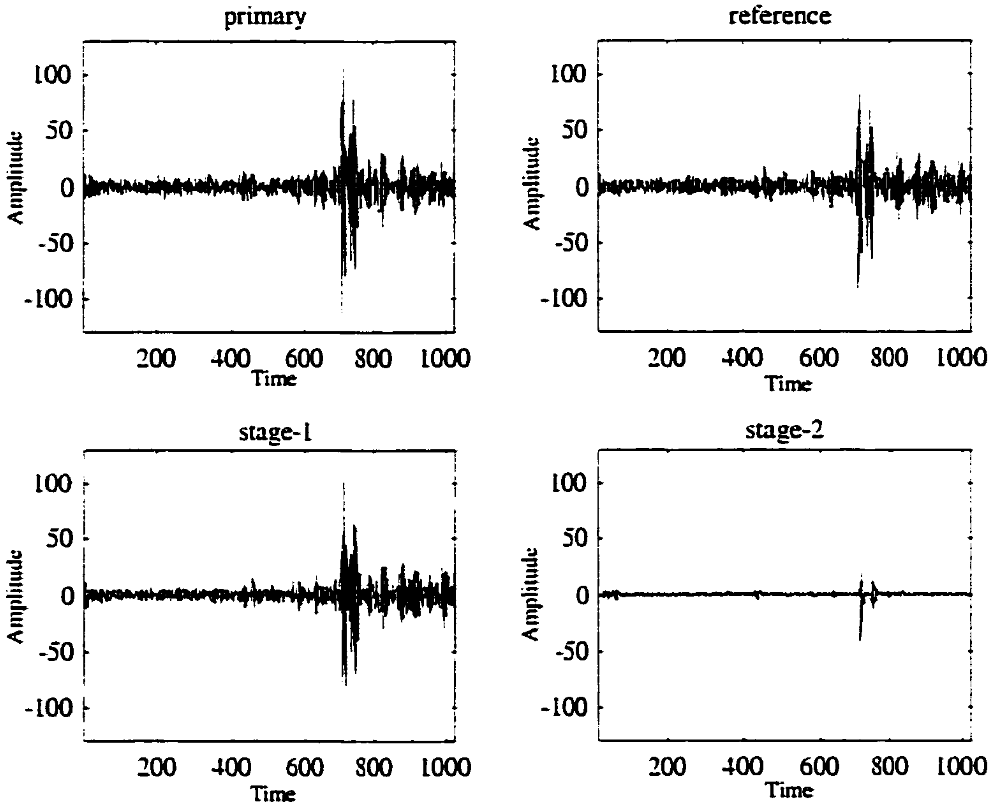

Figure 3.8 Results using adaptive filtering on signals containing both flaw and noise components (filter parameter $L_1=L_2=7$, $\mu_1=\mu_2=0.1$).

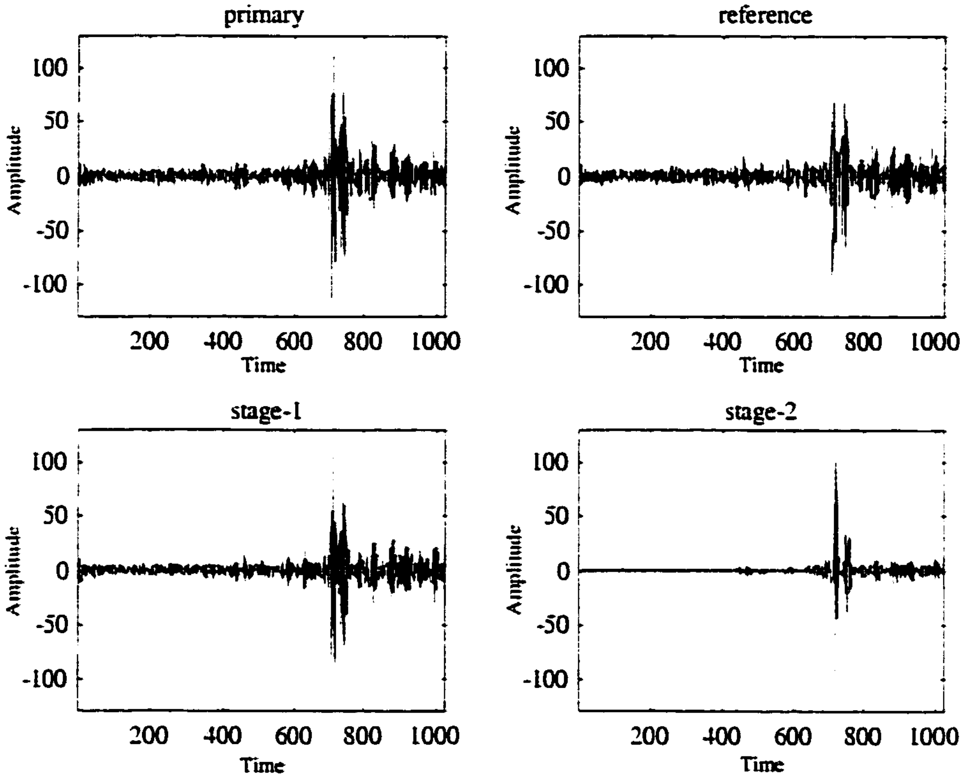

Figure 3.9 Results using adaptive filtering on signals containing both flaw and noise components (filter parameter $L_1=7$, $L_2=9$, $\mu_1=\mu_2=0.1$).

Table 3.4 SNR_{flaw} and cross-correlation coefficients in multi-stage adaptive noise cancellation.

Parameters		SNR_{flaw}(dB)			ρ	
L_1	L_2	Input	Stage-1	Stage-2	Stage-1	Stage-2
3	5	27.6502	28.1205	37.0675	0.8388	0.8919
7	7	27.6502	29.0110	41.1783	0.8388	0.9014
7	9	27.6502	29.0110	42.9493	0.8388	0.9014

Note: ρ represents the correlation between adjacent flaw signals at the end of stage1 and stage 2.

the second stage output signal. The second stage SNR columns show a significant jump in the noise reduction and the last columns also show increases in the correlation between the flaw signals. Similarly, the results obtained using noise only signals in Figure 3.10 show significant reduction in noise level. The cross-correlation coefficient in this case for grain noise components was reduced from 0.6534 in first stage to 0.4665 at the end of the second stage.

3.3.3 Effect of Learning Rate

In general, the time complexity of the ANC system depends on the learning rate μ of the LMSE algorithm. Variable learning rates were applied to the MAF system. Using L_1=7 and L_2=9, which was shown to be optimal in the previous experiment, convergence rates μ=0.01, 0.05, and 0.1 were tried. The results are summarized in Table 3.5. Once again, this parameter has a greater influence on the performance only in the second stage.

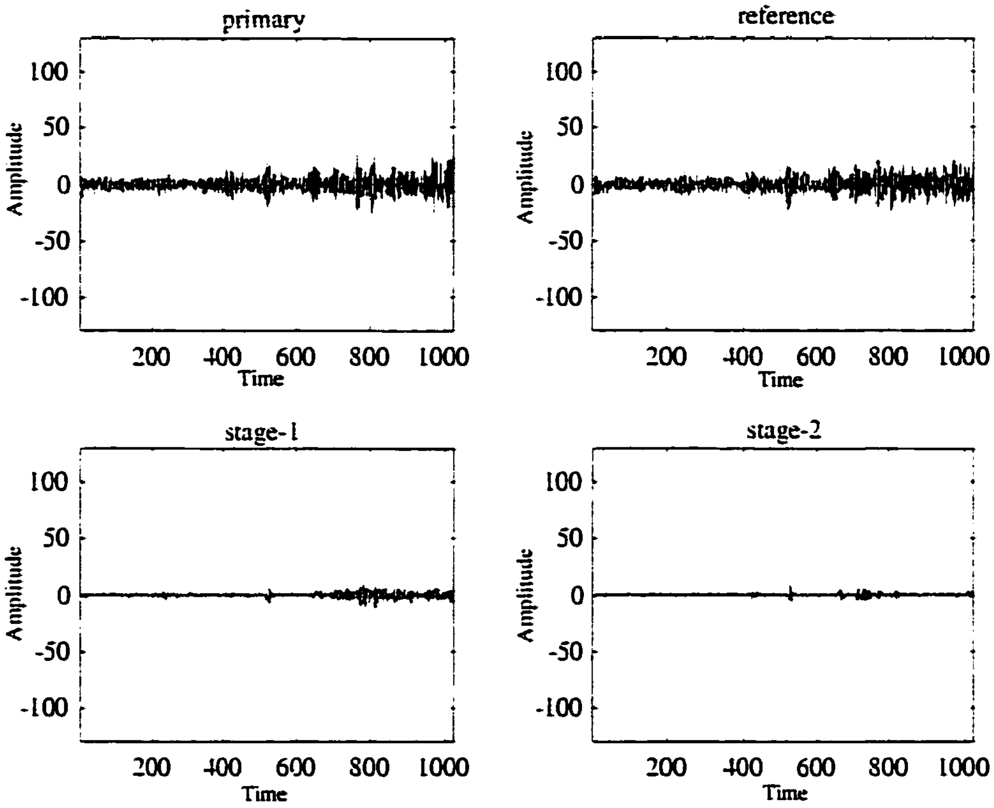

Figure 3.10 Results using adaptive filtering on noise-only signals (filter parameter L_1=7, L_2=9, $\mu_1=\mu_2$=0.1).

Table 3.5 SNR_{flaw} and cross-correlation coefficients in multi-stage adaptive noise cancellation (L_1=7, L_2=9 and μ_i is learning rate at each stage where i=1,2).

Parameters		SNR_{flaw}(dB)			ρ	
μ_1	μ_2	Input	Stage-1	Stage-2	Stage-1	Stage-2
0.01	0.01	27.6502	27.4270	25.8304	0.8388	0.7379
0.05	0.05	27.6502	29.1195	38.9023	0.8388	0.8511
0.1	0.1	27.6502	29.0110	42.9493	0.8388	0.9014
0.05	0.1	27.6502	29.1195	45.4681	0.8388	0.8511

Note: ρ represents the correlation between adjacent flaw signals at the end of stage1 and stage 2.

3.3.4 Effect of Transducer Distance

The degree of correlation associated with the noise components is highly dependent on the distance δ between the transducer positions from which the reference and input signals are acquired. Too small a value of δ will result in higher correlation between noises, whereas too large a value of δ will make flaw signals uncorrelated. The ANC system was implemented using FIR adaptive filters with varying values of δ, and the results are summarized in Table 3.6. The optimal SNR improvement was obtained when the distance was 0.016" (two pixels). As the distance between the two transducers is increased, the SNR of output at second stage is decreased. This shows that the value of δ should be chosen carefully for optimal performance of the MANC algorithm. This result can be further confirmed by examing the correlation of noise signals in the C-scan image. Both the normalized auto-correlation and cross-correlation parameters were estimated and are plotted in Figure 3.11 for two noise signals that are 2 pixels apart. This translates to a physical distance of 0.016". The cross– correlation function reveals that the grain noise signals are

Table 3.6 SNR_{flaw} comparisons for various distances between two transducers for multi-stage adaptive noise cancellation.

Distance (δ)	2	4	6	8
Input SNR	27.6502	27.6502	27.6502	27.6502
Stage-1 SNR	29.0110	28.4862	28.0523	30.1740
Stage-2 SNR	42.9496	38.8604	35.9458	30.8850

sufficiently uncorrelated to satisfy the assumptions. The auto-correlation property is also estimated to check its closeness to an impulse.

3.3.5 Method II Implementation

Adaptive noise cancellation was also implemented using the alternate configuration for multi-stage adaptive filtering process shown in Figure 3.3, where both the reference and primary inputs for second stage are obtained from the processed first stage data. Figure 3.12 describes a flow diagram for implementation of the second configuration. The filter parameters used here were $L_1=7$, $\mu_1=0.1$ in the first ANC system and $L_2=9$, $\mu_2=0.1$ in the second stage. The transducer distance δ was 2 pixels (0.016") in both ANC stages. As expected the improvement in performance in terms of the second stage output SNR is significantly higher. The SNR increased from 29.0110 dB in first stage to 47.8215 dB at the end of the second stage. Figure 3.13 shows the raw and processed A-scans using the second configuration. However, the disadvantage of this configuration is that the two stages have to be implemented sequentially. In contrast, the first configuration (Figure 3.2) can be implemented in an online manner.

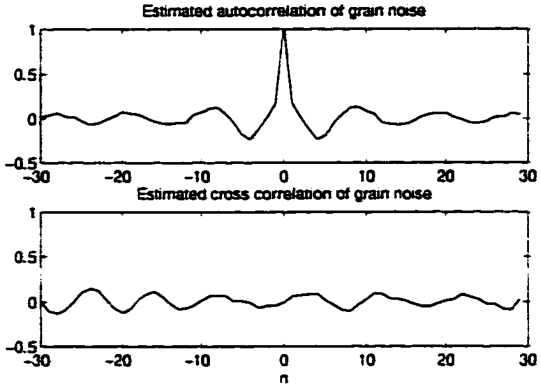

Figure 3.11 Normalized auto-correlation and cross-correlation.

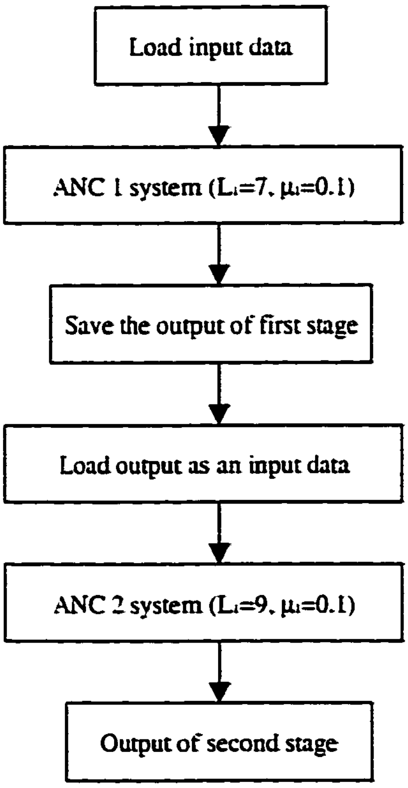

Figure 3.12 Flow diagram for Method II.

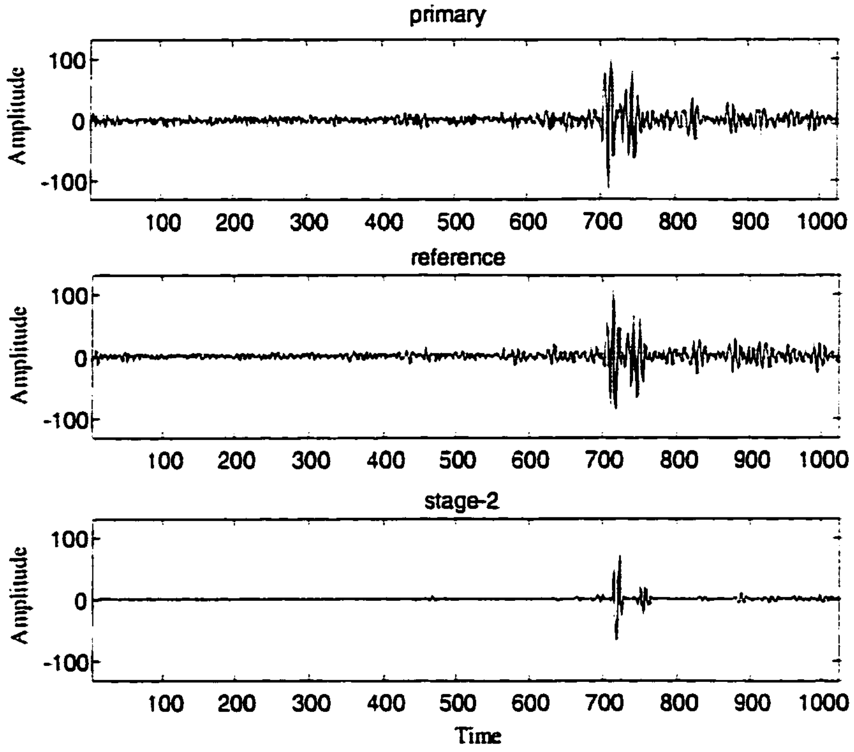

Figure 3.13 Results using Method II multi-stage adaptive filtering on signals containing both flaw and noise components (filter parameter $L_1=7$, $\mu_1=0.1$, $L_2=9$, $\mu_2=0.1$).

3.4 Adaptive Wavelet De-noising Method (AWDM)

Wavelet transform [42][43][44] is a recent analysis technique that is becoming increasing popular in many signal processing applications. The main characteristic of the wavelet transform is its multi-resolution decomposition of the information contained in a function or signal at different scales. In other words, wavelet analysis allows the use of longer time intervals where we want more precise low frequency information and shorter time intervals at high frequency information to get a good time resolution.

As shown in the time-frequency plane in Figure 3.14, the basis functions of wavelet transform are localized in both frequency (scale) and time, in contrast to Fourier basis functions that are localized only in frequency. This multi-scale or multi-resolution analysis (MRA) is based on the following properties. First, the spanned signal spaces are nested from the null space to the full space, which can be written as

$$\{0\} = V_{-\infty} \subset \cdots \subset V_{-2} \subset V_{-1} \subset V_0 \subset V_1 \subset V_2 \subset \cdots \subset V_{\infty} = L^2(\mathbf{R}). \qquad (3.17)$$

The above equation implies that V_1 consists exactly of all the functions in V_0 compressed by a factor of 2. V_2 consists of the functions in V_0 compressed by a factor of $2^2 = 4$. V_{-1} consists of the functions in V_0 dilated by a factor 2, and so on. For every pair of spaces $\{V_j, V_{j+1}\}$, we can define an orthogonal complement W_j from which the higher space can be recovered. This relation can be expressed as

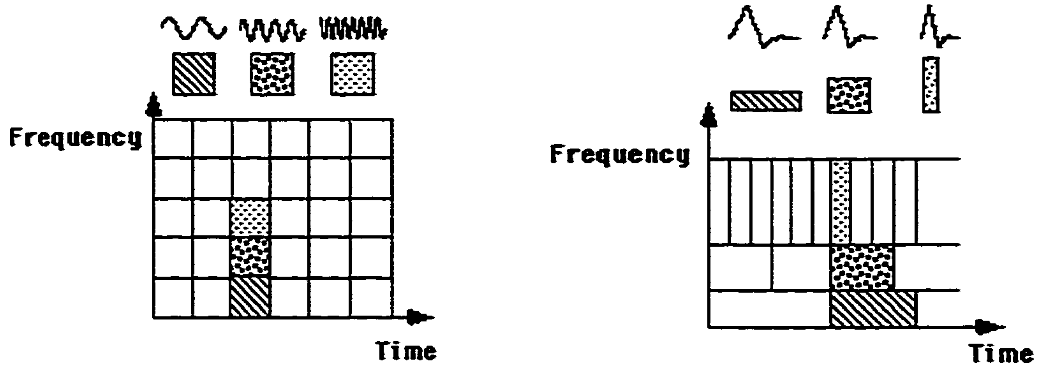

(a) (b)

Figure 3.14 Basis function resolutions in time-frequency plane, (a) windowed Fourier Transform, and (b) Wavelet Transform.

$$V_j \oplus W_j = V_{j+1}, \; j \in Z. \qquad (3.18)$$

The symbol '⊕' in Equation (3.18) implies that the vectors in W_j plus the vectors in V_j can generate all vectors in V_{j-1}. V_j and W_j are orthogonal. The basis for each nested subspace V_j are derived from a scaling function $\phi(t)$. This scaling function $\phi(t)$ and its translation $\varphi_k(t) = \phi(t-k)$ form an orthonormal basis for V_0 in Figure 3.15 and can be written as $V_0 = \underset{k}{span}\{\phi_k(t)\}$. Hence, any function $f(t) \in V_0$ can be expressed as $f(t) = \sum_k a_k \psi_k(t)$. A two dimensional family of functions is generated from the dyadic scaling function according to $\varphi_{j,k}(t) = 2^{j/2}\varphi(2^j(t-k))$ so that $V_j = \underset{k}{span}\{\varphi_{j,k}(t)\}$. The details in the signal reside in the subspaces W_j which are spanned by dilates and translates of the wavelet function $\psi_{j,k}(t)$. Furthermore, it is required that the scaling functions and wavelets be orthogonal.

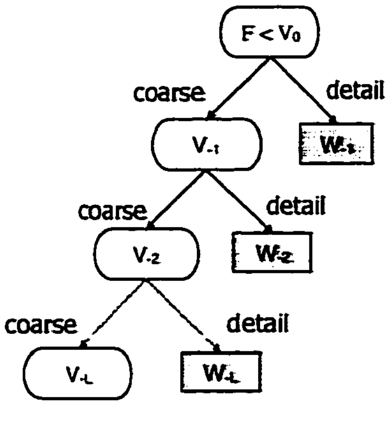

Figure 3.15 Decomposition using a multiresolution analysis.

The original wavelet shrinkage algorithm of Donoho and Johnstone [45][46][47] has found many applications in data de-noising. Noise cancellation using wavelet shrinkage is one possible approach for ultrasonic nondestructive evaluation. In this research, the wavelet shrinkage de-noising method can be treated as a preprocessing step for the multi-stage adaptive filter as shown in Figure 3.16. The main idea underlying wavelet shrinkage de-noising relies on wavelet coefficient thresholding. A standard model of noise in signals is additive Gaussian white noise that can be modeled as

$$y_i = f_i + z_i, \quad i = 0,1,\ldots,n-1. \tag{3.19}$$

where f_i are samples of f and z_i are independent and identically distributed (iid) N(0,1) random variables. For this model, Donoho and Johnstone showed in [45][47] that orthogonal wavelet transforms provide a powerful tool in recovering the original samples f_i by applying

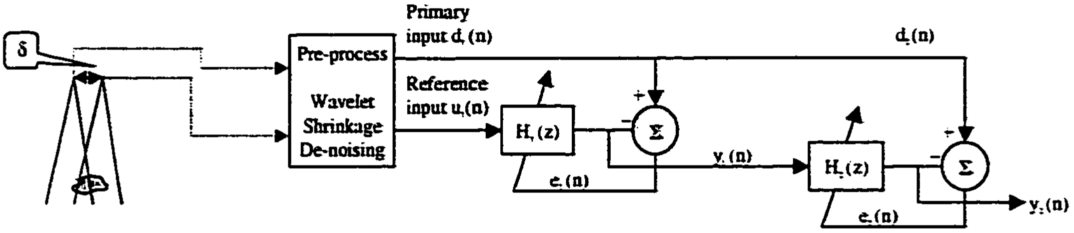

Figure 3.16 Configuration of adaptive multi-stage adaptive noise cancellation filter (AWDM).

a simple thresholding rule to the noisy wavelet coefficients. The wavelet shrinkage de-noising procedures can be summarized as follows:

1. Decomposition.

   Apply the discrete wavelet transform to a signal in Equation (3.19) and get the wavelet coefficients that can be defined as

$$WT(y_t) = WT(f_t) + WT(z_t) \tag{3.20}$$

   where WT stands for discrete wavelet transform, which is a linear operation. Hence, $WT(z_t) \overset{iid}{\sim} N(0,1)$ is also a Gaussian.

2. Threshold detail coefficients.

   The main part of wavelet based de-noising is thresholding, which simply assigns wavelet coefficients with amplitudes less than a certain threshold to zero. In order to choose the threshold value, it is defined by $\lambda = \sigma\sqrt{2\log n}$ where n is a signal length and σ^2 is the noise variance of the wavelet coefficients at the finest level [42][48][49].

In this research investigation, the level-independent estimates [50] of λ, i.e., one common estimate for all the multiresolution levels in the wavelet decomposition, is obtained by including all the detail coefficients.

The threshold calculation method involves selecting the threshold as a quantile of the empirical distribution of the wavelet coefficients. In order to perform the thresholding operation, a nonlinear soft thresholding operation [51] may be applied as

$$\hat{w}_t = \begin{cases} w_t - \lambda, & w_t \ge \lambda \\ 0 & |w_t| < \lambda \\ w_t + \lambda, & w_t < -\lambda \end{cases} \tag{3.21}$$

3. Reconstruction.

Using the inverse DWT, the thresholded wavelet coefficients are transformed back to obtain the filtered estimate of function, $\hat{f}_t$ of f_t.

3.4.1 Experimental Results with AWDM

An adaptive wavelet de-noising scheme was implemented in a wavelet transform domain using the coefficient shrinkage method. The block diagram (AWDM) for the multi-stage adaptive filtering process is shown in Figure 3.16, where both the reference and primary inputs for the first stage are preprocessed in wavelet transform domain. The scaling function and mother wavelet used in AWDM is a Daubechies wavelet [52] (in Figure 3.17)

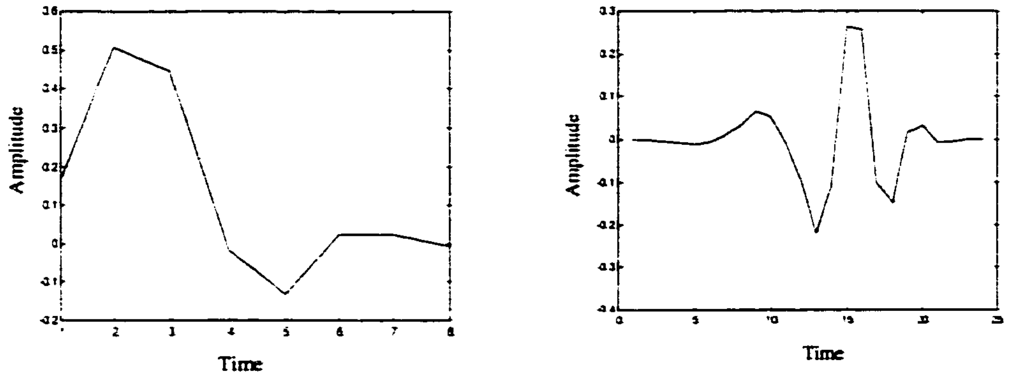

(a) (b)

Figure 3.17 Daubechies' wavelet (a) scaling function and (b) mother wavelet.

with decomposition level 3. The filter parameters used here were $L_1=7$, $\mu_1=0.1$ in the first stage and $L_2=9$, $\mu_2=0.1$ in the second stage. The transducer distance δ was 2 pixels (0.016") in the adaptive de-noising method. As expected, the improved performance in terms of the second stage output SNR is significantly higher since the primary and reference signals are prefiltered in the wavelet domain.

For comparison, the typical wavelet shrinkage de-noising method is applied to the primary and reference signals. As seen in Table 3.7, the SNR increased from 27.6502 dB in reference input signal to 38.97 dB at the end of the wavelet shrinkage de-noising step. The adaptive de-noising method also shows the improvement in terms of SNR with 78.4109 dB. Also, the wavelet shrinkage de-noising results are comparable to that obtained using the multi-stage adaptive noise cancellation method. In addition, the MANC if followed by the prefiltering process (WSD), results in a better performance. Figures 3.18 and 3.19 show results of the adaptive wavelet de-noising method.

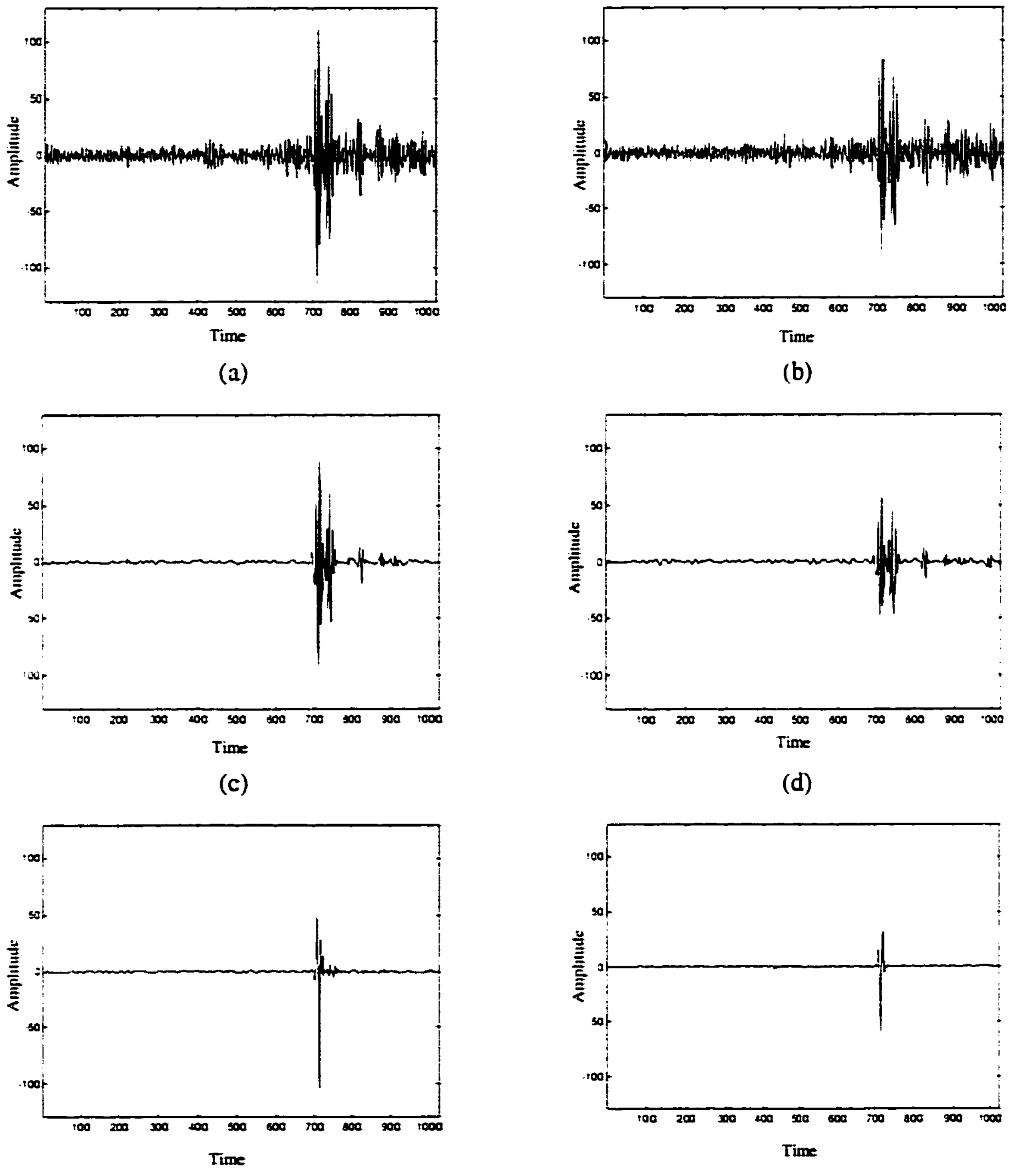

(a) (b) (c) (d) (e) (f)

Figure 3.18 Results using adaptive filtering on signals containing both flaw and noise components with wavelet shrinkage de-noising method (filter parameter $L_1=7$, $L_2=9$, $\mu_1=\mu_2=0.1$), (a) primary input, (b) reference input, (c) wavelet shrinkage de-noised signal with a primary input, (d) wavelet shrinkage de-noised signal with a reference input, (e) first stage output, and (f) second stage output.

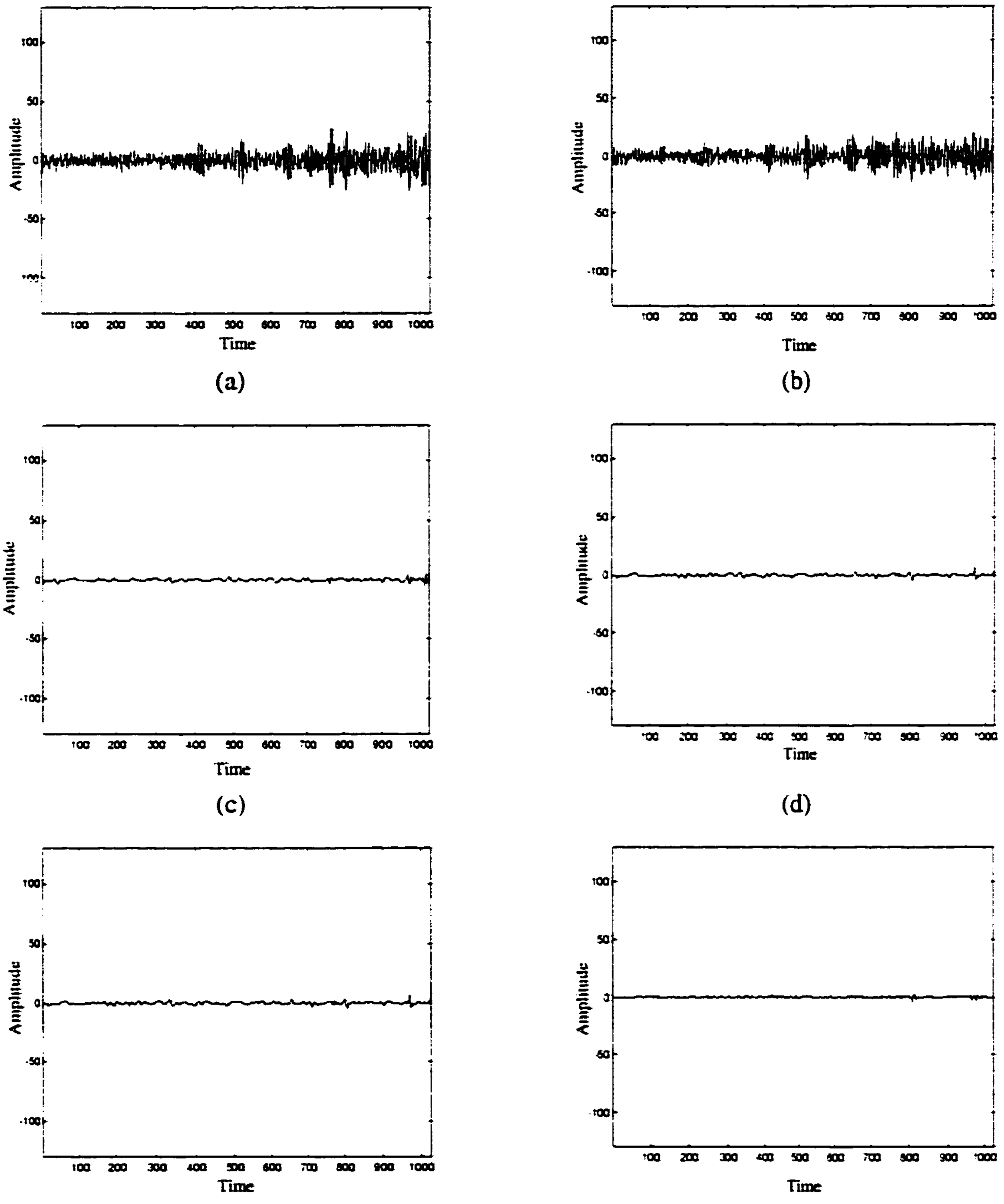

(a) (b) (c) (d) (e) (f)

Figure 3.19 Results using adaptive filtering on signals containing noise components only with wavelet shrinkage de-noising method (filter parameter $L_1=7$, $L_2=9$, $\mu_1=\mu_2=0.1$), (a) primary input, (b) reference input, (c) wavelet shrinkage de-noised signal with a primary input, (d) wavelet shrinkage de-noised signal with a reference input, (e) first stage output, and (f) second stage output.

3.4.2 Stopping Criterion

The stopping criterion is an important issue in multistage adaptive noise cancellation method. Since an iterative method computes successive signal-to-noise-ratio of a MANC system, a practical test is needed to determine the number of stages required before the algorithm is stopped. In this research, the stopping criterion, typically, is based on the SNR value. The following simple stopping criterion was implemented using a user–specified threshold value, θ.

1. Select a stopping threshold, θ.
2. Compute SNR_i at each stage i ($i=1,2,\ldots$).
3. If $R_{i,i+1} = \dfrac{SNR_i}{SNR_{i+1}} > \theta$, stop.

   Else go to the next stage.

The stopping threshold value (θ) used in this algorithm is 1.5. The above stopping criterion was applied to the multistage adaptive noise cancellation method. The SNRs are summarized in Table 3.8. For example, the ratio between the output of stage-1 and the

Table 3.7 SNR_{flaw} comparisons for a reference signal with wavelet shrinkage de-noising (WSD) method, multistage adaptive noise cancellation method (MANC), and adaptive wavelet de-noising method (AWDM) ($L_1=7$, $L_2=9$ and $\mu_1=\mu_2=0.1$).

	INPUT SNR	WSD	MANC*	AWDM*
SNR_{flaw}	27.6502	38.97	42.9493	78.4109

Note: * represents the second stage.

output of stage-2, $R_{1,2}$, is 0.70. Based on the above stopping criterion, the MANC system stopped after 3 stages with the SNR ratio value $R_{3,4} = 0.68$. Consequently, the algorithm was also stopped after 3 stages. Figure 3.20 shows the best filtered signal with M=3.

Table 3.8 Stopping criterion comparisons for the multistage adaptive noise cancellation method (MANC), ($L_1= L_2= L_3= L_4=7$ and $\mu_1=\mu_2=\mu_3=\mu_4=0.1$).

	Reference	Stage-1	Stage-2	Stage-3	Stage-4
SNR_i	30.3036	29.0505	41.1190	60.4678	18.2204

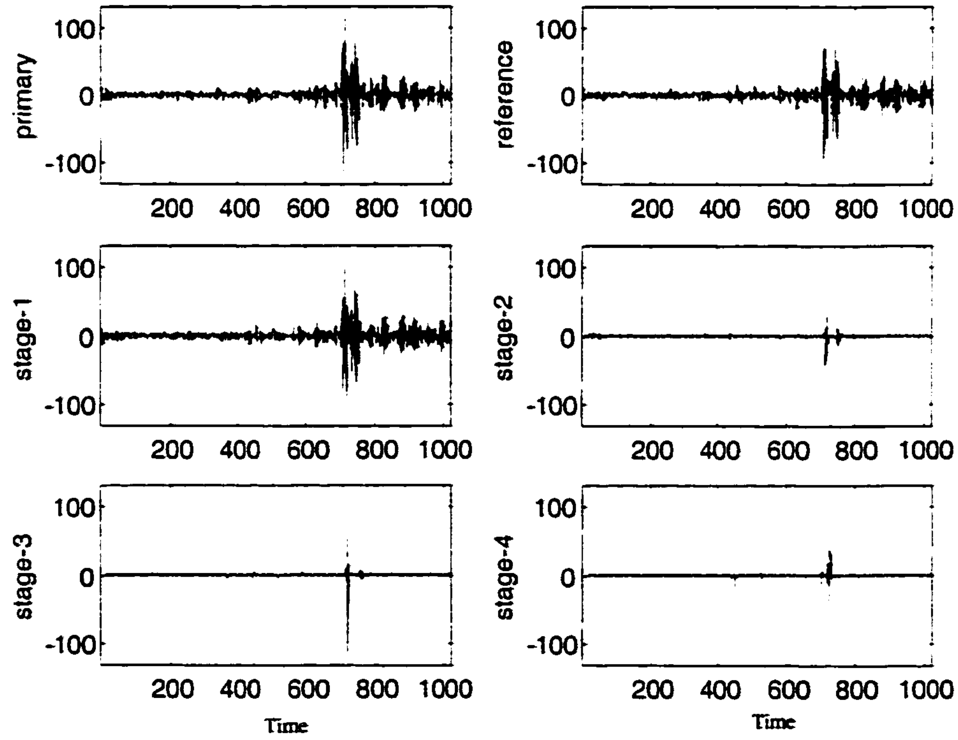

Figure 3.20 Results using MANC on signals containing both flaw and noise components with M=4 stages, (filter parameter $L_1= L_2= L_3= L_4=7$ and $\mu_1=\mu_2=\mu_3=\mu_4=0.1$).

CHAPTER 4. SIGNAL CLASSIFICATION – ONE DIMENSIONAL SIGNAL PROCESSING

A second focus of this thesis is the classification of ultrasonic signals obtained in the inspection of welds. Automatic signal classification (ASC) systems are becoming increasingly popular in commercial signal analysis applications. The major steps in an ASC system consist of (i) preprocessing, (ii) feature extraction, and (iii) classification. A number of methods have been developed over the years for extracting signal features from time, frequency, and spatial domains [53][54][55]. In signal classification systems, feature extraction serves to reduce the data length and identify discriminatory properties in signals of different classes. Through selection of the most effective features, the dimensionality of the measurement vector can also be reduced, which in turn can speed up the subsequent classification process. The most commonly used features consist of the Fourier series coefficients. Frequency analysis yields a representation of the frequency content and distribution of a signal. The Fourier transform maps a signal in the time domain into the frequency domain using complex exponential basis functions. The analysis equation of the Fourier transform is given by,

$$X(f) = \int_{-\infty}^{\infty} x(t) e^{-j2\pi f t} dt \tag{4.1}$$

The power of the Fourier transform lies in its capacity to decompose a signal into its constituent frequencies. Since the integral extends over all time, there is a loss of time information in the spectra. The exponential basis functions used in the Fourier transform are infinite in duration. This leads to spreading of any time localization of abrupt changes in the signal over the entire frequency axis. Therefore, any time localization of the input signal is lost when the magnitude spectrum is used.

A classic example is the Fourier transform of an impulse signal. In the time-domain, the dirac-delta is localized, but the magnitude spectrum of the delta function is spread out over the entire frequency spectrum (Figure 4.1). The magnitude spectrum of the Fourier transform does not have any information regarding the time of occurrence of the delta function. In ultrasonic nondestructive evaluation, signals contain reflections from discontinuities that manifest as abrupt time-localized changes, resulting in time-varying spectral characteristics. In fact, Fourier transform analysis is not appropriate for representing non-stationary signals.

A good way of circumventing this drawback of Fourier analysis is to introduce a window in the time domain. By sectioning parts of the signal and computing the Fourier transforms of these windowed signals, a measure of time can be introduced in the Fourier

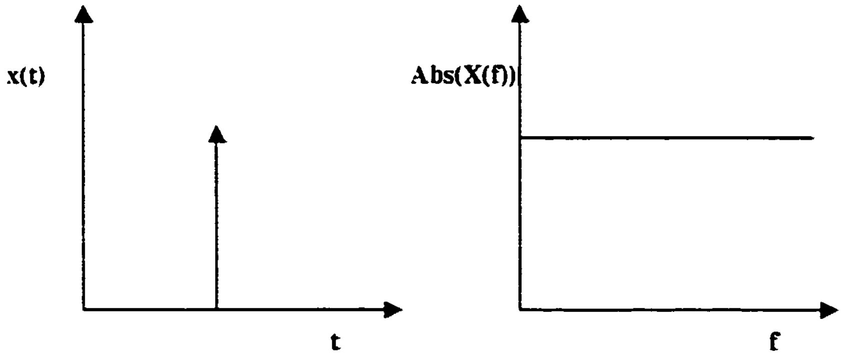

Figure 4.1 The dirac-delta and its Fourier magnitude spectrum.

analysis. This is the concept of the Short-Time Fourier Transform (STFT) [56], which is one of the early methods used in time-frequency analysis.

STFT uses a single window to compute the time-frequency spectrum of a signal. The input signal is first windowed in the time domain. The Fourier transform of the windowed sections of a signal constitutes its STFT. Several windows such as the rectangular window and the exponential window have been proposed depending on the problem at hand. The STFT $S(t,\Omega)$ can be defined by the relation,

$$S(t,\Omega) = \int_{-\infty}^{\infty} x(\tau) g^*(\tau - t) e^{-j\Omega\tau} d\tau \tag{4.2}$$

where $g(\tau)$ is the window function.

For a discrete time signal, the STFT is defined as

$$S(n,\omega) = \sum_{m=-\infty}^{\infty} x[m] g[n-m] e^{-j\omega m} \tag{4.3}$$

The STFT represents the local behavior of the signal x[n] as observed through the sliding window g[n-m]. The STFT analysis can be thought of as a filtering operation on the signal using a modulated filter bank. The analysis window, g[n], represents the filter and the exponential basis functions modulate this filter to obtain a modulated filter bank. On a time-frequency plane the STFT amounts to sampling the signal uniformly on both the time and frequency axes. The time-bandwidth product of the window used corresponds to the areas shown in Figure 4.2. The time-bandwidth product has a lower bound provided by the "Heisenberg uncertainty principle". This means that

$$(\textit{time resoultion}) \times (\textit{frequency resolution}) = \Delta t \Delta f \geq \frac{1}{4\pi} \qquad (4.4)$$

The major disadvantage of the STFT is the trade-off in time-frequency resolution. Since the time-frequency resolution remains the same for all frequencies in Figure 4.2, a signal can be studied with either high time or frequency resolution but not both. If the time-resolution is desired, then the window chosen is narrow. This results in a very poor frequency resolution and vice-versa. This property makes STFT analysis critically dependent on the window size and is not suitable for analysis of non-stationary signals, such as ultrasonic or biological signals. In the case of such signals, a sharper time resolution with a smoother frequency resolution window is needed for higher frequency components, and vice-

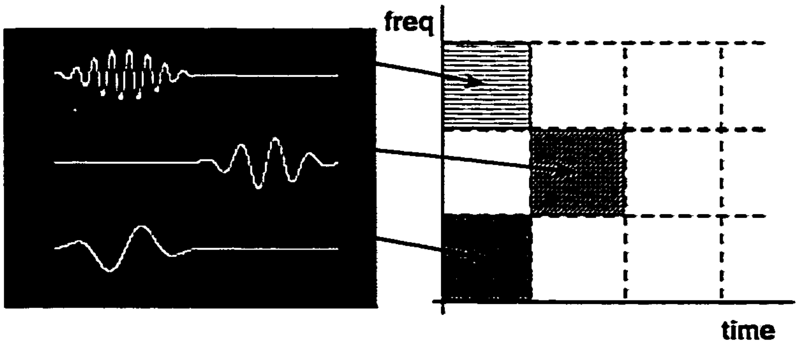

Figure 4.2 Time-frequency plane of the STFT.

versa. Recently, a more effective technique based on wavelet transforms has been developed for analyzing ultrasonic waveforms with good time-frequency resolutions.

4.1 The Discrete Wavelet Transform (DWT)

Wavelet Transform (WT) techniques are finding increasing use in many applications including image compression [57], signal processing [58][59], and solution of partial differential equations [60] with time-varying spectra. The WT is defined in terms of basis functions obtained by compression/dilation and shifting of a 'mother wavelet'. Mathematically, the wavelet coefficients of a function $f(t)$ are given by

$$WT_f(t,a) = \int f(\tau)h^*_{a,t}(\tau)d\tau \tag{4.5}$$

where

$$h_{a,\tau} = \frac{1}{\sqrt{a}}h\left(\frac{t-\tau}{a}\right) \tag{4.6}$$

Equation (4.6) is the shifted and compressed version of the mother wavelet $h(t)$. The time-shift is τ and the frequency scale is a. The mother wavelet $h(t)$ can be considered as a bandpass function centered on the scale frequency and is translated in time to select the part of the signal to be analyzed. Inner products of signal $f(t)$ with translated and dilated versions of wavelet $h(t)$ in Equation (4.5) indicate the contribution of the wavelet to a signal. Hence, the wavelet transform represents the correlation between the signal *f(t)* and scaled versions of a prototype, the mother wavelet. The scaling of the prototype function involves contraction and dilation of the signal, and the translation involves shifting this function along the time axis.

Wavelet analysis allows the use of long time intervals where we want more precise low frequency information, and shorter regions where we want to analyze high frequency information. This is the biggest advantage of the wavelet representation in signal processing applications. Figure 4.3 shows the coverage of the time-frequency plane using the Fourier

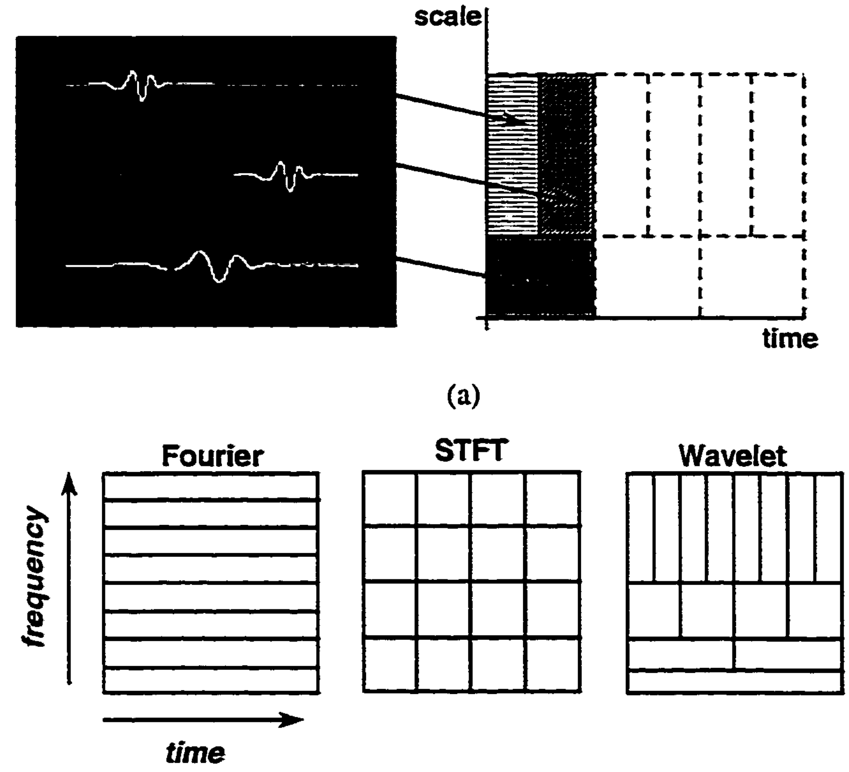

(a)

(b)

Figure 4.3 (a) Time-frequency plane of the WT and (b) comparisons of FT, STFT, and WT.

transform, STFT, and wavelet representation. As shown in Figure 4.3, the wavelet transform also performs multi-resolution analysis of signals using varying window sizes.

It is convenient to view the decomposition as passing a signal s[n] through a pair of filters h[n] and g[n]. The pair of filters h[n] and g[n] corresponds to the half-band lowpass and highpass filter, respectively, and are called the quadrature mirror filters (QMF) in the signal processing literature [61]. By downsampling the filtered signal by two (i.e., dropping every other sample) as shown in Figure 4.4, the wavelet transform is computed by filtering the signal with a set of filters (h[n] and g[n]) and subsampling the output of each filter in order to sample the multi-resolution signals at their respective Nyquist frequencies. The signal s[n] is first passed through a halfband highpass filter g[n] and a lowpass filter h[n]. After filtering, half of the samples of the two output signals are discarded by downsampling since the signals now have a bandwidth of π/2 radians instead of π. The output of each of the filters after subsampling by 2 is expressed as

$$y_{high}[k] = \sum_{n} s[n]g[2k-n] \tag{4.7}$$

$$y_{low}[k] = \sum_{n} s[n]h[2k-n]. \tag{4.8}$$

The relationship of h[n] and g[n] can be written as

$$h[L-1-n] = (-1)^n g[n] \tag{4.9}$$

where L is the length of the filter.

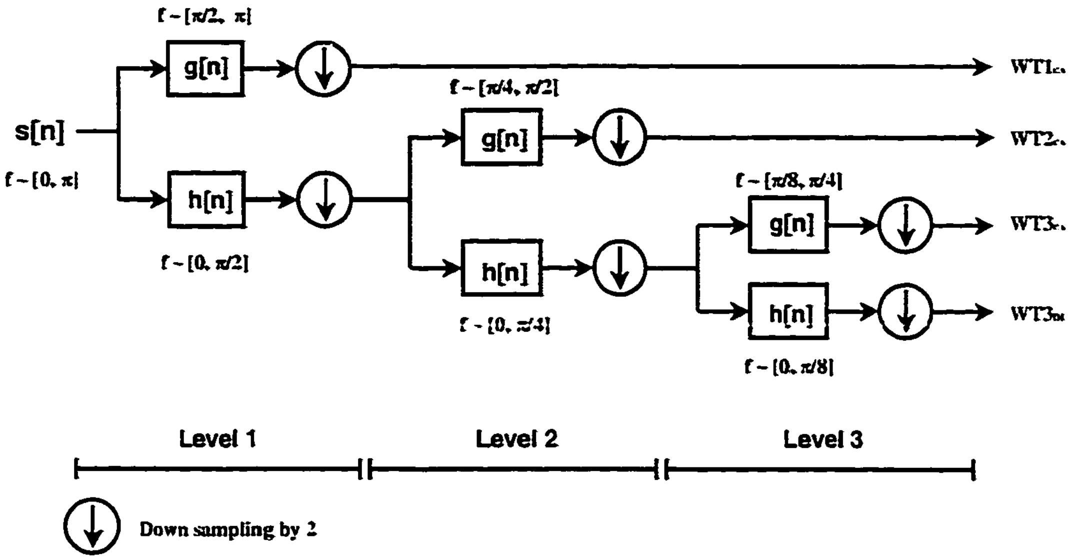

Figure 4.4 The wavelet decomposition tree.

Recursive filtering using this filter bank produces the wavelet coefficients at the output of the highpass filters and the detail signal at the output of the final lowpass filter. For level 3 wavelet decomposition (Figure 4.4), the DWT coefficients are concatenated at every level and can be expressed as

$$C_{DWT} = \left[WT3_{DI} \quad WT3_{CA} \quad WT2_{CA} \quad WT1_{CA} \right] \tag{4.10}$$

where DI and CA stand for detail information and coarse approximation, respectively. Figure 4.5-(a) shows an ultrasonic crack signal using a 5 MHz transducer at a 60 degree angle and 25 MHz sampling frequency. The signal length is 512 points, and its DWT coefficients using Daubechies wavelet [62][63] of order 4 (Figure 4.6) is shown in Figure 4.5-(b). In general, there are no deterministic criteria to chose the mother wavelet. The selection of wavelet depends on data distribution, signal shape and wavelet properties

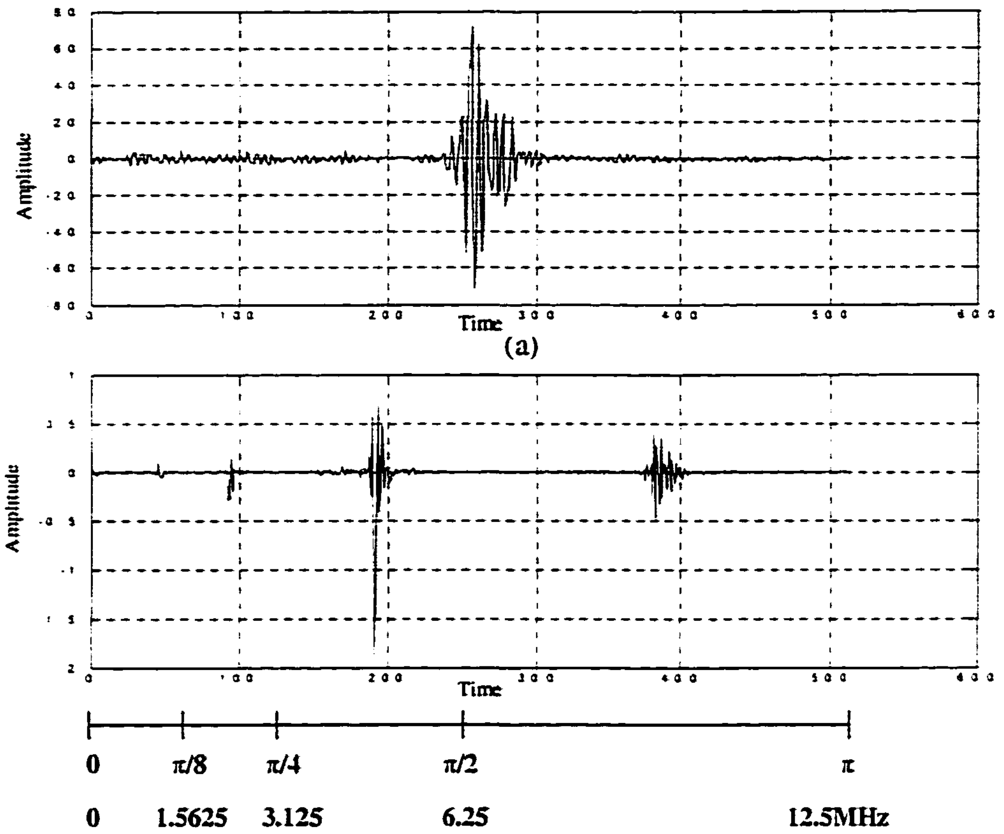

(a)

(b)

Figure 4.5 The relation of frequencies in WT domain.

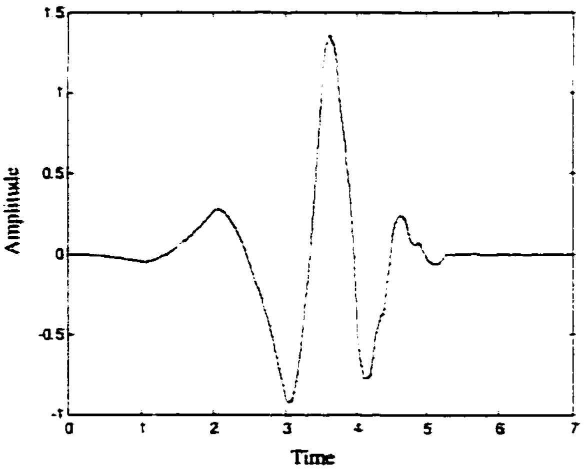

Figure 4.6 The Daubechies wavelet with order 4.

such as symmetric property or orthogonality. Therefore, in this research investigation, Daubechies wavelet is chosen as a mother wavelet since the signal shape is asymmetric and Gaussian type. As can be seen in Figure 4.5, it is convenient to analyze the relation of each frequency band in wavelet transform domain. The main energy of the signal appears in [$\pi/8$, $\pi/2$], which corresponds to the frequency range of 1.5625 MHz to 6.25 MHz.

4.2 Feature Selection

The objective of feature selection is to find the minimum number of features with maximum discriminatory information. A number of feature selection algorithms in pattern recognition have been developed and applied to automated signal classification applications. The techniques for feature extraction can be categorized into automated and manual techniques. Examples of automated feature selection techniques are the ID3 decision tree [64] or cost optimization techniques. Typically, cost optimization functions are based on Entropy [65] of the data or the fisher linear discriminant (FLD) function [66].

In the manual feature selection case, the feature vector is selected from the significant DWT coefficients. In Figure 4.5, the energy of the ultrasonic signal is seen to be concentrated in certain frequency bands and in general, coefficients in selected frequency bands can be a good candidate for a feature vector. A number of supervised and unsupervised pattern recognition algorithms have been applied for the classification of multidimensional signals. The K-means clustering algorithm [67] was one of the most widely used techniques for partitioning feature space. More recently, neural networks [68] have proved to be extremely effective in signal classification, largely due to their ability to generate arbitrarily complex decision boundaries.

In this research, the multiplayer perceptron (MLP) was trained with back propagation learning algorithm to classify the signals [69][70]. The simplest model of the perceptron network is the single layer perceptron, which consists of one input layer and one output layer. Since the capabilities of a single layer perceptron are limited to linear decision boundaries, this network is limited in real world applications. However, by cascading perceptrons in layers, we can implement complex decision surfaces. For example, Figure 4.7 illustrates the architecture of the two-hidden layer MLP network.

In MLP network architecture, an activation level is computed as shown in Figure 4.8. The MLP networks consist of a set of simple nonlinear processing elements that are arranged in layers and connected via weights. The nonlinear sigmoid function is bounded in [0,1] and is expressed as

$$f(\theta) = \frac{1}{1+e^{-\lambda\theta}} \tag{4.11}$$

where the parameter λ determines the slope of sigmoid function. The input vector $\mathbf{I} = (I_1, I_2, \ldots, I_N)$ is fed to the input layer of the network. In order to compute the values at the hidden and output layer nodes, the formulations can be written as

$$H1_j = f\left(\sum_{i=1}^{N} u_{ij} I_j\right), \quad j=1,2,\ldots,N_1 \tag{4.12}$$

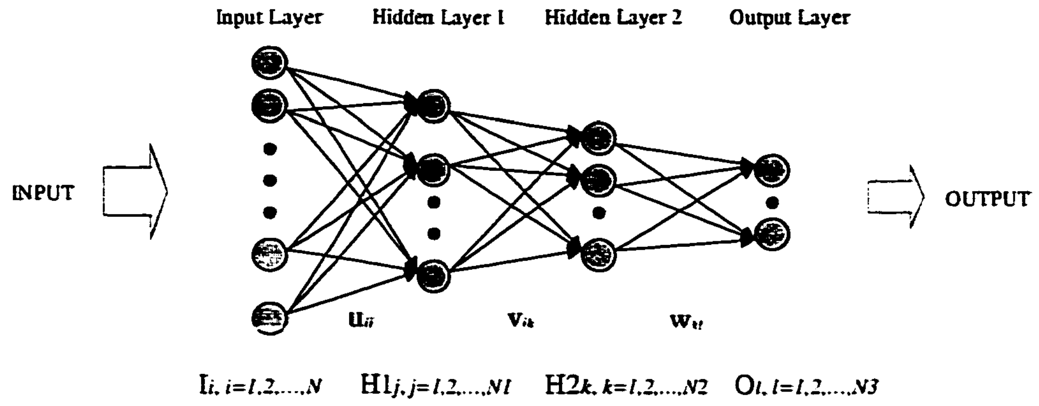

Figure 4.7 The multiplayer perceptron architecture with two hidden layers.

$$H2_k = f\left(\sum_{j=1}^{N1} v_{jk} H1_j\right), \quad k=1,2,\ldots,N_2 \tag{4.13}$$

$$O_l = f\left(\sum_{k=1}^{N2} w_{kl} H2_k\right), \quad l=1,2,\ldots,N_3 \tag{4.14}$$

The training of a multiplayer perceptron is usually done by using the back-propagation learning algorithm, a gradient–based iterative algorithm in the learning error that is propagated backwards through the network. Accordingly, the weight update equation in the back-propagation algorithm is given by

$$w_{ji}^k(n+1) = w_{ji}^k(n) + \eta\delta_j^k(n)x_j^{k-1}(n) \tag{4.15}$$

where η is a learning rate parameter, $\delta_j^k(n)$ is the local gradient for node j in layer k, and $x_j^{k-1}(n)$ is the output of node j in layer $k-1$ at the time instant n.

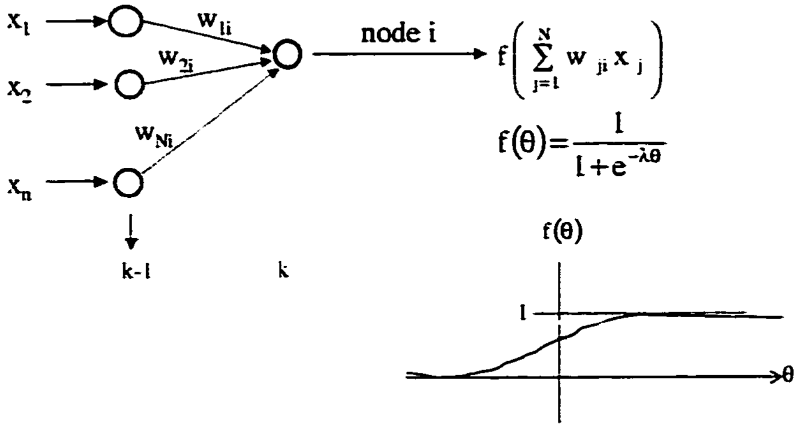

Figure 4.8 An example of nonlinear processing.

4.3 Application to Weld Inspection Data

Test welds were fabricated with induced discontinuities. The welded test plates were 24 x 24 x 1 ½ - inch thick HY-80 steel. A gas metal arc welding (GMAW) process was used to fabricate the plates. The following types of defects were induced in these test welds: porosity, slag, lack of fusion, and crack. Figure 4.9 shows a general scanning procedure and a geometry for a test plate. The transducer was moved along the longitudinal axis of the weld. In order to ensure coverage of the defect area, the test sample plate was scanned from either sides of the weld, referred to as north and south views.

A database comprising C-scan images using an automated scanning system was generated using a 5 MHz transducer, 60 degree angle beam, and a sampling frequency of 25 MHz. Figure 4.10 shows typical C-scan images from each class. The horizontal and vertical axes correspond to the axial and circumferential positions of the transducer on the sample plate.

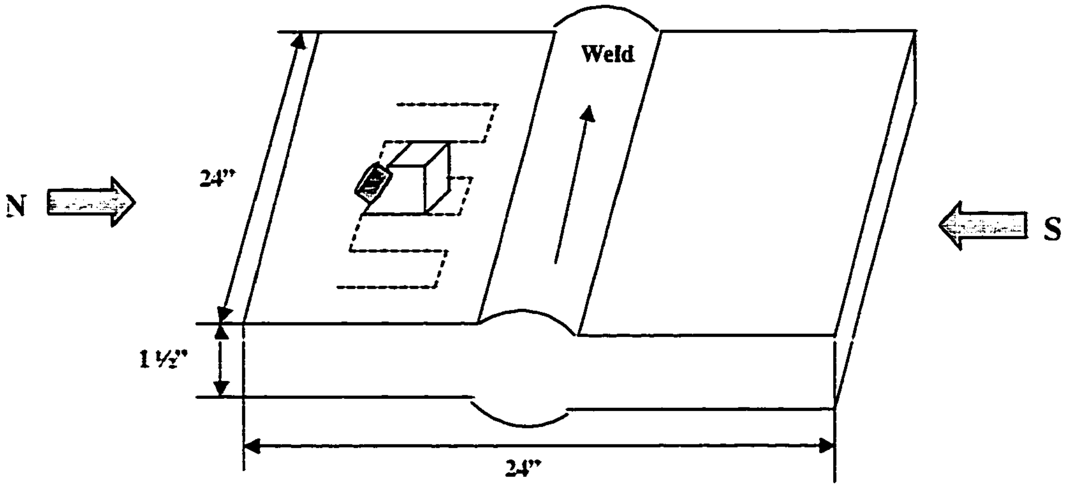

Figure 4.9 The scanning procedure and test plate geometry.

From the known positions of the machined discontinuities, the spatial coordinates and time gates of the A-scan were first computed. With a sampling frequency of 25 MHz, the sampling period T is 0.04 μs. Once the start and end time gates were identified, a signal of 512 samples [20 ~ 21 μs] was generated according to the procedure shown in Figure 4.10. The metal path with time of flight [20 ~ 21 μs] is [1.26 ~ 1.323"] with sound velocity 0.126 inch per microsecond. In practice, UT weld inspection signals contain multiple indications and in order to classify each indication, the time segment chosen is around 10 or 15 μs.

In order to keep the signal length constant at 512 points, a Gaussian weighting function centered at the peak helps de-emphasize other indications at the rear extremities of the gate. Therefore, the windowed signal $y_1[n]$ can be expressed as

$$y_1[n] = x[n]e^{-n/2\sigma^2} \qquad (4.16)$$

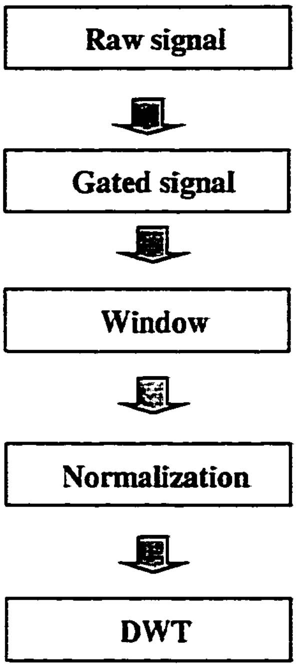

Figure 4.10 The overall implementation procedure for training database.

The value of σ, the shape of the Gaussian window, depends on time duration of the time window selected. After segmenting, the signal $y_1[n]$ is normalized to get $y_2[n]$ expressed as

$$y_2[n] = \frac{y_1[n]}{\max|y_1[n]|}. \tag{4.17}$$

The DWT coefficients for $y_2[n]$ are computed by Equation (4.5) and a feature vector consisting of DWT coefficients [81 ~ 220] is used as input to classify a neural network. The distribution of A-scan signals in four classes is summarized in Table 4.1. Two hundred signals (50 signals from each class) were randomly chosen to be included in the training dataset to train the network. The remaining signals in the entire dataset were used as test

Table 4.1 Distribution of A-scan signals in each defect.

	Crack	Porosity	Slag	Lack of fusion
Number of signals	155	52	132	379

data. Each windowed signal was first normalized, and the discrete wavelet transforms were computed. In a feature selection stage, the coefficients were chosen between 81 to 220 on DWT domain. The coefficients correspond to the frequency bands [1.9531 ~ 5.3711] MHz. The results observed at each step in Figure 4.10 are shown in Figure 4.11. The feature vectors consist of 140 DWT coefficients requiring 140 input nodes in the MLP network. The

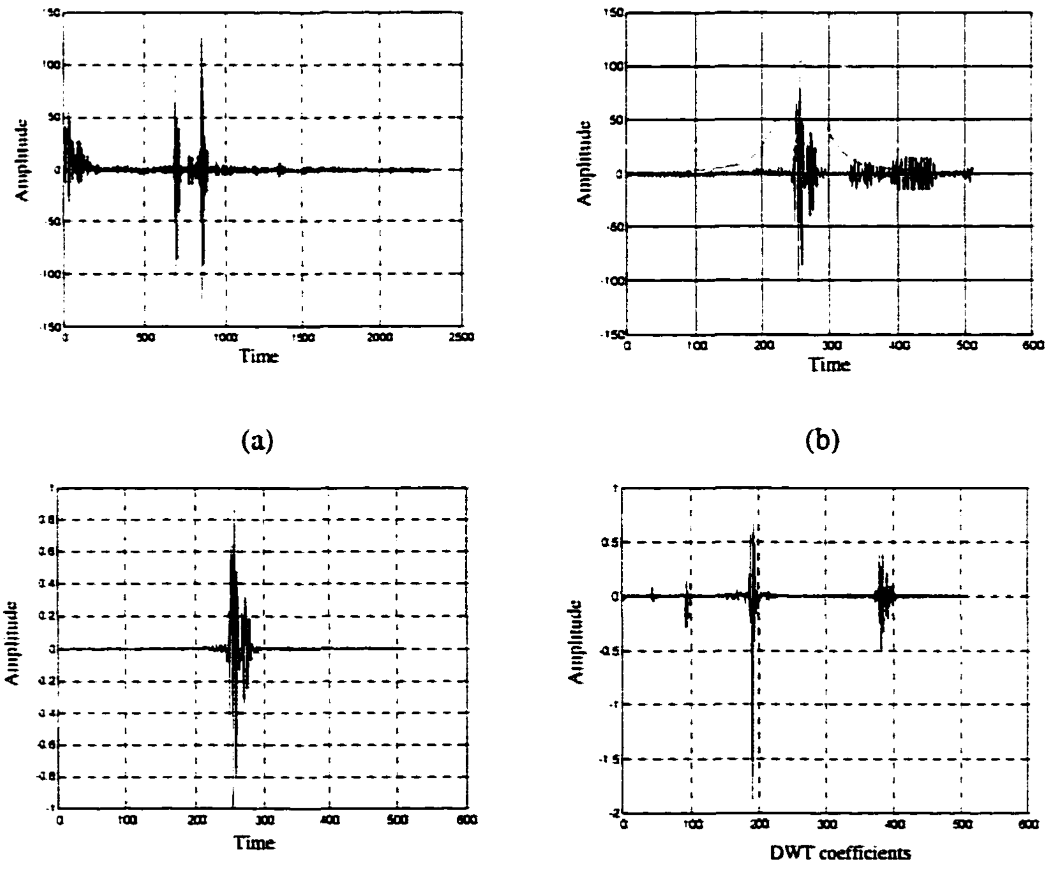

(a)

(b)

(c)

(d)

Figure 4.11 An example signal corresponding to each step of Figure 4.7, (a) raw signal, (b) gated signal and window function, (c) de-noised and normalized signal, and (d) DWT.

network also consisted of two hidden layers with 40 nodes in the first hidden layer, 12 nodes in the second hidden layer, and 4 nodes in the output layer corresponding to crack, slag, porosity, and lack of fusion.

The neural network was trained and the performance was tested on 28 C-scan images not used in training. While each A-scan from the image was preprocessed, the feature vector of DWT coefficients was computed and used for inputs to the neural network. In the neural network-generated pixel by pixel classification image, cracks are represented in red, lack of fusions are represented in green, slags are represented in cyan, porosity is represented in yellow, and background signals are shown in blue. A precise quantitative measure of the classification performance cannot be given for this database because only the class of regions is known rather than the class of every single A-scan. The classification of each A-scan in the ROI was noted, and the final classification of the ROI was based on the histogram of the classification image. Figure 4.12 shows a typical classification image and the corresponding

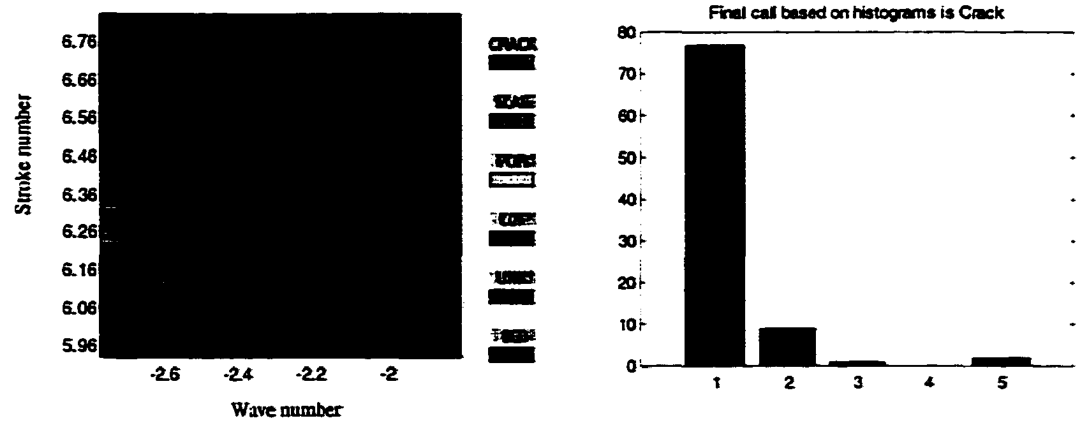

(a) (b)

Figure 4.12 (a) Classification image of ROI and (b) corresponding histogram (1-crack, 2-slag, 3-porosity, 4-lack of fusion, and 5-unknown).

histogram. The histogram shows the number of pixels in the ROI assigned to each of five classes: crack, slag, porosity, lack of fusion, and unknown. The "unknown" class indicates that the neural network could not classify the signal into any of the four classes unambiguously. Based on the histogram, the final classification of the ROI in this example (Figure 4.12) is "crack". Figure 4.13 and Figure 4.14 show the input C-scan image and neural network-generated classification images. Table 4.2 is summarized for C-scan classification results.

Table 4.2 Summary of classification results for individual C-scan using DWT coefficients.

	Crack	Slag	Porosity	Lack of Fusion	Total
Crack	7				7/7
Slag		7			7/7
Porosity	3	1	3		3/7
Lack of Fusion				7	7/7
					24/28

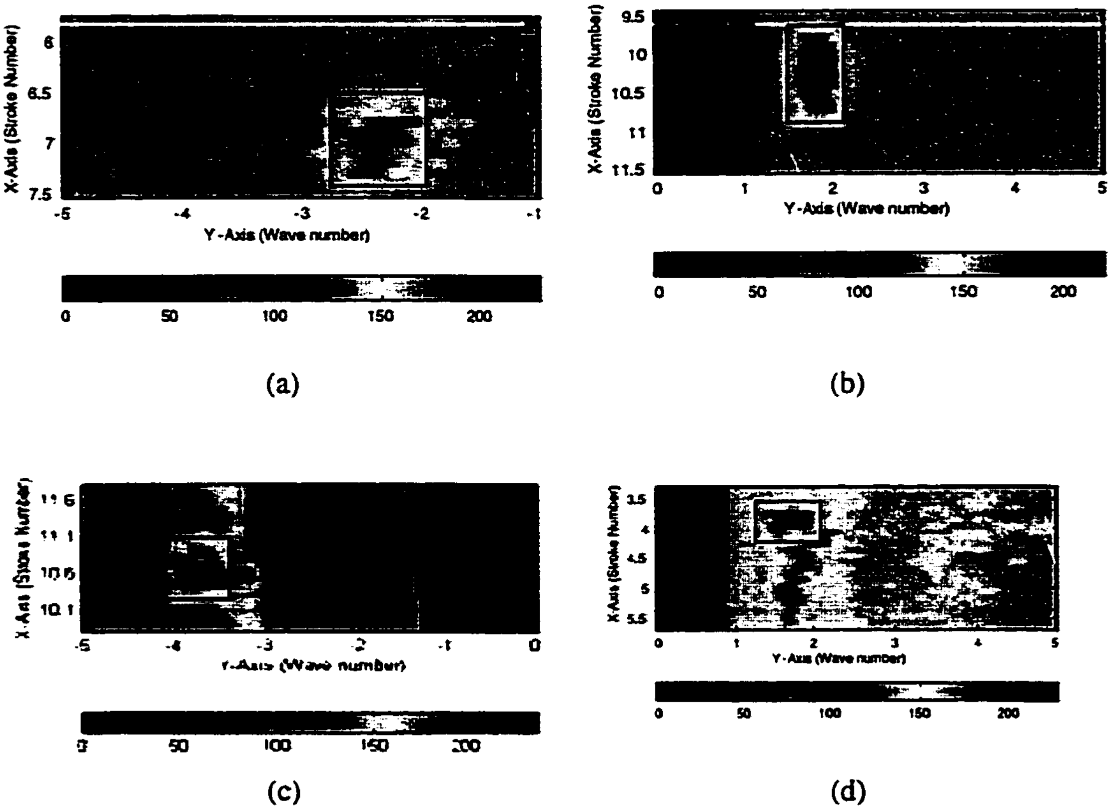

Figure 4.13 The typical C-scan image for (a) crack, (b) lack of fusion, (c) slag, and (d) porosity.

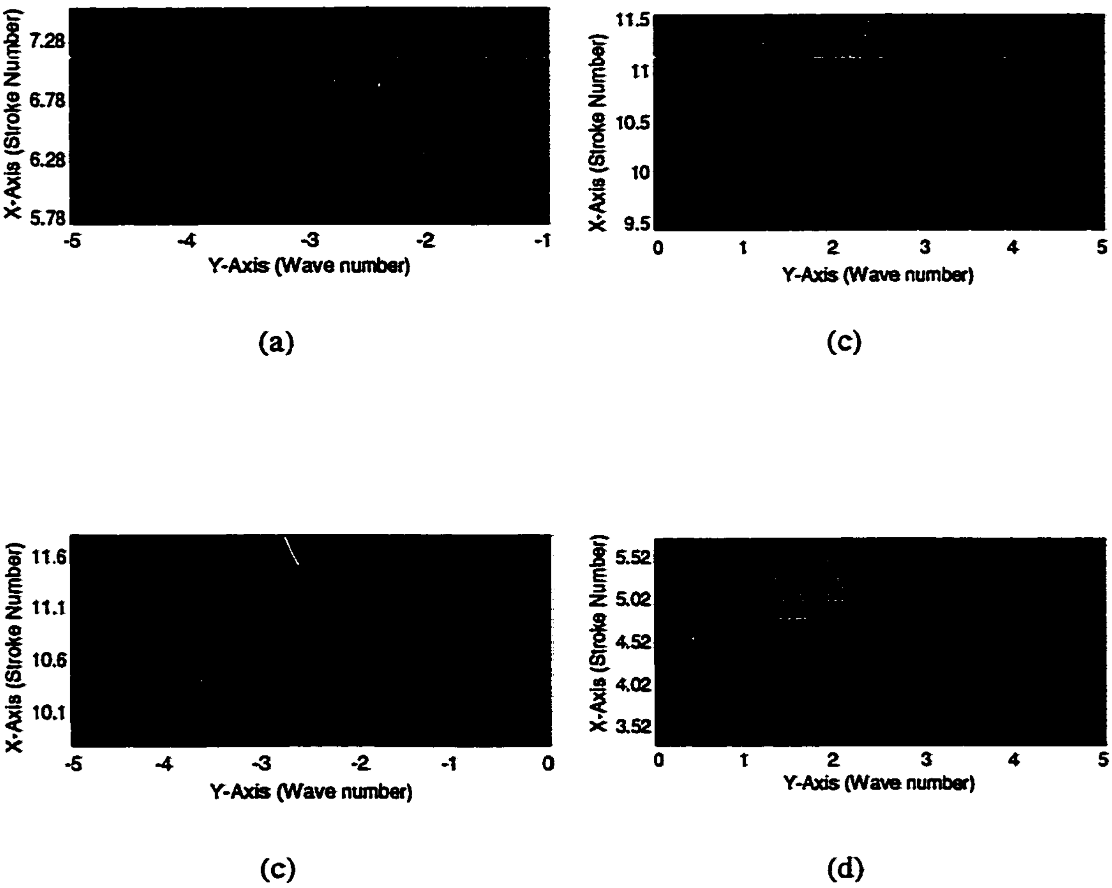

(a) (c)

(c) (d)

Figure 4.14 The neural network-generated classification images of Figure 4.13, (red = crack, green = lack of fusion, cyan = slag, yellow = porosity, purple = unknown, and blue = background).

CHAPTER 5. SIGNAL CLASSIFICATION – MULTIDIMENSIONAL SIGNAL PROCESSING

Ultrasonic signal classification systems currently used are based on processing individual A-scans. Even though these approaches show reasonable success, a single A-scan signal itself cannot represent a flaw in time, space, or transform domain. Another drawback of these approaches is that they do not incorporate the effect of beam spread. A better approach is to analyze a neighborhood of signals prior to making a classification decision. Such an approach provides a better estimate of the dynamics in the signal. In the previous chapter, a work on classification of a group of A-scans using discrete Wavelet transform (DWT) coefficients has been shown where the variance of a group of A-scans in a neighborhood is computed. Although computationally simple, this technique does not capture all the characteristics of the signal. In this research, a new classification scheme, based on classifying a set of B- and B'-scans, is presented to combine these results to obtain a final classification for a flaw.

A multidimensional signal can be modeled as a function of M independent variables where $M \geq 2$. In this chapter, we are concerned primarily with two- and three-dimensional discrete ultrasonic data. In ultrasonic inspection, a piezoelectric transducer is used to send high frequency sound (ultrasonic) wave into the test sample. Discontinuities in the sample reflect the energy that is received by the transducer and converted into an electrical signal that varies with time. The result is a one-dimensional time domain signal called an A-scan.

In the inspection of a weld, a two-dimensional scan of an area around a weld (Figure 5.1) is typically done by acquiring one A-scan at each spatial location, resulting in a three-

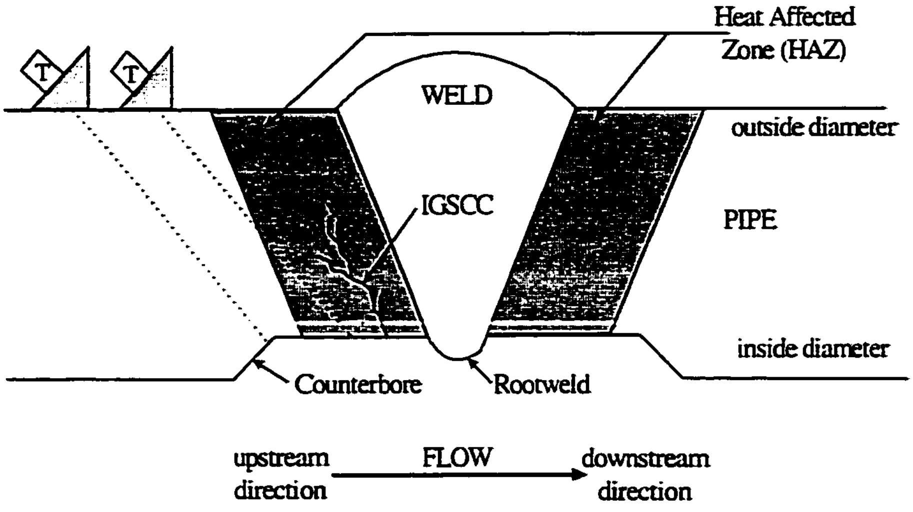

Figure 5.1 Inspection geometry for ultrasonic weld inspection.

dimensional done by acquiring one A-scan at each spatial location, resulting in a three-dimensional volume of data represented by $Z(x,y,t)$, where (x, y) represents the spatial coordinates of a transducer and t is the time axis. An image of the sample obtained by presenting the peak value of the A-scan at each position (x, y) is called the C-scan. A collection of A-scans along a single line of the C-scan image is referred to as the B-scan image. In weld inspection, the set of A-scans obtained by scanning perpendicular to the weld at $y=y_0$ is know as a B'-scan and can be represented as $Z(x,y_0,t)$, while that obtained by scanning parallel to the weld at $x=x_0$ is known as a B-scan represented by $Z(x_0,y,t)$. A C-scan image shows the plane view of the test specimen. Figure 5.2 shows an example of C-scan, B-scan and B'-scan image representations of weld inspection data. The B- and B'-scan images illustrate the changes in the A-scan as the transducer scans the flaw. The axes on these images represent time and distance (x or y). The B-(axial scan) and B'-scan (circumferential scan) represent a cross-sectional view of the object on a plane that is normal

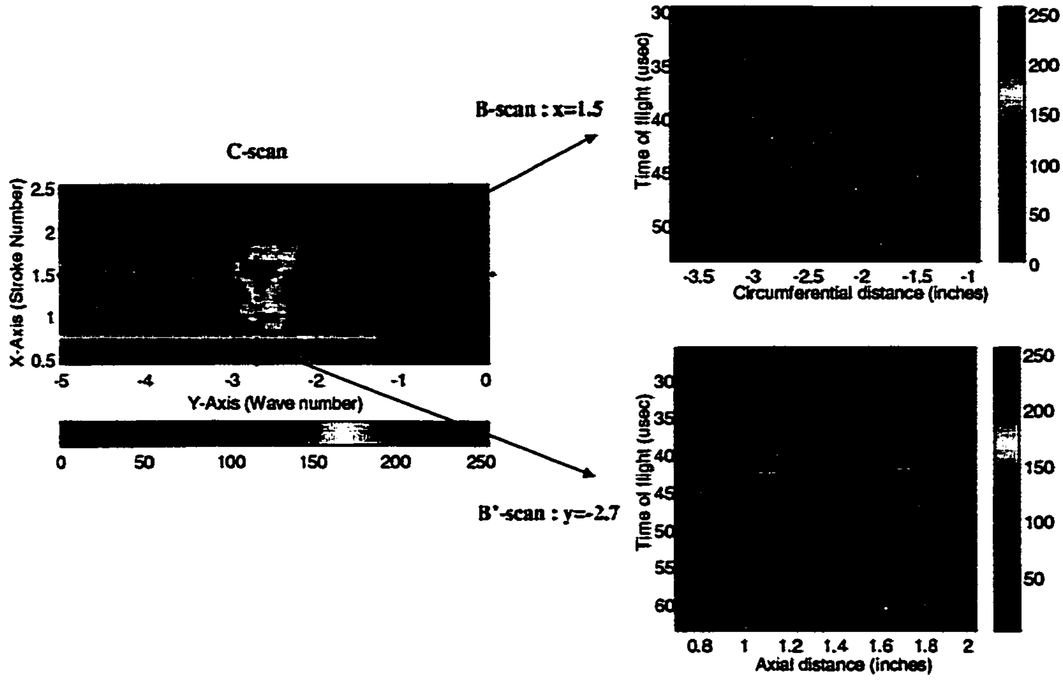

Figure 5.2 Typical C-scan, B-scan and B'-scan images.

to the surface of the probe. These images contain significant discriminatory information between different types of flaws. For instance, the reflection obtained from planar flaws (cracks) tends to have a sharper envelope transverse to the weld but a larger envelop along the weld, while those from volumetric flaws (slags and porosities) tend to have a larger envelope along both spatial directions. Further, the signals from planar flaws have different spatial variations from that of volumetric flaws. Thus, a classification scheme using information in the A-scans in a neighborhood is more powerful than previous schemes based on individual A-scans.

In order to analyze the information contained in a three-dimensional volume of data, this thesis investigates the feasibility of using two- and three-dimensional transform–based methods for feature extraction. Using the overall approach of feature extraction followed by classification of the feature vector, the problem is reduced to one of compressing the information into an appropriate feature vector. The next section describes the application of two-dimensional Fourier transforms to the B- and B'-scan image data.

5.1 Two-dimensional Fourier Transform

A simple feature extraction approach for images is the two-dimensional discrete Fourier transform (DFT) [71][72] given by

$$F(u,v) = \frac{1}{MN}\sum_{x=0}^{M-1}\sum_{y=0}^{N-1} f(x,y)\exp\left[-j2\pi ux/M\right]\exp\left[-j2\pi vy/N\right] \tag{5.1}$$

where $u = 0,1,2,\ldots,M-1$, and $v = 0,1,2,\ldots,N-1$. In general, $f(x,y)$ represents an image in the spatial domain. The variables u and v are frequency variables. In the B- or B'-scan image representation, $f(x,y)$ can be replaced by $f(x,t)$, which is a function of two discrete (spatial and time) variables x and t. The two-dimensional DFT plays a critical role in a broad range of image processing applications. The magnitude and phase spectrum used in two-dimensional feature extraction can be written as, respectively,

$$|F(u,v)| = \left[\mathrm{Re}^2(F(u,v)) + \mathrm{Im}^2(F(u,v))\right]^{1/2} \tag{5.2}$$

and

$$\phi(u,v) = \tan^{-1}\left[\frac{\mathrm{Im}(F(u,v))}{\mathrm{Re}(F(u,v))}\right]. \tag{5.3}$$

The discrete Fourier transform in Equation (5.1) can be expressed in the separable form

$$F(u,v) = \frac{1}{M}\sum_{x=0}^{M-1}\exp(-j2\pi ux/M)\left[\frac{1}{\mathrm{N}}\sum_{y=0}^{N-1}f(x,y)\exp(-j2\pi vy/N)\right] \tag{5.4}$$

where $u = 0,1,2,\ldots,M-1$ and $v = 0,1,2,\ldots,N-1$. The principal advantage of the separability property is that *F(u,v)* can be obtained in two steps by successive applications of the one-dimensional Fourier transform. In other words, the two-dimensional function *F(u,y)* is obtained by taking a transform along each row of *f(x,y)*, and then *F(u,v)* is obtained by taking a transform along each column of *F(u,y)*. Another important property in the frequency domain is a conjugate symmetry. In the following description, we consider the image size as a square array, M=N. As in the case of one-dimensional Fourier transform, the two-dimensional DFT is periodic with period *N*, i.e.,

$$F(u,v) = F(u+N,v) = F(u,v+N) = F(u+N,v+N). \tag{5.5}$$

The validity of this property can be demonstrated by direct substitution of the variables *(u+N)* and *(v+N)* in Equation (5.1). Because of the periodicity, usually only the range $-\pi \leq u,v \leq \pi$ is displayed, which translates into the N values of each variable in any one period. Therefore, one period of the transform is necessary to specify *F(u,v)* completely in the frequency domain. Furthermore, the conjugate symmetry property of two-dimensional

DFT is also useful for feature extraction. Figure 5.3 shows diagonal symmetry on a transformed domain. For instance, for real valued signals, $f(x,y)$ is real. Using the conjugate symmetry property of Fourier transform, we have

$$F(u,v) = F^*(-u,-v) \tag{5.6}$$

and the magnitude of $F(u,v)$ is

$$|F(u,v)| = |F(-u,-v)| \tag{5.7}$$

where $F^*(-u,-v)$ is the complex conjugate of $F(u,v)$. As a special case, if $f(x,t)$ is real and symmetric in spatial domain, the magnitude of the Fourier spectrum has the following symmetry property.

$$F(u,v) = F(u,-v) = F(-u,v) = F(-u,-v) \tag{5.8}$$

As shown in Equations (5.5) and (5.7), the periodicity property indicates that $F(u,v)$ has a period of length N. The symmetry property shows quadrants of the Fourier transform after multiplication by the factor $(-1)^{x+y}$ prior to the Fourier transform.

$$F(u-N/2, v-N/2) = \frac{1}{N}\sum_{x=0}^{N-1}\sum_{y=0}^{N-1} f(x,y)(-1)^{x+y} \exp[-j2\pi ux/N] \exp[-j2\pi vy/N] \tag{5.9}$$

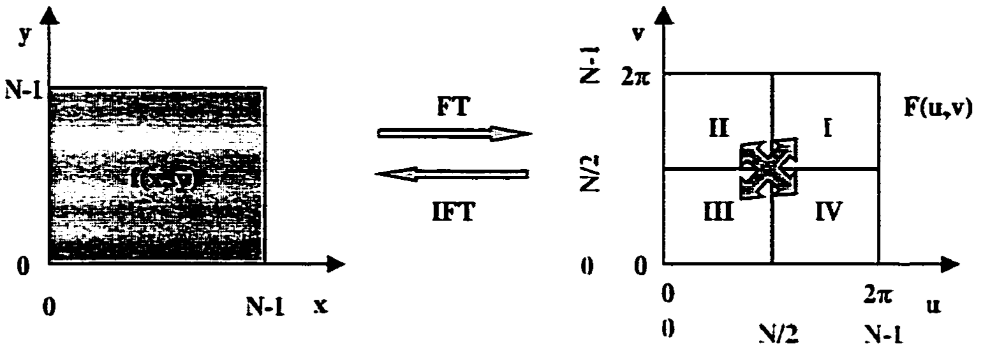

Figure 5.3 The diagonal symmetry on transformed domain *F(u,v)*.

The centering process swaps the first and third quadrants and second and fourth quadrants of transformed spectrum, *F(u,v)*. As a result of the conjugate symmetry property, one-half of the transform domain samples are sufficient to fully represent the information in *f(x,y)*. Since the dynamic range of a Fourier transformed image is in general very highly valued, the spectra can only be visible on the brightest part. In order to avoid compressing the high values in Fourier spectra and the logarithmic magnitude of the DFT, $\log|F(u,v)|$ is used. This method helps to bring out more details of the Fourier transform in regions where *F(u,v)* is very close to zero. Figure 5.4 shows an example of magnitude and phase spectrum of Fourier transform, which can be useful for feature extraction.

5.2 Two-dimensional Feature Extraction

An image feature is a distinguishing primitive characteristic or attribute of an image. In feature selection, the discriminatory attributes using diagonal and conjugate symmetry on two-dimensional Fourier transform can be chosen as a feature vector. Three

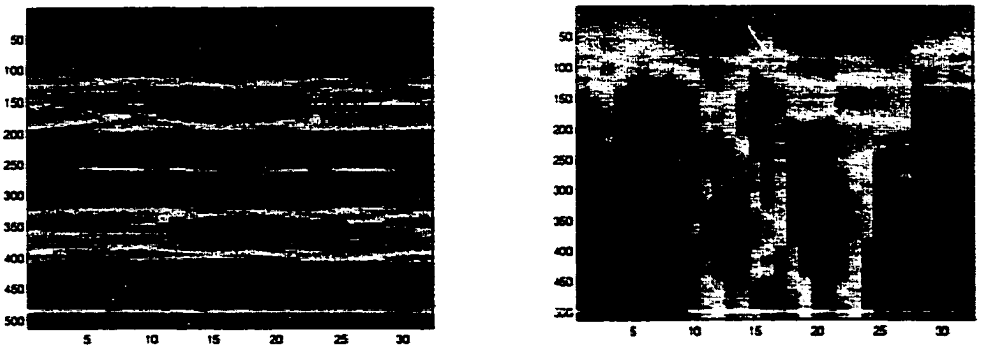

(a) (b)

Figure 5.4 Examples of Fourier transform: (a) magnitude (b) phase spectrum.

different feature selections, namely, magnitude, phase, and combined magnitude and phase, are described in following section.

1. Feature A - Magnitude

The magnitude, in general, represents the most intuitive feature of one-dimensional or two-dimensional spectral data. Figure 5.5 shows two-dimensional Fourier transform magnitudes of B- and B'-scan images for four classes. As can be seen, it is difficult to extract discriminatory features manually from the transform domain. However, using the diagonal symmetry property, the upper left quadrant (II) or upper right quadrant (I) can be chosen as a candidate for obtaining a reduced feature vector. In this research investigation, second quadrant coefficients were chosen as a feature vector and is expressed as

$$M_{II}(i,j) = \left\{ F(u,v) \,\|\, 0 \le u < M/2, \mathrm{N}/2 \le v \le N-1 \right\} \tag{5.10}$$

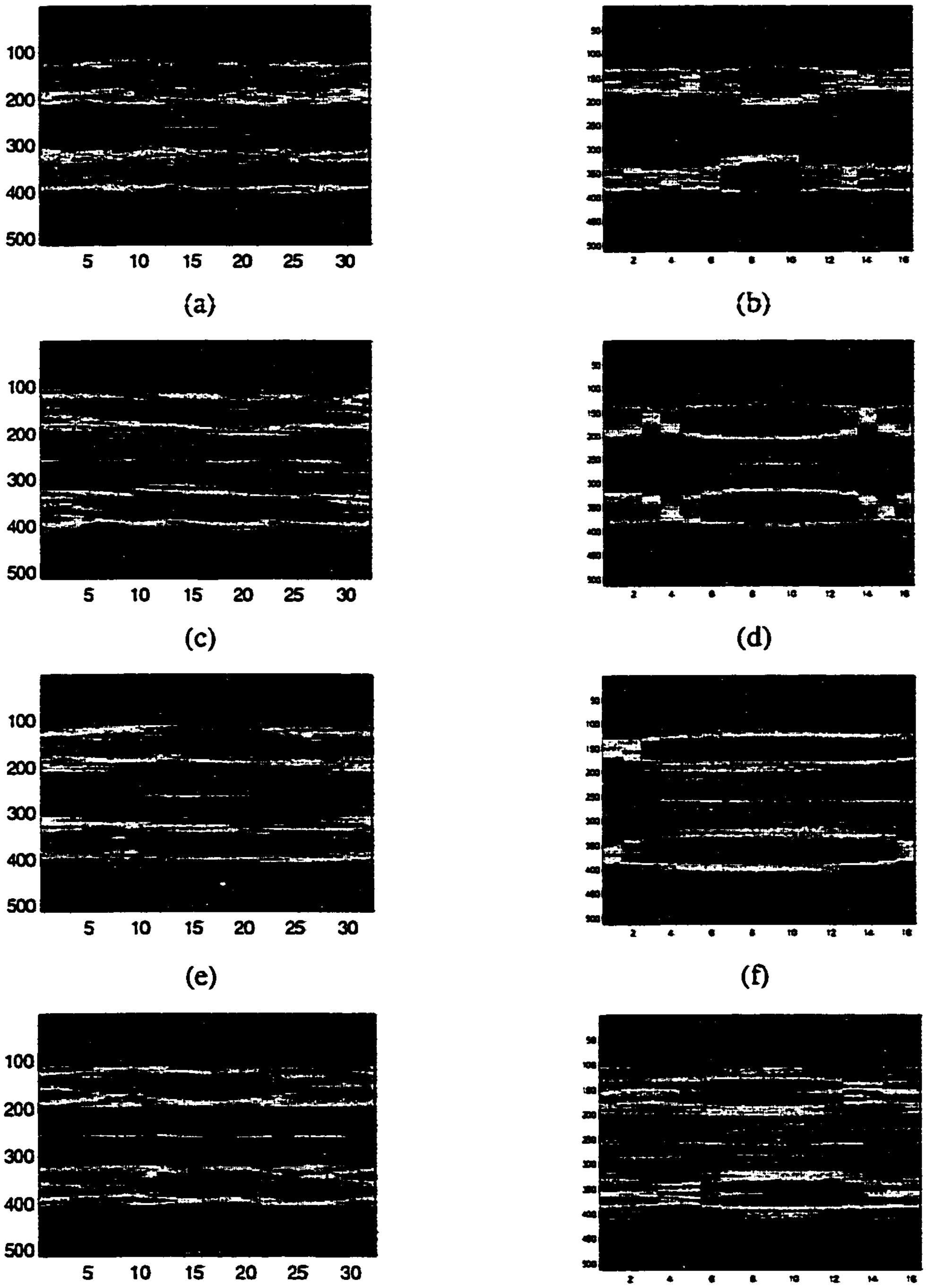

(a) (b)

(c) (d)

(e) (f)

(g) (h)

Figure 5.5 Two-dimensional magnitude spectra of four classes with B- and B'-scans. Each row shows crack, slag, porosity, and lack of fusion, respectively. Each column shows B-scan and B'-scan images.

where $0 \le i < M/2, 0 \le j < N/2$. Therefore, the size of feature matrix is M/2 x N/2. The feature matrix is converted into a one-dimensional vector format by concatenating the columns

$$\mathrm{M}_{feature} = [M_{II}(i, j=0) \quad M_{II}(i, j=1) \quad \bullet \quad \bullet \quad M_{II}(i, j=N/2-1)] \quad i = 0,1,2,\ldots,M/2-1 \tag{5.11}$$

and is used as input to a classifier.

2. Feature B - Phase Angle

The phase information in a two-dimensional Fourier transform is sometimes more useful than the magnitude of Fourier Transform, particularly in ultrasonic signals. Figure 5.6 shows the phase spectra for all four classes and the corresponding average value of all rows, Φ_v, along frequency variable v, where

$$\Phi_v(i) = \frac{1}{M}\sum_{u=0}^{M-1}\phi(u,i), \quad for\, i = 0,1,2,\ldots,N/2-1. \tag{5.12}$$

3. Feature C - Combined Magnitude and Phase

In signal classification systems, the selected features are optimized to yield (i) linear separability of classes and (ii) reduced dimensionality of data. Often, the class separability is improved by using a combination of features. In this work, the magnitude and phase spectra data are used in identifying a new feature vector. The first moment of the magnitude and

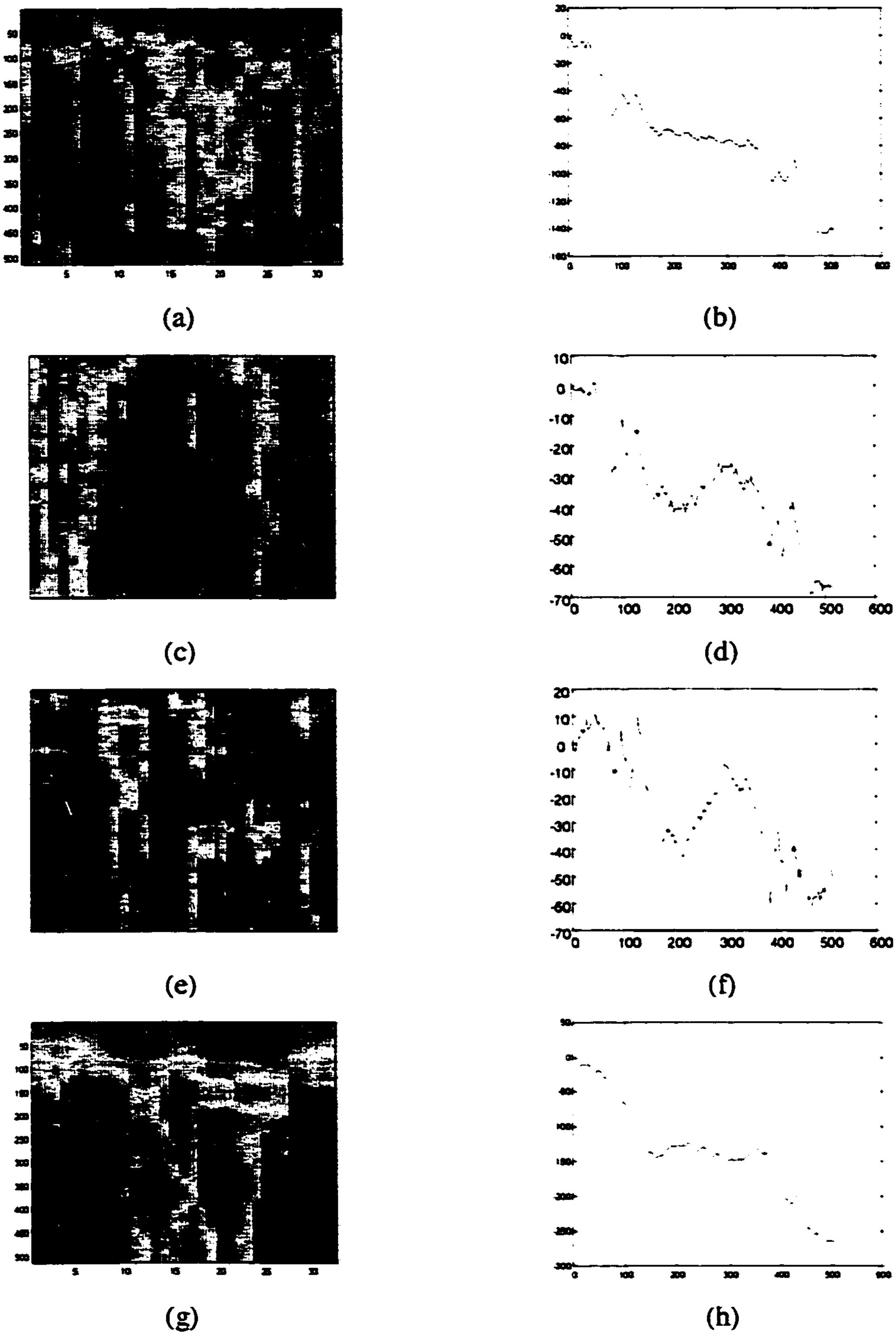

Figure 5.6 Phase spectra and average Φ_v along frequency variable v of four classes. Each row shows crack, slag, porosity, and lack of fusion, respectively. Each column shows B-scan and B'-scan images.

phase of the two-dimensional Fourier transform are used as a combined 2M long feature vector. The first moment of magnitude feature in the same manner like feature B can be written as

$$M_v(i) = \frac{1}{M}\sum_{u=0}^{M-1} F(u,i), \quad for\, i = 0,1,2,\dots, N/2-1. \tag{5.13}$$

Finally, the combined feature vector can be expressed as

$$C_v(i) = \left[\frac{1}{M}\sum_{u=0}^{M-1} F(u,i) \quad \frac{1}{M}\sum_{u=0}^{M-1} \phi(u,i) \right] \tag{5.14}$$

where for $i = 0,1,2,\dots, N/2-1$. The feature vectors for all four classes are shown in Figure 5.7.

5.3 Experimental Results

Twenty-eight C-scan images, equally distributed among the four classes, were obtained by using an automated scanning system with a 5MHz transducer and a 60° wedge angle. The resulting data was sampled at 25 MHz. The feature vectors were computed and applied to an MLP network for classification. The overall classification scheme is shown in Figure 5.8 and consists of the following steps:

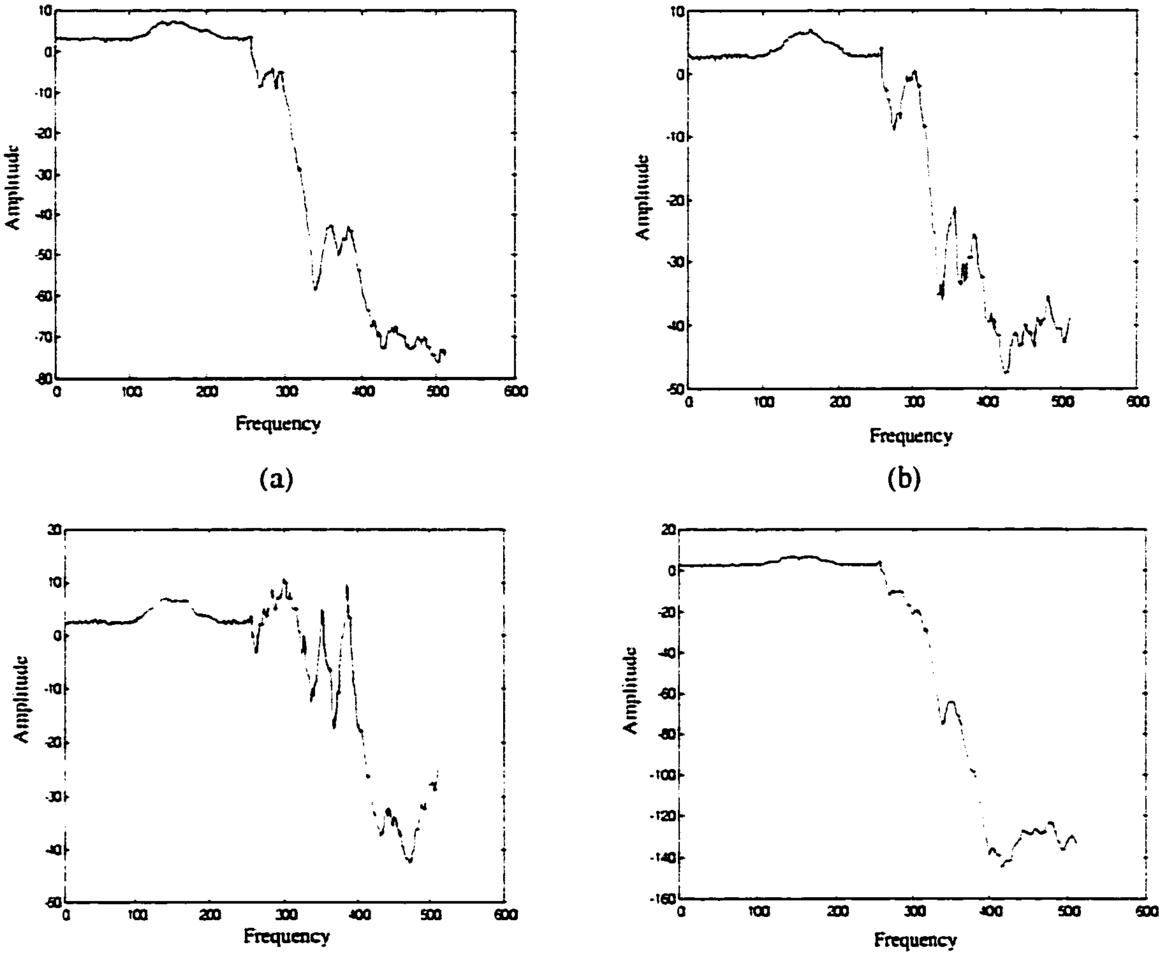

(a) (b)

(c) (d)

Figure 5.7 The combined feature vector plots for the first moment of the magnitude and phase along frequency variable v of four classes – (a) crack, (b) slag, (c) porosity, and (d) lack of fusion.

1. Select a region of interest (ROI) on a C-scan image.

   The ROI in a C-scan image can be defined as

$$\mathrm{ROI}(x,y) = \{f(x,y) | x = x_0, x_1, x_2, ..., x_m, \text{ and } y = y_0, y_1, y_2, ..., y_n \} \tag{5.15}$$

   where, $x_i = x_0 + i\Delta x, i = 1,2,....,m$, and $y_j = y_0 + j\Delta y, j = 1,2,....,n$. Δx and Δy are increment on x and y axis, respectively.

2. Obtain B- and B'-scans from an ROI.

   In the ROI, the data is three dimensional represented by ROI(x,y,t) as shown in Figure 5.9 where (x,y) represents the spatial coordinates of a transducer. Therefore, B- and B'-scan images can be written as

$$\mathrm{B}_{\mathrm{ROI}}(y,t) = \{ROI(x_0, y, t) \mid y = y_i, \ i = 0,1,2,....,n, \ t_1 \le t \le t_2 \} \tag{5.16}$$

   and

$$\mathrm{B'}_{\mathrm{ROI}}(x,t) = \{ROI(x, y_0, t) \mid x = x_i, \ i = 0,1,2,....,m, \ t_1 \le t \le t_2 \} \tag{5.17}$$

   where t_1 and t_2 are time gates. For each ROI image of m x n, m B-scan images and n B'-scan images are generated.

   For each B- and B'-scan image,

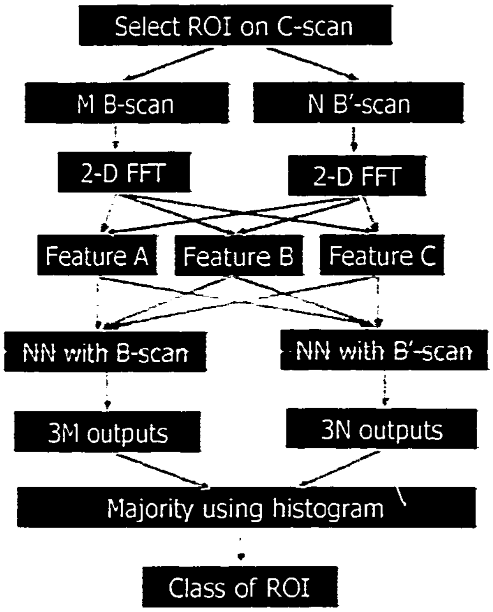

Figure 5.8 The overall scheme for multidimensional signal processing.

3. Create a fixed size image.

   Since the size of the ROI varies from one image to the other, the dimensionality of B_{ROI} and B'_{ROI} images needs to be first reduced or increased to a fixed size. This can be achieved by zero-padding, i.e.,

$$\mathrm{B}_{\mathrm{ROI}}(t_i, y) = \left[\begin{array}{cccc} & 0 & \cdot & 0 \\ & 0 & \cdot & 0 \\ B_{ROI}(x_0, y, t_i) & \cdot & \cdot & \cdot \\ & \cdot & \cdot & \cdot \\ & 0 & \cdot & 0 \end{array}\right] \quad (5.18)$$

where $n + n_{zp} = \hat{n} = 32$. Similarly, B'_{ROI} can be expressed as

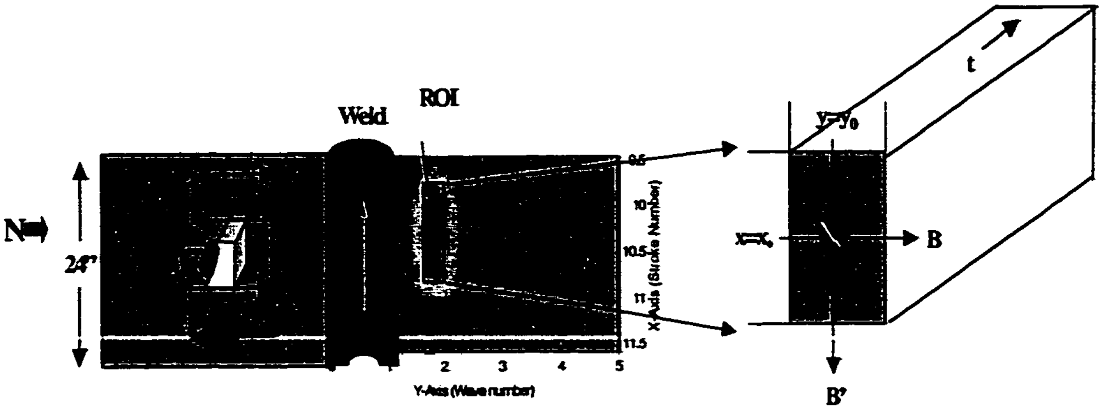

Figure 5.9 The geometry of ROI, B- and B'-scan images.

$$B'_{\mathrm{ROI}}(t_i,x)=\left[\begin{array}{cccc} & 0 & \cdot & 0\\ & 0 & \cdot & 0\\ B_{ROI}(x,y_0,t_i) & \cdot & \cdot & \cdot\\ & \cdot & \cdot & \cdot\\ & 0 & \cdot & 0\end{array}\right] \qquad (5.19)$$

where $m+m_{zp}=\hat{m}=16$.

4. Take two-dimensional Fourier transform to generate *F(u,v)*.
5. Select two-dimensional features.

   Three set of features, obtained using magnitude (Feature A), first moment of phase (Feature B), and combined first moment of magnitude and phase (Feature C) were selected.

6. Generate training data of feature vectors.

   The training data consist of 16 images from four classes.

7. Train B- and B'-networks.

   The neural networks are trained using the error back-propagation method with each feature sets A, B, and C.

8. Classify test images.

Signal classification was performed using the three different features, magnitude, phase, and combined magnitude and phase of the two-dimensional Fourier transform of B- and B'-scan images. The B-scan data analysis is summarized in Table 5.1 and 5.2. Each B-scan consists of fixed size 512 x 32. From step 1 through 4, the data are transformed into two-dimensional Fourier domain. Feature A generating images of size (256 by 16 points) is converted into a vector by concatenating the columns to give a 4096 elements long vector. Similarly, Feature B produces a vector phase information and Feature C is a vector of combined magnitude and phase information derived from the Fourier transform.

A MLP with two hidden layers of 40 and 12 nodes was trained. Of a total of 114 B-scan images, 60% images were used for training the network and the remaining 40% were used for testing. The detailed results on the test data are shown in Table 5.2. The procedure for preprocessing B'-scan data is similar to that used for B-scan data. The difference lies in the fact that the B'-scan image was 512 by 16 points, and the feature vector image is of size (256 x 8). The data distribution for training and test sets was summarized in Table 5.3. The classification performances using the 3 feature sets are shown in Table 5.4.

Two separate neural networks are used, one each for the B-scan and the B'-scan, respectively. During the classification phase, the B- and B'-scan images for a given flaw (C-scan image) are extracted and classified individually. In the classification of the C-scan image, the results of B- and B'-network are combined. Since each ROI image generates its own B- and B'-scan images, B-scan images are first passed through B-network, and B'-scan

Table 5.1 Distribution of B-scan images in each defect.

Number of images	Crack	Porosity	Slag	Lack of fusion
Train	19	14	11	24
Test	13	10	7	16
Total	32	24	18	40

Table 5.2 Summary of classification results using magnitude spectrum for B-scans.

Feature A

	Crack	Slag	Porosity	Lack of Fusion	Total
Crack	7	1	2	2	7/13
Slag	3	6	1		6/10
Porosity	1	1	5		5/7
Lack of Fusion	1	2	3	10	10/16
					28/46

Feature B

	Crack	Slag	Porosity	Lack of Fusion	Total
Crack	7	3	2	1	7/13
Slag	2	6	2	0	6/10
Porosity	0	1	6	0	6/7
Lack of Fusion	1	2	0	13	13/16
					32/46

Feature C

	Crack	Slag	Porosity	Lack of Fusion	Total
Crack	12	0	0	1	12/13
Slag	0	7	0	3	7/10
Porosity	0	1	6	0	6/7
Lack of Fusion	1	1	0	14	14/16
					39/46

Table 5.3 Distribution of B'-scan images in each defect.

Number of images	Crack	Porosity	Slag	Lack of fusion
Train	37	37	33	43
Test	26	26	23	30
Total	63	63	56	73

Table 5.4 Summary of classification results using magnitude spectrum for B'-scans.

Feature A

	Crack	Slag	Porosity	Lack of Fusion	Total
Crack	18	8			18/26
Slag	5	9	1	11	9/26
Porosity	6	2	15		15/23
Lack of Fusion	3	4	1	22	22/30
					64/105

Feature B

	Crack	Slag	Porosity	Lack of Fusion	Total
Crack	12	5	3	6	12/26
Slag	4	10	2	10	10/26
Porosity	7	3	13	0	13/23
Lack of Fusion	1	3	5	21	21/30
					56/105

Feature C

	Crack	Slag	Porosity	Lack of Fusion	Total
Crack	17	5	3	1	17/26
Slag	3	15	3	5	15/26
Porosity	1	0	17	5	17/23
Lack of Fusion	5	1	1	23	23/30
					72/105

images are passed through B'-network. The final classification for the C-scan image is obtained by combining the classifications of each of the B- and B'-scan images. A weighted majority voting technique is used to combine the results, and the C-scan is assigned to the resultant class. A majority voting technique finds the class of a number of B- and B'-scan images obtained from the selected ROI passed through the B- and B'-scan networks. The results of classification of the 28 C-scan images are shown in Table 5.5.

Unlike Feature B and C, Feature A produces a large dimensional input vector. A reduced dimension of feature vector can be determined by selecting a region of frequency spectrum using the following equations,

$$\begin{aligned} \mathrm{M}_{B.feature} &= \left[M_{II}(u,v),\ u = 1,2,\ldots,16\right] \\ \mathrm{M}_{B'feature} &= \left[M_{II}(u,v),\ u = 1,2,\ldots,8\right] \end{aligned} \qquad (5.20)$$

where v=101, 103, ... 200. The subband is selected on the basis of the distribution of the signal energy in various frequency bands. The reduced dimension of Feature A is [100 x 16] and is generated from B-scan data. The B'-scan data is processed similarly to obtain a feature vector of size [100 x 8]. These reduced dimension vectors are used as input for B- and B'-neural networks with two hidden layers of 40 and 12 nodes. The classification performance using the reduced Feature A is also shown in Table 5.5. As summarized in Table 5.5, although the training time was reduced relative to the large Feature A, the overall classification performance decreased significantly indicating loss of discriminatory information. More work need to be done in selecting the sub-region of the two-dimensional spectral phase that contain class discriminatory information.

Table 5.5 Summary of classification results for individual C-scans.

Feature A

	Crack	Slag	Porosity	Lack of Fusion	Total
Crack	6	1			6/7
Slag		7			7/7
Porosity			7		7/7
Lack of Fusion				7	7/7
					27/28

Feature A with a reduced dimension

	Crack	Slag	Porosity	Lack of Fusion	Total
Crack	4	2		1	4/7
Slag	1	3		3	3/7
Porosity	1		3	3	3/7
Lack of Fusion	1	2	1	3	3/7
					13/28

Feature B

	Crack	Slag	Porosity	Lack of Fusion	Total
Crack	6	1			6/7
Slag		7			7/7
Porosity			7		7/7
Lack of Fusion				7	7/7
					27/28

Feature C

	Crack	Slag	Porosity	Lack of Fusion	Total
Crack	7				7/7
Slag		7			7/7
Porosity			7		7/7
Lack of Fusion				7	7/7
					28/28

5.4 Principal Component Analysis (PCA)

Principal component analysis (PCA) is a well established tool in multivariate data analysis, which has been in use since 1901 [73]. The principal components are obtained using the eigenvectors of the covariance matrix. The diagonalization of the covariance matrix is sometimes called the Hotelling transform [74] or Karhunen-Loéve transform (KLT) [75][76]. The projection of data onto the eigenvector yields the principal components of the data.

In the signal processing community, principal component analysis is a linear transform that has been widely used in data analysis and compression. Principal component analysis is based on the statistical representation of a random variable [77]. Suppose we have a random vector population **x**, where

$$\mathbf{x}=\begin{bmatrix} x_1 \\ x_2 \\ \cdot \\ \cdot \\ x_n \end{bmatrix}. \tag{5.21}$$

The mean of that population is denoted by

$$\mu_{\mathbf{x}} = E\{\mathbf{x}\} \tag{5.22}$$

and the covariance matrix of the data set can be expressed as

$$\mathbf{C}_\mathbf{x} = E\{(\mathbf{x}-\boldsymbol{\mu}_\mathbf{x})(\mathbf{x}-\boldsymbol{\mu}_\mathbf{x})^T\}. \tag{5.23}$$

The elements of $\mathbf{C}_\mathbf{x}$, denoted by c_{ij}, represent the covariances between the random variable components x_i and x_j. The element c_{ii} is the variance of the component x_i and indicates the spread of the component around its mean value. If two components x_i and x_j of the data are uncorrelated, their covariance is zero $(c_{ij} = c_{ji} = 0)$. The covariance matrix is always real, symmetric, and positive definite. We can find an orthogonal matrix of eigenvectors of $\mathbf{C}_\mathbf{x}$ that diagonalizes the covariance matrix. The eigenvalues are derived by finding the solutions of the characteristic equation

$$|\mathbf{C}_\mathbf{x} - \lambda\mathbf{I}| = 0 \tag{5.24}$$

where the $\mathbf{I}$ is the identity matrix having the same order as $\mathbf{C}_\mathbf{x}$ and the $|\bullet|$ denotes the determinant of the matrix. For simplicity we assume that the λ_i are distinct. The corresponding eigenvalues λ_i are derived from the solutions of the equation

$$\mathbf{C}_\mathbf{x}\mathbf{e}_i = \lambda_i\mathbf{e}_i,\ i = 1,2,\ldots,n. \tag{5.25}$$

If the data vector has n components, the characteristic equation is of order n. Solving for eigenvalues and corresponding eigenvectors in general is a non-trivial task. Several numerical methods have been developed to solve this problem including the more recent neural solution [78]. Arranging the eigenvectors in the order of descending eigenvalues (largest first), one can create an ordered orthogonal basis with the first eigenvector having the direction of the largest variance of the data. In this way, we can find the directions in which the data set has the most significant amount of energy.

Suppose one has a data set of which the sample mean and the covariance matrix have been calculated. Let **A** be a matrix consisting of eigenvectors of the covariance matrix as the row vectors. By transforming a data vector **x** to vector **y**,

$$\mathbf{y} = \mathbf{A}(\mathbf{x} - \boldsymbol{\mu}_x) \qquad (5.26)$$

which is a point in the orthogonal coordinate system defined by the eigenvectors. Components of **y** are then coordinates in the orthogonal base. We can reconstruct the original data vector **x** from **y** by

$$\mathbf{x} = \mathbf{A}^T\mathbf{y} + \boldsymbol{\mu}_x \qquad (5.27)$$

where $\mathbf{A}^T$ is the transpose of a matrix **A**. Equation (5.26) is the projection of the original vector **x** on the coordinate axes defined by the orthogonal basis. Equation (5.27) is the reconstruction of the original vector using a linear combination of the orthogonal basis vectors.

Alternately, we can also project the data onto a subspace spanned by a subset of vectors of the orthogonal basis. If we denote the matrix having the first K eigenvectors as rows by $\mathbf{A}_K$, we can perform a similar transformation to get

$$\mathbf{y}_K = \mathbf{A}_K(\mathbf{x}-\boldsymbol{\mu}_x)\,. \tag{5.28}$$

The inverse transform is given by

$$\mathbf{x} = \mathbf{A}_K{}^T\mathbf{y}_K + \boldsymbol{\mu}_x\,. \tag{5.29}$$

This representation minimizes the mean-square error between the data and its representation for a given number of eigenvectors. In feature extraction, the general objective is to reduce the dimension of the representation and also preserve as much of the original information content as possible. PCA offers an efficient way to control the trade-off between loss of information and dimensionality reduction.

In this section, our effort was focused on the reduction of the input dimensionality of the feature vector. The experimental data used here were the same as the two-dimensional B- and B'-scan images from the classes namely, crack, slag, porosity, and lack of fusion. A total of 28 C-scan images, equally distributed among the four classes, were obtained by using an automated scanning system with a 5MHz transducer and a 60° wedge angle and sampled at 25 MHz. The feature vectors were computed and applied to an MLP network for classification. The overall classification scheme is shown in Figure 5.10. In this classification scheme, the features used were principal components augmented by means of magnitude and phase spectra as described below. Steps 1 through 5 are similar to those described in section 5.3 (Refer Figure 5.9).

1. Select a region of interest (ROI) on C-scan image.

   The ROI in a C-scan image can be defined as

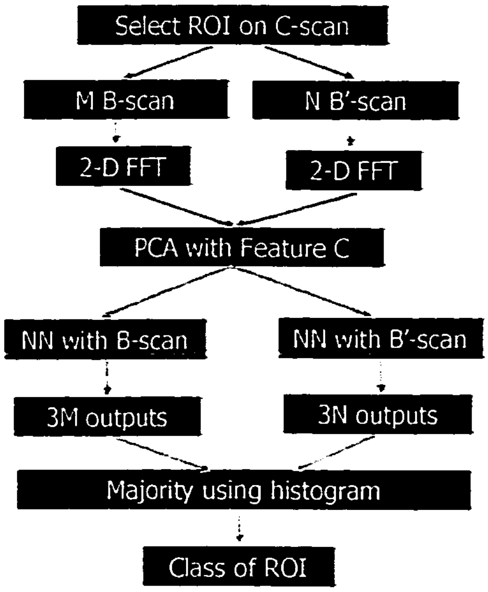

Figure 5.10 The overall classification scheme for multidimensional signal processing using PCA.

$$\mathrm{ROI}(x,y)=\{f(x,y)\,|\,x=x_0,x_1,x_2,\ldots,x_m,\ \text{and}\ y=y_0,y_1,y_2,\ldots,y_n\ \} \qquad (5.30)$$

where, $x_i = x_0 + i\Delta x, i = 1,2,\ldots,m$, and $y_j = y_0 + j\Delta y, j = 1,2,\ldots,n$. Δx and Δy are increment on x and y axis, respectively.

2. Obtain B- and B'-scans from a ROI.

In the ROI, B- and B'-image are obtained by scanning the spatial coordinate (x,y) of a transducer and can be written as

$$\mathrm{B}_{\mathrm{ROI}}(y,t)=\{ROI(x_0,y,t)\,|\,y=y_i,\ i=0,1,2,\ldots,n,\ t_1\le t\le t_2\ \} \qquad (5.31\text{-a})$$

$$\mathrm{B'}_{\mathrm{ROI}}(x,t)=\{ROI(x,y_0,t)\,|\,x=x_i,\ i=0,1,2,\ldots,m,\ t_1\le t\le t_2\ \} \qquad (5.31\text{-b})$$

where t_1 and t_2 are time gates.

For each B- and B'-scan image,

3. Create a fixed size image.

   Since the size of the ROI varies from one image to the other, the dimensionality of B_{ROI} and B'_{ROI} images needs to be first reduced or increased to a fixed size with zero-padding. The resized data consists of

$$\mathrm{B}_{\mathrm{ROI}}(t_i, y) = \begin{bmatrix} & 0 & \cdot & 0 \\ & 0 & \cdot & 0 \\ B_{ROI}(x_0, y, t_i) & \cdot & \cdot & \cdot \\ & \cdot & \cdot & \cdot \\ & 0 & \cdot & 0 \end{bmatrix} \tag{5.32-a}$$

$$\mathrm{B}'_{\mathrm{ROI}}(t_i, x) = \begin{bmatrix} & 0 & \cdot & 0 \\ & 0 & \cdot & 0 \\ B_{ROI}(x, y_0, t_i) & \cdot & \cdot & \cdot \\ & \cdot & \cdot & \cdot \\ & 0 & \cdot & 0 \end{bmatrix} \tag{5.32-b}$$

   The dimension of resized B_{ROI} and B'_{ROI} images are [512 x ($n+n_{zp}=\hat{n}=32$)] and [512 x ($m+m_{zp}=\hat{m}=16$)], respectively.

4. Compute two-dimensional Fourier transform.

   The two-dimensional Fourier transform is computed using the following definition:

$$F(u,v)=\frac{1}{MN}\sum_{x=0}^{M-1}\sum_{y=0}^{N-1} f(x,y)\exp\left[-j2\pi ux/M\right]\exp\left[-j2\pi vy/N\right] \tag{5.33}$$

where $u = 0,1,2,\ldots,M-1$. and $v = 0,1,2,\ldots,N-1$. The dimensionality of $F(u,v)$ for B

$\mathrm{B_{ROI}}$ and $\mathrm{B'_{ROI}}$ is

$$Dim\{F(u,v)\} = \begin{cases} 512\times\hat{n}, & \text{for } \mathrm{ROI_B} \\ 512\times\hat{m}, & \text{for } \mathrm{ROI_{B'}} \end{cases}. \tag{5.34}$$

5. Compute the first moment of two-dimensional spectra.

As described in Section 5.2, the average values of all rows along frequency variable v of the magnitude and phase spectra are obtained by

$$M_v(i) = \frac{1}{M}\sum_{u=0}^{M-1} F(u,i), \quad for\ i = 0,1,2,\ldots,N/2-1. \tag{5.35-a}$$

$$\Phi_v(i) = \frac{1}{M}\sum_{u=0}^{M-1} \phi(u,i), \quad for\ i = 0,1,2,\ldots,N/2-1. \tag{5.35-b}$$

and finally the combined feature vector (CFV) can be expressed as

$$\mathrm{CFV}_v(i) = \left[\frac{1}{M}\sum_{u=0}^{M-1} F(u,i), \quad \frac{1}{M}\sum_{u=0}^{M-1} \phi(u,i)\right] \tag{5.36}$$

where for $i = 0,1,2,\ldots,N/2-1$.

6. Normalize the data.

The normalization of the data (F) of size of M x N is calculated by

$$\hat{F}_{i,j} = \frac{F_{i,j} - \mu_i}{\sigma_i}, i = 1,2,\ldots,M \tag{5.37}$$

where

$$\mu_i = \frac{1}{N}\sum_{j=1}^{N} F_{i,j}, i = 1,2,\ldots,M, j = 1,2\ldots N. \tag{5.38-a}$$

$$\sigma_i = \left(\frac{1}{N}\sum_{j=1}^{N} F_{i,j} - \mu_i\right)^{1/2}, i = 1,2,\ldots,M, j = 1,2\ldots N. \tag{5.38-b}$$

7. Compute the covariance matrix, eigenvalues, and eigenvectors.

The covariance matrix for each class (crack, slag, porosity, and lack of fusion) is calculated by

$$\mathbf{C}_{p\times p} = \begin{bmatrix} c_{11} & c_{12} & \cdot & \cdot & c_{1p} \\ c_{21} & c_{22} & \cdot & \cdot & c_{2p} \\ \cdot & \cdot & \cdot & \cdot & \cdot \\ \cdot & \cdot & \cdot & \cdot & \cdot \\ c_{p1} & c_{p2} & \cdot & \cdot & c_{pp} \end{bmatrix} \tag{5.39}$$

where the element c_{ij} of **C** being defined as

$$c_{ij} = E[(\mathbf{F}_i - \boldsymbol{\mu}_i)(\mathbf{F}_j - \boldsymbol{\mu}_j)T]. \tag{5.40}$$

The characteristic equation of $\mathbf{C}_{p\times p}$ is a polynomial of degree *p*, which is obtained by expanding the determinant of

$$\left|\mathbf{C}_{p\times p}-\lambda\mathbf{I}\right|=\begin{vmatrix} c_{11}-\lambda & \cdot & \cdot & c_{1p}-\lambda \\ \cdot & c_{22}-\lambda & \cdot & \cdot \\ \cdot & \cdot & \cdot & \cdot \\ c_{p1}-\lambda & \cdot & \cdot & c_{pp}-\lambda \end{vmatrix}=0 \tag{5.41}$$

and solving for the roots λ. Specifically, the largest eigenvalue, λ_1, and its associated vector, $\mathbf{v}_1$, are corresponding. Figure 5.11 shows the largest eigenvalues of the covariance matrix of the four classes.

8. Compute the principal components (PC).

Let $\mathbf{V}_{crk}$, $\mathbf{V}_{slg}$, $\mathbf{V}_{por}$, and $\mathbf{V}_{lof}$ be K significant eigenvectors of the estimated covariance matrices, $\mathbf{C}_{crk}$, $\mathbf{C}_{slg}$, $\mathbf{C}_{por}$, and $\mathbf{C}_{lof}$ of crack, slag, porosity, and lack of fusion, respectively. Then, the principal component features of a data set $\mathbf{F}$ are obtained using the projections

$$PC_{crk}=E[\mathbf{F}^T\mathbf{V}_{crk}] \tag{5.42-a}$$

$$PC_{slg}=E[\mathbf{F}^T\mathbf{V}_{slg}] \tag{5.42-b}$$

$$PC_{por}=E[\mathbf{F}^T\mathbf{V}_{por}] \tag{5.42-c}$$

$$PC_{lof}=E[\mathbf{F}^T\mathbf{V}_{lof}] \tag{5.42-d}$$

Finally, the overall feature vector based on PCA can be expressed as

$$PC=[PC_{crk}\ \ PC_{slg}\ \ PC_{por}\ \ PC_{lof}]. \tag{5.43}$$

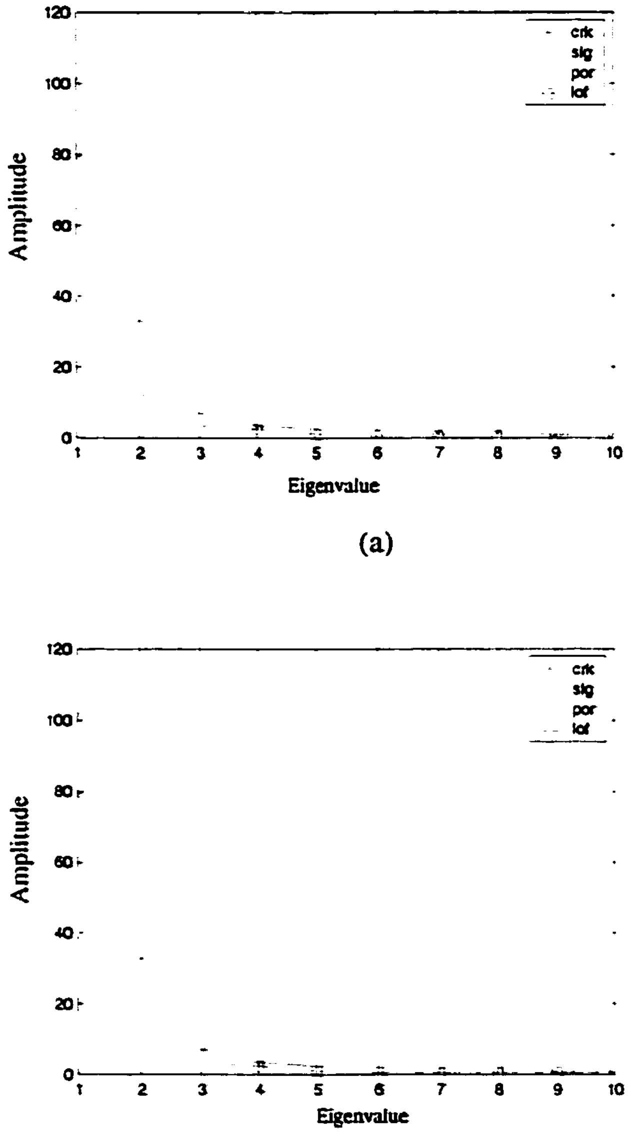

(a)

(b)

Figure 5.11 Eigenvalues of the covariance matrix: (a) B-scan data (b) B'-scan data.

9. Train B- and B'-networks.

10. Classify test images.

In principal component analysis, the key factor is the selection of eigenvalues. There is, however, no general criterion for selecting the number of eigenvalues. In this research, based on the largest eigenvalues, a set of 11 eigenvalues was chosen for each class. Each class is presented by 11 eigenvectors derived from the training data in that class. Each training data is projected onto the 44 eigenvectors to generate a 44-dimensional feature vector. A neural network of architecture 44-20-8-4 was trained and used for classification. In the classification phase, the B- and B'-scan images for a given flaw (C-scan image) are extracted and classified individually. In the classification of principal component features, the overall classification performance was comparable to two-dimensional features processed in Section 5.3. In addition, the training time was reduced because of lower dimensionality. Tables 5.6 and 5.7 summarize the data distribution and classification results for B- and B'-scan data. The final classification for the C-scan image is obtained by combining the classifications of each of the B- and B'-scan images as explained in the previous section. Again, a weighted majority voting technique is used to combine the results, and the C-scan is assigned to the resultant class. The results of classification of the 28 C-scan images are shown in Table 5.8.

5.5 Three-dimensional Moment Analysis

In ultrasonic weld inspection, the transducer scans a two-dimensional plane with an A-scan acquired at each spatial point. Processing the data in its entirety involves using the information in the three-dimensional volume for classification. In order to compute features that capture all the information, this section introduces three-dimensional spatial moments of

Table 5.6 Summary of data distribution and classification results of training and testing data using PCA for B-scans.

Data distribution

Number of images	Crack	Porosity	Slag	Lack of fusion
Train	22	17	13	28
Test	10	7	5	12
Total	32	24	18	40

Training data

	Crack	Slag	Porosity	Lack of fusion	Total
Crack	22	0	0	0	22/22
Slag	0	17	0	0	17/17
Porosity	0	0	13	0	13/13
Lack of fusion	0	0	0	28	28/28
					80/80

Testing data

	Crack	Slag	Porosity	Lack of fusion	Total
Crack	8	0	0	2	8/10
Slag	0	5	1	1	5/7
Porosity	0	1	4	0	4/5
Lack of fusion	2	0	0	10	10/12
					27/34

Table 5.7 Summary of data distribution and classification results of training and testing data using PCA for B'-scans.

Data distribution

Number of images	Crack	Porosity	Slag	Lack of fusion
Train	44	44	39	51
Test	19	19	17	22
Total	63	63	56	73

Training data

	Crack	Slag	Porosity	Lack of fusion	Total
Crack	44	0	0	0	44/44
Slag	0	44	0	0	44/44
Porosity	0	0	39	0	39/39
Lack of fusion	0	0	0	51	51/51
					178/178

Testing data

	Crack	Slag	Porosity	Lack of fusion	Total
Crack	13	3	1	2	13/19
Slag	5	10	2	2	10/19
Porosity	1	2	13	1	13/17
Lack of fusion	2	3	0	17	17/22
					53/77

Table 5.8 Summary of classification results using PCA for individual C-scans.

	Crack	Slag	Porosity	Lack of Fusion	Total
Crack	7				7/7
Slag		7			7/7
Porosity			7		7/7
Lack of Fusion				7	7/7
					28/28

the ultrasonic volumetric data. The three-dimensional moment, in general, is defined as

$$M(p,q,r)=\frac{1}{L^p N^q M^r}\sum_{t=1}^{L}\sum_{y=1}^{N}\sum_{x=1}^{M} x^p y^q t^r V(x,y,t) \tag{5.44}$$

where p, q, and r are the orders of moments. Here $V(x,y,t)$ indicates the volume of data with x=1,2,...,M, y=1,2,...,N and t=1,2,...,L. Clearly, the zero order spatial moment (zero-order moment) is given by

$$M(0,0,0)=\sum_{t=1}^{L}\sum_{y=1}^{N}\sum_{x=1}^{M} V(x,y,t) \tag{5.45}$$

where M(0,0,0) is the sum of the voxel values. The ratios

$$\begin{aligned}\bar{x}&=\frac{M(1,0,0)}{M(0,0,0)}\\ \bar{y}&=\frac{M(0,1,0)}{M(0,0,0)}\\ \bar{t}&=\frac{M(0,0,1)}{M(0,0,0)}\end{aligned} \tag{5.46}$$

of first-order to zero-order spatial moments define the centroid of the volume data. With the ratios, we can define other order spatial central moments of a discrete volume as

$$M(p,q,r)=\frac{1}{L^p N^q M^r}\sum_{t=1}^{L}\sum_{y=1}^{N}\sum_{x=1}^{M}[x-\bar{x}]^p[y-\bar{y}]^q[t-\bar{t}]^r V(x,y,t). \tag{5.47}$$

In three-dimensional signal classification, the spatial moments can serve as a candidate for features to be used in classification. This research initially was focused on the two-class problem namely, planar vs. volumetric flaws. In this problem, crack and lack of fusion belong to the planar defect type, whereas porosity and slag belong to the volumetric flaw type. In order to get a moment-based feature vector, we investigated moments of order ($p+q+r$) with p=0,1,2,3, q=0,1,2,3 and r=0,1,2,3. Figure 5.12 shows the 64 ($p+q+r$) order moments for the four flaws. In this figure, the horizontal axis indicates the index number of the data files and vertical axis indicates ($p+q+r$) order moment values. For example, (p=1,q=1,r=2) indicates 22nd order moment on the vertical axis. As can be seen in Figure 5.12, the moment distribution of each class distinguished the flaw type.

The moment distribution of the volumetric flaw (slag and porosity) is different than that of planar scatters (crack and lack of fusion). A neural network classification with one hidden layer of size 12 was trained to classify the moment vectors. The network training time was very short compared to a two-dimensional classification. Table 5.9 summarizes the data distribution and classification results obtained.

5.6 Three-dimensional Fourier Transform

An alternate choice for features representing volumetric data is to consider the three-dimensional spectral domain. In order to analyze the full three-dimensional volume of data, this process was extended to three-dimensional DFT pair which is defined as

$$F(u,v,w)=\sum_{x=0}^{N-1}\sum_{y=0}^{N-1}\sum_{z=0}^{N-1} f(x,y,z)W_N^{ux+vy+wz} \qquad \text{for } u,v,w=0,1,2,\ldots,N-1. \qquad (5.48)$$

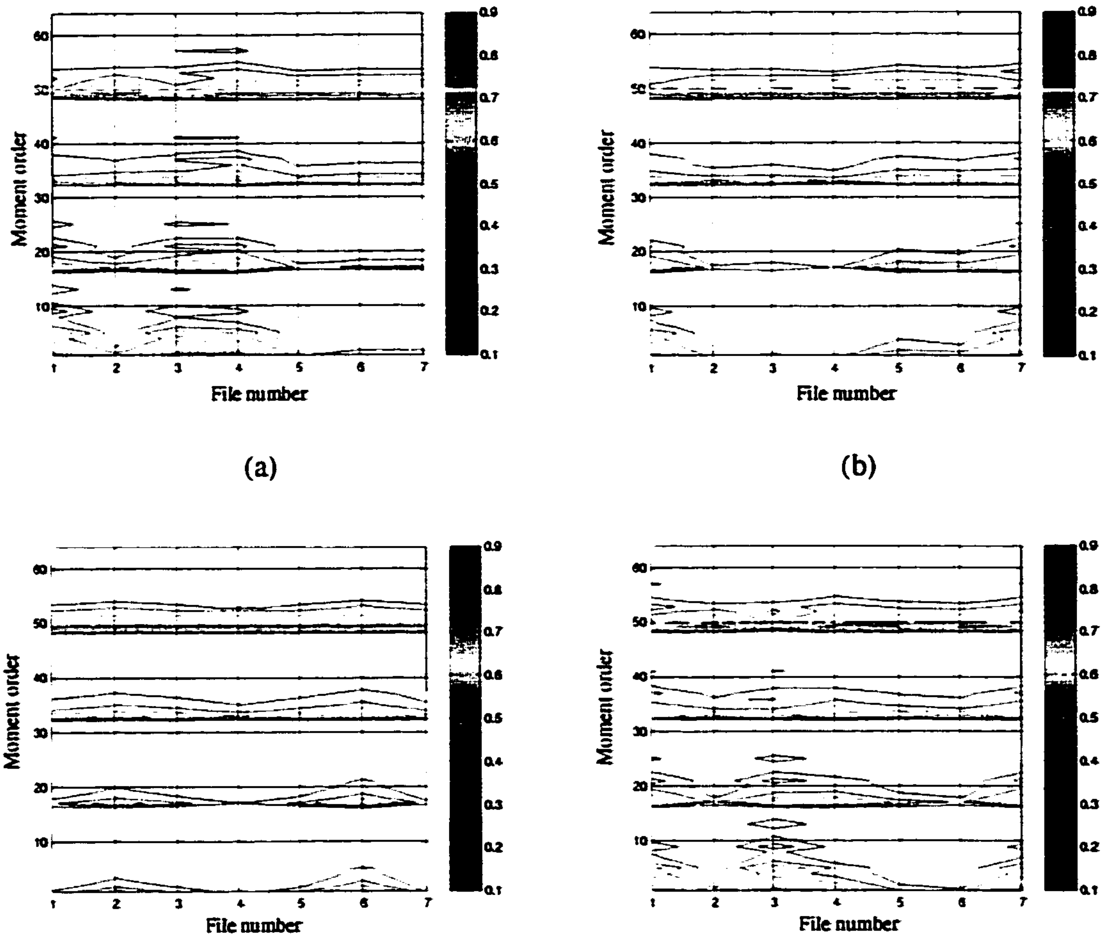

(a) (b)

(c) (d)

Figure 5.12 The spatial moments: (a) crack, (b) slag, (c) porosity, and (d) lack of fusion.

Table 5.9 Summary of data distribution and classification results of testing data using a spatial moment features – planar vs. volumetric.

Data distribution

Number of files	Planar	Volumetric
Train	8	8
Test	6	6
Total	14	14

Overall classification (training + testing data)

	Planar	Volumetric	Total
Planar	13	1	13/14
Volumetric	2	12	12/14

and

$$f(x,y,z)=\sum_{u=0}^{N-1}\sum_{v=0}^{N-1}\sum_{w=0}^{N-1}F(u,v,w)W_N^{-(ux+vy+wz)} \quad \text{for } x,y,z=0,1,2,\ldots,N-1 \qquad (5.49)$$

where $W_N=e^{-j2\pi/N}$ and $f(x,y,z)$ represents the volumetric data, which is a function of three discrete spatial variables (spatial) x, y and (time) z. The variables u, v, and w are the corresponding spatial and time frequency variables. The magnitude and phase spectrum are defined as

$$|F(u,v,w)|=\left[\mathrm{Re}^2(F(u,v,w))+\mathrm{Im}^2(F(u,v,w))\right]^{1/2} \qquad (5.50)$$

and

$$\phi(u,v,w)=\tan^{-1}\left[\frac{\mathrm{Im}(F(u,v,w))}{\mathrm{Re}(F(u,v,w))}\right] \qquad (5.51)$$

The separability, periodicity, and symmetry properties can be derived in the same manner as in the two-dimensional case. The discrete Fourier transform in Equation (5.8) can be expressed in the separable form

$$F(u,v,w) = \sum_{x=0}^{N-1} W_N^{ux} \sum_{y=0}^{N-1} W_N^{vy} \sum_{z=0}^{N-1} f(x,y,z) W_N^{wz} \tag{5.52}$$

for $u,v,w = 0,1,2,\ldots,N-1$. As can be seen in Equation (5.48), three-dimensional Fourier transform can be calculated sequentially along the three components. The three-dimensional periodicity with period N is expressed as

$$\begin{aligned} F(u,v,w) &= F(u+N,v+N,w) \\ &= F(u+N,v,w+N) \\ &= F(u,v+N,w+N) \\ &= F(u+N,v+N,w+N). \end{aligned} \tag{5.53}$$

The validity of this property can be demonstrated by direct substitution of the variables $(u+N)$, $(v+N)$, and $(w+N)$ in Equation (5.8). Here, only one period of the transform is necessary to specify $F(u,v,w)$ completely in the frequency domain.

The three-dimensional Fourier transform also exhibits a conjugate symmetry, which can be written as

$$F(u,v,w) = F^*(-u,-v,-w) \tag{5.54}$$

and the magnitude of $F(u,v,w)$ as

$$|F(u,v,w)| = |F(-u,-v,-w)| \tag{5.55}$$

where $F^*(-u,-v,-w)$ is the complex conjugate of $F(u,v,w)$. As in two-dimensional Fourier transform, after centering the transform in the frequency range [-π,π] in the transform domain, we can derive a diagonal symmetry property as shown in Figure 5.13.

Some simple examples of three-dimensional transforms are given below. Consider the three-dimensional discrete unit impulse, $\delta(n_1,n_2,n_3)$.

$$f(n_1,n_2,n_3) = \delta(n_1,n_2,n_3) = \begin{cases} 1, & n_1 = n_2 = n_3 = 0 \\ 0, & otherwise \end{cases} \tag{5.56}$$

The Fourier transform of the impulse function can be calculated as

$$\begin{aligned} F(u,v,w) &= \sum_{n_1=0}^{N_1-1}\sum_{n_2=0}^{N_2-1}\sum_{n_3=0}^{N_3-1} \delta(n_1,n_2,n_3) W_{N_3}^{wn_3} W_{N_2}^{vn_2} W_{N_1}^{un_1} \\ &= \sum_{n_1=0}^{N_1-1}\sum_{n_2=0}^{N_2-1} \delta(n_1,n_2) W_{N_2}^{vn_2} W_{N_1}^{un_1} \\ &= \sum_{n_1=0}^{N_1-1} \delta(n_1) W_{N_1}^{un_1} \\ &= 1 \end{aligned} \tag{5.57}$$

Next, consider a simple cube defined as

$$f(x,y,z) = \begin{cases} 1, & 0 \le x,y,z \le N-1 \\ 0, & otherwise \end{cases} \tag{5.58}$$

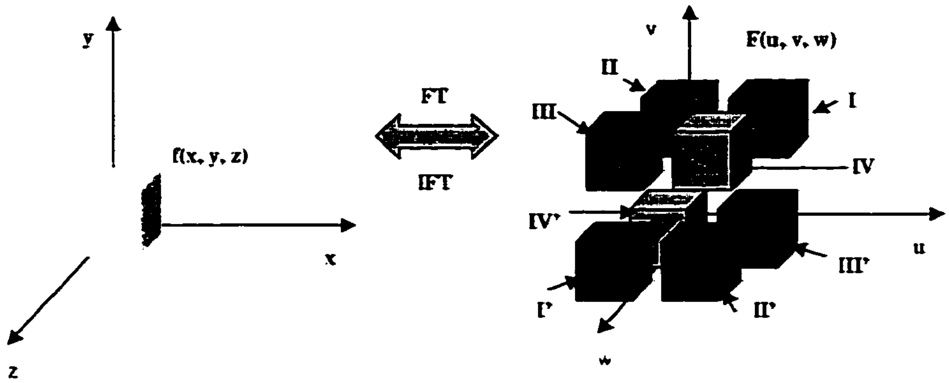

Figure 5.13 The diagonal symmetry on transformed domain *F(u,v,w)*.

which is real and symmetric, and where N=8. If f(x,y,z) is continuous and integrable, the three-dimensional Fourier transform $F(u,v,w)$ can be written as

$$F(u,v,w) = \iiint_{x,y,z} f(x,y,z)\exp[-j2\pi(ux+vy+wz)]dxdydz. \tag{5.59}$$

According to the above equation, the three-dimensional Fourier transform is calculated as the following.

$$\begin{aligned}F(u,v,w) &= \int_0^{N-1} e^{-j2\pi ux}dx \int_0^{N-1} e^{-j2\pi vy}dy \int_0^{N-1} e^{-j2\pi wz}dz \\ &= \left[\frac{e^{-j2\pi ux}}{-j2\pi u}\right]_0^{N-1} \left[\frac{e^{-j2\pi vy}}{-j2\pi v}\right]_0^{N-1} \left[\frac{e^{-j2\pi wz}}{-j2\pi w}\right]_0^{N-1} \\ &= \frac{1}{-j2\pi u}\left[e^{-j2\pi u(N-1)} - 1\right] \frac{1}{-j2\pi v}\left[e^{-j2\pi v(N-1)} - 1\right] \frac{1}{-j2\pi w}\left[e^{-j2\pi w(N-1)} - 1\right] \\ &= \frac{1}{j2\pi u}\left[e^{j\pi u(N-1)} - e^{-j\pi u(N-1)}\right] e^{-j\pi u(N-1)} \frac{1}{j2\pi u}\left[e^{j\pi u(N-1)} - e^{-j\pi u(N-1)}\right] e^{-j\pi u(N-1)} \\ &\quad \frac{1}{j2\pi u}\left[e^{j\pi u(N-1)} - e^{-j\pi u(N-1)}\right] e^{-j\pi u(N-1)} \\ &= \frac{\sin\{\pi u(N-1)\}e^{-j\pi u(N-1)}}{\pi u} \frac{\sin\{\pi v(N-1)\}e^{-j\pi v(N-1)}}{\pi v} \frac{\sin\{\pi w(N-1)\}e^{-j\pi w(N-1)}}{\pi w}.\end{aligned} \tag{5.60}$$

Therefore, the magnitude spectrum is

$$|F(u,v,w)| = \left|\frac{\sin\{\pi u(N-1)\}e^{-j\pi u(N-1)}}{\pi u}\right|\left|\frac{\sin\{\pi v(N-1)\}e^{-j\pi v(N-1)}}{\pi v}\right|\left|\frac{\sin\{\pi w(N-1)\}e^{-j\pi w(N-1)}}{\pi w}\right|. \tag{5.61}$$

In this case, the real and symmetric magnitude spectrum is shown in Figure 5.14. By applying three-dimensional Fourier transform, this thesis investigates the derivation of volumetric features of the ultrasonic data. A major drawback, however, is that this technique results in a very large dimension of the feature vector. For a volume of MxNx512, the length of the feature vector after taking into consideration the symmetry of the transform is so huge. One possible method to reduce the dimensionality is to consider the moments in the transform domain.

In order to investigate the feasibility of three-dimensional moment features in three-dimensional Fourier transform domain, the classification of the volumetric data was implemented in the same manner as in the three-dimensional spatial domain. In this study, the moment values were calculated using Equation (5.48). Again, this study has focused on the two-class problems namely, planar vs. volumetric type. The order $(p+q+r)$ indices for moment calculations used here to compute a three-dimensional Fourier transform moment feature are p=0,1,2,3, q=0,1,2,3 and r=0,1,2,3. Figure 5.15 shows a plot of the $(p+q+r)$ order moments for the four classes. The number of moments used here is 64, which is the number of input nodes in the neural network. The architecture of the MLP neural network is 64-12-2 nodes in input, hidden, and output layers, respectively. Table 5.10 summarizes the data distribution and classification results with the planar vs. volumetric case.

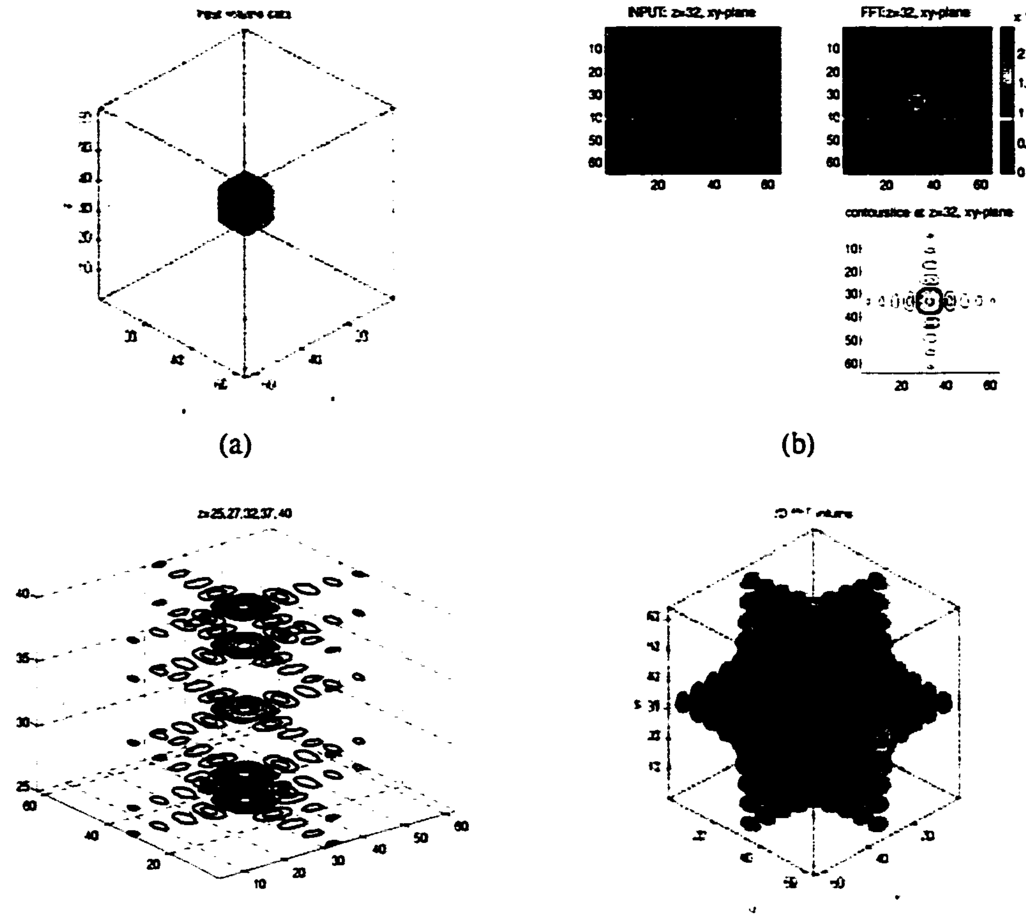

(a) (b)

(c) (d)

Figure 5.14 A synthetic three-dimensional Fourier transform (a) a cube data, (b) a magnitude spectrum of one slice with xy-plane at z=32 and its contour plot, (c) contour plots on z=25, 27, 32,37,40, and (d) three-dimensional DFT volume.

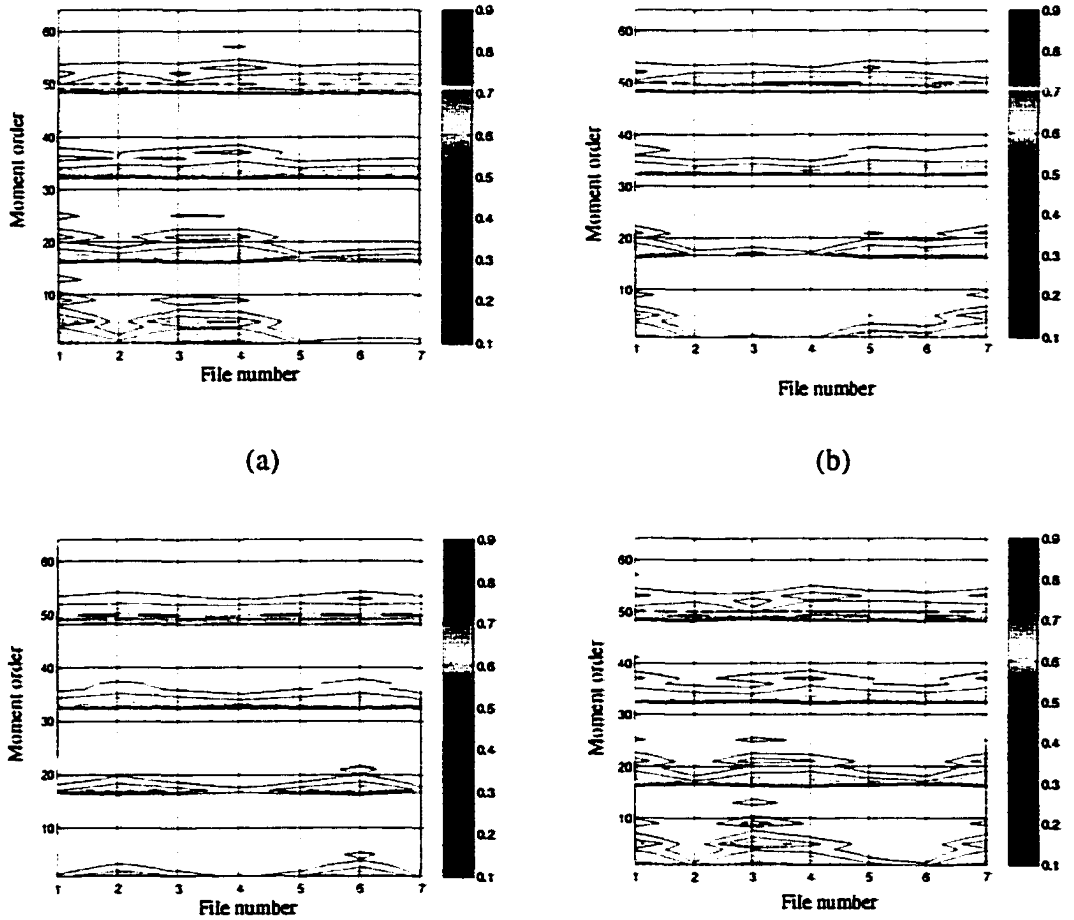

(a)

(b)

(c)

(d)

Figure 5.15 The three-dimensional Fourier transform moments: (a) crack, (b) slag, (c) porosity, and (d) lack of fusion.

Table 5.10 Summary of data distribution and classification results of testing data using a Fourier transform moment features – planar vs. volumetric.

Data distribution

Number of files	Planar	Volumetric
Train	8	8
Test	6	6
Total	14	14

Overall classification (training + testing data)

	Planar	Volumetric	Total
Planar	11	3	11/14
Volumetric	4	10	10/14

CHAPTER 6. CONCLUSIONS

6.1 Summary and Conclusions

This research was motivated by a desire to develop a complete ultrasonic signal processing and analysis package for interpretation of the data generated in a two-dimensional scan. Also, this research studied the limitations of split-spectrum processing. The basic problem with ultrasonic grain noise reduction was that the signal energy of both the flaw and microstructure lies within the same frequency range, and hence typical filtering techniques, such as a lowpass, highpass, or a single bandpass filter, were not effective even in split-spectrum processing. The split-spectrum processing technique designed to eliminate the microstructure signal would result in the loss of the flaw signal. In addition, a signal with two distinct frequencies failed to enhance the signal-to-noise ratio in split-spectrum processing.

In the second focus of the research, noise due to material grain structure was reduced using a multi-stage adaptive filtering algorithm. A multi-stage adaptive noise cancellation scheme using a LMSE adaptive filter was developed and analyzed. The first stage adaptive filter was used as a preconditioning stage so that the signals at the output of the first stage possess the requisite correlation properties for the second stage adaptive filter to be more effective. The Multi-stage Adaptive Noise Cancellation (MANC) algorithm was demonstrated to be successful in achieving these goals as indicated in the significant jump in the de-noising performance at the second stage as shown in Table 3.4 and Table 3.5. Also, the effects of transducer distance, filter length, and leaning rate on the multi-stage adaptive noise cancellation method have been studied and selected. In addition, the optimal number of stages is selected for implementing a stopping criterion based on the SNR ratio of two successive stages. The proposed algorithm is simple and easy to implement and is seen to be effective when the filter parameters are optimal. The drawback of the proposed algorithm is the increase in implementation time complexity due to the additional adaptation stages. However, the proposed algorithm can also be implemented in real time using a TMS320C25 or TMS320C30 DSP chip for on-line inspection applications.

The third emphasis of this research is to develop a multi-dimensional signal processing and classification scheme. In this thesis, ultrasonic signal classification algorithms based on the information in a neighborhood of A-scans have been developed. Implementations of one, two, and three-dimensional signal classifications have been presented. Table 6.1 summarizes the different implementations of multi-dimensional processing.

Table 6.1 Summary of multi-dimensional processing.

Dimension	Feature	Neural Network	Classification Performance	Note
One	DWT	140-40-12-4	24/28	Time-frequency processing
Two	FFT Magnitude	4096-40-12-4	27/28	Use echo dynamics on linear scan
	FFT Phase	256-40-12-4	27/28	
	Mean [Magnitude Phase]	512-40-12-4	28/28	
	PCA	44-20-8-4	28/28	
Three	Spatial moment	64-12-2	25/28	Usage of volume data on spatial and frequency domain
	FFT moment	64-12-2	21/28	

In general, ultrasonic signal classification systems are based on processing individual A-scans. Even though these approaches show reasonable success, a single A-scan signal itself cannot represent a flaw in time, space, or transform domain. Another drawback of these approaches is that they do not incorporate the effect of beam spread. A better approach is to analyze a neighborhood of signals prior to making a classification decision. Such an approach provides a better estimate of the dynamics in the signal. Because of these reasons, the two and three-dimensional signal classification techniques were studied. In two-dimensional signal classification, the various features using magnitude, phase, and the first moment of combined magnitude and phase spectra on two-dimensional Fourier transform were investigated. In particular, the first moment of combined magnitude and phase spectra resulted in a good classification performance. In addition, a two-dimensional process using principal component analysis showed comparable results, where the variance of a group of A-scans in a neighborhood is computed. Furthermore, the initial results of moments in three-dimensional spatial and transform domain clearly demonstrate the ability of a neural network to discriminate between planar (crack and lack of fusion) and volumetric (slag and porosity) discontinuities. The results are, however, obtained only on a limited set of data and need to be validated on a larger database.

A major problem encountered in this work was the availability of reliable training data. Although a significant amount of effort was spent on "cleaning" this database, the training data was used in developing the ASC system contained conflicting information. The availability of a reliable numerical model would have solved this problem. However, to-date there are no theoretical models that can simulate the ultrasonic wave propagation in a weld region with porosity, slag or lack of fusion. Lack of reliable simulated and experimental data proved to be a serious drawback in this work.

6.2 Future Work

In the multi-stage adaptive filtering method, the capability of noise reduction has been demonstrated. However, the performance depends strongly on the filter parameters and hence automated selection of optimal filter parameters should be investigated. Alternate adaptation algorithms must also be evaluated. Future work will focus on a study using the following approaches.

- Combinations of algorithms in different stages will also be studied. In this research, the LMS adaptation algorithm has been used in adjusting filter weights. For the multi-stage adaptive filtering method, each stage adaptation algorithm can adopt different adaptation methods such as recursive least square algorithm or constant modulus algorithm.
- In signal classification, feature extraction will concentrate on classification of a larger database. For the feature extraction, the automated feature selection such as ID3 with three-dimensional Fourier transform will also be useful for identifying the features with the most amount of discriminatory information.

APPENDIX

PROPERTIES OF THREE-DIMENSIOANL FOURIER TRANSFORM

In discussing the three-dimensional discrete Fourier transform (DFT), we have not assumed that our image data contains only real sample values. Indeed, all of the results are valid whether $f(x,y,z)$ is real or complex. As with one- or two-dimensional discrete Fourier transforms, however, if $f(x,y,z)$ is known to consist of a real sequence of data, the DFT will satisfy symmetry property. We investigate some properties of three-dimensional Fourier transform.

The three-dimensional DFT pair is defined as

$$F(u,v,w)=\sum_{x=0}^{N-1}\sum_{y=0}^{N-1}\sum_{z=0}^{N-1} f(x,y,z)W_N^{ux+vy+wz} \qquad \text{for } u,v,w=0,1,2,\ldots,N-1. \qquad \text{(A.1)}$$

and

$$f(x,y,z)=\sum_{u=0}^{N-1}\sum_{v=0}^{N-1}\sum_{w=0}^{N-1} F(u,v,w)W_N^{-(ux+vy+wz)} \qquad \text{for } x,y,z=0,1,2,\ldots,N-1. \qquad \text{(A.2)}$$

where $W_N=e^{-j2\pi/N}$ and $f(x,y,z)$ represents a volumetric data that is a function of three discrete spatial variables x, y, and z. The variables u, v, and w are frequency variables.

1. Conjugate Symmetry

In symmetric property, let $f(x,y,z)$ be real. The Fourier transform exhibits conjugate symmetry, which can be written as

$$F(u,v,w) = F^*(-u,-v,-w) \tag{A.3}$$

and the magnitude of $F(u,v,w)$ is

$$|F(u,v,w)| = |F(-u,-v,-w)| \tag{A.4}$$

where $F^*(-u,-v,-w)$ is the complex conjugate of $F(u,v,w)$.

<u>Proof</u>

If $f(x,y,z)$ is real, $f(x,y,z) = f^*(x,y,z)$. First we can define the complex conjugate $F^*(-u,-v,-w)$ of $F(u,v,w)$ by the definition of three-dimensional Fourier transforms.

$$F^*(-u,-v,-w) = \sum_{x=0}^{N-1}\sum_{y=0}^{N-1}\sum_{z=0}^{N-1} f^*(x,y,z)\left(W_N^{-(ux+vy+wz)}\right)^* \tag{A.5}$$

The term of $\left(W_N^{-(ux+vy+wz)}\right)^*$ simply can be computed as follows:

$$\left(W_N^{-(ux+vy+wz)}\right)^* = \left(W_N^{ux+vy+wz}\right). \tag{A.6}$$

Second, by the definition Equation (A.1), the magnitude of $F(u,v,w)$ can be calculated as

$$\left|F(u,v,w)\right| = \left|\sum_{x=0}^{N-1}\sum_{y=0}^{N-1}\sum_{z=0}^{N-1} f(x,y,z) W_N^{ux+vy+wz}\right| \tag{A.7}$$

and

$$\left|F(-u,-v,-w)\right| = \left|\sum_{x=0}^{N-1}\sum_{y=0}^{N-1}\sum_{z=0}^{N-1} f(x,y,z)\left(W_N^{-(ux+vy+wz)}\right)\right|. \tag{A.8}$$

Since the magnitude of term $\left|W_N^{ux+vy+wz}\right| = \left|W_N^{-(ux+vy+wz)}\right|$, (A.7) and (A.8) hold validly.

2. Periodicity

The validity of periodic property can be demonstrated by direct substitution of the variables $(u+N)$, $(v+N)$ and $(w+N)$ in Equation (A.1). This property represents that only one period of the transform is necessary to specify $F(u,v,w)$ completely in the frequency domain. The periodic property with period N can be defined as

$$\begin{aligned} F(u,v,w) &= F(u+N,v+N,w) \\ &= F(u+N,v,w+N) \\ &= F(u,v+N,w+N) \\ &= F(u+N,v+N,w+N). \end{aligned} \tag{A.9}$$

Proof

Let us first compute the periodic property $F(u,v,w) = F(u+N,v+N,w)$. By definition, $F(u+N,v+N,w)$ with period N can be written as

$$F(u+N,v+N,w) = \sum_{x=0}^{N-1}\sum_{y=0}^{N-1}\sum_{z=0}^{N-1} f(x,y,z)W_N^{(u+N)x+(v+N)y+wz} \qquad \text{(A.10)}$$

where $u,v,w = 0,1,2,\ldots,N-1$. Since $\left(W_N^{Nx}\right)$ and $\left(W_N^{Ny}\right)$ in term $\left(W_N^{(u+N)x+(v+N)y+wz}\right)$ are always equal to one, $\left(W_N^{(u+N)x+(v+N)y+wz}\right)$ is equal to $\left(W_N^{ux+vy+wz}\right)$. Therefore, $F(u,v,w) = F(u+N,v+N,w)$ hold validly. A similar process can be used to prove periodicity.

BIBLIOGRAPHY

[1] Howard B. Cary. *ARC Welding Automation*. New York. NY: Marcel Dekker. Inc.. 1995.

[2] *Standard Welding Terms and Definitions*. AWS 3.0-89. The American Welding Society. Miami. FL.

[3] *Symbols of Welding and Non-destructive Testing, AWS 2.4*. The American Welding Society. Miami. FL.

[4] *Standard Reference Radiographs for Examination of Aluminum Fusion Welds*. The American Society for Testing and Materials. West Conshohocken. PA.

[5] Robert C. McMaster. *Nondestructive Testing Handbook*. Vol. 1 and 2. New York. NY: The Ronald Press. 1963.

[6] *ASM Handbook: Nondestructive Evaluation and Quality Control*. ASM vol. 17. Materials Park. OH. 1992.

[7] *ASNT Handbook: Nondestructive Testing Handbook*, 2nd ed.. ASNT. Vol. 3. Columbus. OH. 1985.

[8] J. Seydel and R. S. Sharpe. "Ultrasonic Synthetic Aperture Focusing Techniques in NDT." *Research Techniques in Nondestructive Testing*, Vol. 6, pp. 1-47. New York: Academic Press. 1982.

[9] Juha Ylitalo. "A Fast Ultrasonic Synthetic Aperture Imaging Method: Application to NDT." *Ultrasonics*. Vol. 34, pp. 331-333, 1996.

[10] J. G. Costa, R. E. Gonzalez, R. E. Guyotte, D. P. Salvano, T. Swift, and R. J. Koenig, "Titanium rotating components review team report," *Federal Aviation Administration*, December. 1990.

[11] R. L. Scheaffer, J. T. McClave, *Probability and Statistics for Engineers*. 2nd Edition. Boston: Duxbury Press. 1986.

[12] Chien-Ping Chiou, R. Bruce Thompson, and Lester W. Schmerr, "Ultrasonic Signal-to-Noise Ratio Enhancement Using Adaptive Filtering Technique," *Review of Progress in Quantitative Nondestructive Evaluation of Materials*, Vol. 14, pp. 727-732, 1995.

[13] R. Murthy, N. M. Bilgutay, and J. Saniie, "Application of Bandpass Filtering in Ultrasonic Nondestructive Testing," *Review of Progress in Quantitative Nondestructive Evaluation of Materials*, Vol. 8, pp. 759-767, 1989.

[14] V. L. Newhouse, N. M. Bilgutay, J. Saniie, and E. S. Furgason, "Flaw-to-grain Echo Enhancement by Split-spectrum Processing," *Ultrasonics*, Vol. 20, pp. 59-68, 1982.

[15] Y. Zhu and J. P. Weight, "Ultrasonic Nondestructive Evaluation of Highly Scattering Materials Using Adaptive Filtering and Detection," *IEEE Transactions on Ultrasonics, Ferroelectrics, and Frequency Control*, Vol. 41, No.1, pp. 26-33, 1994.

[16] S. Bae, J. Kim, L. Udpa, and S. S. Udpa, "A New Adaptive Grain Noise Cancellation Filtering Technique," *Review of Progress in Quantitative Nondestructive Evaluation of Materials*, Vol. 17, pp. 759-766, 1997.

[17] L. Udpa, and S. S. Udpa, "Application of Signal Processing and Pattern Recognition Techniques to Inverse Problems in NDE," *International Journal of Applied Electromagnetics and Mechanics*, No. 8, pp. 99-117, 1997.

[18] R. Polikar, L. Udpa, S. S. Udpa, and T. Taylor, "Frequency Invariant Classification of Ultrasonic Weld Inspection Signals," *IEEE Trans. Ultrasonics, Ferroelectrics and Frequency Control*, Vol. 45, No. 3, pp. 614-625, May 1998.

[19] P. Ramuhalli, L. Udpa, and S. S. Udpa, "An Automatic Signal Classification System for Ultrasonic Weld Inspection Signals," *Materials Evaluation*, Vol. 58, No. 1, pp. 85-89, January 2000.

[20] Gordon S. Kino, *Acoustic Waves: Devices, Imaging and Analog Signal Processing*, Englewood Cliffs, NJ: Prentice Hall, 1987.

[21] David A. Hutchins, H. D. Mair, P. A. Puhach, and A. J. Osei, "Continuous-wave Pressure Fields of Ultrasonic Transducers," *J. Acoust. Soc. Am.*, Vol. 80, No. 1, pp. 1–12, July 1986.

[22] N. K. Batra, K. E. Simmonds, H. H.Chaskelis, and R. B. Mignogna , "Mapping of Three Dimensional Radiation Field of Ultrasonic Transducers," in *Review of Progress in Quantitative Nondestructive Evaluation*, edited by D.O. Thompson and D.E. Chimenti (Plenum Press, New York 1995), Vol. 14A, pp. 1029-1036.

[23] R. N. Thurston and Allen D. Pierce, *Ultrasonic Measurement Methods* (Physical Acoustics Vol. 19), Academic Press, 1990.

[24] J. H. Krautkramer, *Ultrasonic Testing of Materials*, 3rd English edition, Springer-Verlag, 1983.

[25] K. G. Hall, *Observing Ultrasonic Wave Propagation by Stroboscopic Visualization Methods*, Ultrasonics, Butterworth Press, July 1982.

[26] *Neural Networks and Semi-Automatic Scanners for NDE Applications*, EPRI TR-107119, EPRI Final Report, December 1996.

[27] S. P. Neal, P. L. Speckman, and M. A. Enright, "Flaw Signature Estimation in Ultrasonic Nondestructive Evaluation Using the Wiener filter with Limited Prior Information," *IEEE Trans. Ultrasonics, Ferroelectrics and Frequency Control*, Vol. 40, No. 4, pp. 347-353, 1993.

[28] X. Li and N. M. Bilgutay, "Wiener Filter Realization for Target Detection Using Group Delay Statistics," *IEEE Trans. Signal Processing*, Vol. 41, No. 6, pp. 2067-2074, June 1993.

[29] K. D. Donohue, "Maximum Likelihood Estimation of A-scan Amplitudes for Coherent Targets in Media of Unresolvable Scatters," *IEEE Trans. Ultrasonics, Ferroelectrics and Frequency Control*, Vol. 39, No. 3, pp. 422-431, May 1992.

[30] P. Karpur, P. M. Shankar, T. L. Rose, and V. L. Newhouse, "Split Spectrum Processing: Determination of the Available Bandwidth for Spectral Splitting," *Ultrasonics*, Vol. 26, No. 4, pp. 204-209, 1988.

[31] P. M. Shankar, P. Karpur, V. L. Newhouse, and T. L. Rose, "Split Spectrum Processing: Analysis of Polarity Thresholding Algorithm for Improvement of Signal-to-noise Ratio and Detectability in Ultrasonic Signals," *IEEE Trans. Ultrasonics, Ferroelectrics and Frequency Control*, Vol. 36, No. 1, pp. 101-108, 1989.

[32] J. D. Aussel, "Split Spectrum Processing with Finite Impulse Response Filters of Constant Frequency-to-bandwidth Ratio," *Ultrasonics*, Vol. 28, No. 4, pp. 229, 1990.

[33] X. Li, N. M. Bilgutay, and R. Murthy, "Spectral Histogram Using the Minimization Algorithm – Theory and Applications to Flaw Detection," *IEEE Trans. Ultrasonics, Ferroelectrics and Frequency Control*, Vol. 39, No. 2, pp. 279-284, Mar. 1992.

[34] J. Xin, K.D. Donohue, N. M. Bilgutay, and X. Li, "Frequency-diverse Geometric- and Arithmetic-mean Filtering for Ultrasonic Flaw Detection," *Material Evaluation*, Vol. 8, pp. 987-992, 1991.

[35] M. G. Gustafsson, and T. Stepinski, "Split Spectrum Algorithms Rely on Instantaneous Phase Information," *IEEE Trans. Ultrasonics, Ferroelectrics and Frequency Control*, Vol. 40, No. 6, pp. 659-665, Nov. 1993.

[36] B. Widrow and S. D. Stearns, *Adaptive Signal Processing*, Englewood Cliffs, NJ: Prentice Hall, 1985.

[37] B. Widrow et al., "Adaptive Noise Cancelling: Principles and Applications," *Proc. IEEE*, Vol. 63, pp. 1692-1716, December 1975.

[38] B. Widrow et al., "Adaptive Antenna Systems," *Proc. IEEE*, Vol. 55, pp. 2143-2159, December 1967.

[39] J. S. Lim and A. V. Oppenheim, *Advanced Topics in Signal Processing*, Prentice Hall, Elglewood Cliffs, NJ, 1988.

[40] W. K. Jenkins, A. W. Hull, J. C. Strait, B. A. Schnaufer, and X. Li, *Advanced Concepts in Adaptive Signal Processing*, Kluwer Academic Publishers, Norwell, MA, 1996.

[41] Odile Macchi, *Adaptive Processing: The Least Mean Squares Approach with Applications in Transmission*, John Wiley & Sons Ltd, West Sussex, England, 1995.

[42] D. L. Donoho, "Nonlinear Wavelet Methods for Recovery of Signals, Densities, and Spectra from Indirect and Noisy Data," in *Proceedings of Symposia in Applied Mathematics*, Vol. 47, pp. 173-205, 1993.

[43] H. L. Resniloff and R. O. Wells Jr., *Wavelet Analysis: The Scalable Structure of Information*. Springer-Verlag, New York, 1998.

[44] Charles K. Chui (ed.), *Wavelets: A Tutorial in Theory and Applications, Wavelet Analysis and Its Application*. Vol. 2, Academic Press, Boston, 1992.

[45] D. L. Donoho, "De-noising by Soft-Thresholding," *IEEE Trans. Inform. Theory*. Vol. 41, pp. 613-627, May 1995.

[46] D. L. Donoho and I. M. Johnstone, "Adapting to Unknown Smoothness Via Wavelet Shrinkage," *J. Amer. Stat. Assoc.*, Vol. 90, pp. 1200-1224, 1995.

[47] D. L. Donoho and I. M. Johnstone, *Ideal special adaptation by wavelet shrinkage*. Technical Report, Department of Statistics, Stanford University, 1992.

[48] R. T. Ogden, *Essential Wavelets for Statistical Applications and Data Analysis*. Birkhauser Boston, 1997.

[49] B. Vidakovic, *Statistical Modeling by Wavelets*. Wiley Series in Probability and Statistics, 1999.

[50] D. L. Donoho and I. M. Johnstone, "Ideal Spatial Adaptation Via Wavelet Shrinkage," *Biometrika*, Vol. 81, pp. 425-455, 1994.

[51] A. Bruce and H. Y. Gao, "Understanding WaveShrink: Variance and Bias Estimation," Tech. Rep. 36, StatSci Division of MathSoft, Inc., 1995.

[52] I. Daubechies, *Ten Lectures on Wavelets*. Philadelphia, PA: SIAM, 1992.

[53] J. L. Rose and G. P. Singh, "A Pattern Recognition Reflector Classification Study in the Ultrasonic Inspection of Stainless Steel Pipe Welds," *British Journal of Nondestructive Testing* Vol. 21, No. 6, pp.308-311, Nov. 1979.

[54] J. L. Rose, M. J. Avioli, and M. E. Lapides, "A Physically Modeled Feature Based Ultrasonic System for IGSCC Classification," *Material Evaluation*, Vol. 40. No. 13, pp. 1367-1383. December 1982.

[55] S. F. Burch, "A Physical Approach to the Automated Ultrasonic Characterization of Buried Weld Defects in Ferritic Steel, " *NDT International*. Vol. 19, No. 3, pp. 145-153. June 1986.

[56] Michael R. Portnoff, "Time-Frequency Representation of Digital Signals and Systems Based on Short-Time Fourier Analysis," *IEEE Trans. Acoustics, Speech and Signal Processing*, Vol. 28. No. 1, pp. 55-69, 1980.

[57] M. Louys. J. L. Starck, S. Mei, F. Bonnarel, and F. Murtagh, "Astronomical Image Compression," *Astronomy and Astrophysics Supplement Series*, Vol. 136. pp. 579-590, May 1999.

[58] M. Vetterli and J. Kovacevic, *Wavelets and Subband Coding*, Englewood Cliffs, NJ: Prentice Hall, 1995.

[59] M. B. Ruskai, et al., *Wavelets and Their Applications*. Boston, MA: Jones and Bartlett, 1992.

[60] O. V. Vasilyev. D. A. Yuen and S. Paolucci, "The Solution of PDEs Using Wavelet." *Computers in Phys.*. Vol. 11. No. 5, pp. 429-435, 1997.

[61] S. Mallat, "A Theory for Multiresolution Signal Decomposition: The Wavelet Representation." *IEEE Pattern Anal. and Machine Intell.*, Vol. 11, No. 7. pp. 674-693, 1989.

[62] M. J. Shensa, "The Discrete Wavelet Transform: Wedding the A Trous and Mallat Algorithms," *IEEE Trans. on Signal Processing*, Vol. 40, No. 10, pp 2464-2482, 1992.

[63] G. Strang, T. Nguyen, *Wavelets and Filter Banks*, Wellesley-Cambridge Press, 1996.

[64] J. R. Quilan, "Introduction of Decision Tree," *Machine Learning*, Vol. 1, pp. 81-106, 1986.

[65] Shannon Claude, *A Mathematical Theory of Communication*, Bell System Technical Journal, 1984.

[66] Morton Nadler and Eric P. Smith, *Pattern Recognition Engineering*, New York, NY: John Wiley & Sons, Inc., 1992.

[67] J. T. Tou and R. C. Gonzalez, *Pattern Recognition Principles*, Reading, MA: Addison-Wesley Publishing, 1974.

[68] S. Haykin, *Neural Networks: A Comprehensive Foundation*, Englewood Cliffs, NJ: Prentice-Hall, 1994.

[69] R. P. Lippmann, "An Introduction to Computing with Neural Nets," *IEEE Trans. Acoustics, Speech and Signal Processing Magazine*, Vol. 4, No. 2, pp. 4-22, 1987.

[70] Don R. Hush and Bill G. Horne, "Progress in Supervised Neural Networks: What's New Since Lippmann?" *IEEE Signal Processing Magazine*, pp. 8-36, January 1993.

[71] D. Dudgeon and R. Mersereau, *Multidimensional Digital Signal Processing*, Englewood Cliffs, Prentice-Hall, 1984.

[72] Rafael C. Gonzalez and Richard E. Woods, *Digital Image Processing*, Reading, MA: Addison-Wesley Publishing, 1992.

[74] K. Pearson, "On Lines and Planes of Closest Fit to Systems of Points in Space," *Philosophical Magazine*, Vol. 2, pp.559-572, 1901.

[75] H. Hotelling, "Analysis of A Complex of Statistical Variables into Principal Components," *Journal of Educational Psychology*, Vol. 24, pp. 417-441, pp. 498-520, 1933.

[76] K. Karhunen, "Uber lineare methoden in der Wahrsccheilichkeitsrechnung," *Annales Academiae Scientiarum Fennicae, Seried A1: Mathematica-Physica*, Vol. 37, pp. 3-79, 1947.

[77] M. Loéve, *Probability Theory*, Van Nostrand, New York, 1963.

[78] Erkki Oja, *Subspace Methods of Pattern Recognition, Pattern Recognition and Image Processing Series*, Vol. 6, John Wiley & Sons, 1983.

[79] Erkki Oja, "Neural Networks, Principal Components, and Subspaces," *International Journal of Neural Systems*, Vol. 1, No. 1, pp. 61-68, 1989.

ACKNOWLEDGMENTS

I would like to express my deep gratitude to my advisor, Dr. Lalita Udpa, for her invaluable guidance, support, and encouragement throughout the graduate program. She has earned my highest respect for generously sharing her wisdom and knowledge with me during my stay at Iowa State University.

I would like to extend my thanks to Dr. Satish Udpa and Dr. William Lord for sharing their rich knowledge and helpful discussions.

I would also like to appreciate Dr. Julie Dickerson and Dr. William Meeker for willingly taking the time to serve on my graduate committee.

My special thanks go to Debbie Hunter and Brad Trump for their corrections on this dissertation. I also wish to acknowledge the members of the Material Assessment Research Group at Iowa State University, especially Pradeep Ramuhalli and Robi Polikar for sharing their personal time and knowledge.

I would particularly like to express my thanks to my lovely wife, Kyeonghee Bae, my talented son, Jinho, and my parents for their endless encouragement and support.